INVESTIGATING THE *in vitro* CORROSION BEHAVIOUR OF FOUR AS-CAST MAGNESIUM-ZINC ALLOYS FOR ORTHOPAEDIC APPLICATIONS IN SIMULATED BODY FLUID

by

Nivedita Mahesh

B.E., College of Engineering, Guindy, Anna University, 2013

A THESIS SUBMITTED IN PARTIAL FULFILLMENT OF
THE REQUIREMENTS FOR THE DEGREE OF

MASTER OF APPLIED SCIENCE

in

THE COLLEGE OF GRADUATE STUDIES

(Mechanical Engineering)

THE UNIVERSITY OF BRITISH COLUMBIA
(Okanagan)

August 2015

Abstract

The use of metallic biomaterials, such as titanium alloys, stainless steels and cobalt-chromium alloys in bone implant devices is indispensable to support the bone during the healing period. However, prolonged use of implantation devices made of these inert biomaterials may lead to stress shielding due to their high elastic moduli resulting in the loss of bone density during the remodeling process. Therefore, magnesium is being investigated as a possible biomaterial for temporary fixation devices as it has low elastic modulus close to that of the human cortical bone in addition to being biocompatible and biodegradable in the aqueous chloride environment of the human body. However, the high corrosion rates of magnesium due to its low standard electrode potential compromise the mechanical integrity of the implant during the bone healing process. This thesis involved the fabrication of four magnesium-zinc alloys with 1, 1.5, 2 and 5 weight percent Zn in Mg in an attempt to tailor the corrosion rate of the alloy. The hardness and densities of the alloys were determined. The microstructure of the alloys was characterized by chemical analysis both before and after corrosion experiments. Both gravimetric and electrochemical studies were used to understand the *in vitro* corrosion behaviour of the alloys in static Simulated Body Fluid (SBF). The weight loss measurements after immersion tests indicated that the as-cast Mg-2.0Zn alloy had the lowest corrosion rate owing to network-like second phase precipitations. The potentiodynamic polarization experiments yielded extremely low corrosion rates for all the alloys, and were correlated to the microstructures of the corroded surfaces. Electrochemical Impedance Spectroscopy (EIS) was conducted to study and model the interface between the sample and the SBF. The electrochemical test results indicated that the Mg-1.0Zn exhibited the highest polarization resistance leading to the decreased corrosion rate of the alloy. The corrosion products consisted of magnesium carbonates, magnesium hydroxides and calcium phosphates as indicated by Fourier Transform Infrared Spectroscopy (FTIR), X-Ray Diffraction (XRD) and X-ray Energy Dispersive Spectroscopy (X-EDS). Results were suggestive that, Mg-Zn alloys with ≤2 wt. % Zn were promising as a suitable metallic biomaterial for orthopaedic applications and should be considered for further *in vitro* and *in vivo* studies.

Preface

Part of the research involved in this thesis was conducted in the Non-Equilibrium Processing and Corrosion Laboratory, Department of Material Science and Engineering, Indian Institute of Technology (IIT), Kanpur, India with financial support from the Mitacs Globalink Research Award Program. The research experiments in IIT Kanpur were carried out by the author of this thesis under the guidance of Dr. Kallol Mondal and the supervision of Dr. Abhijeet Moon. The FTIR and XRD experiments, detailed in Chapter 3 were conducted by experienced personnel at IIT Kanpur and the raw data was analyzed by the author.

Table of Contents

Abstract ii

Preface iii

Table of Contents iv

List of Tables vii

List of Figures viii

List of Abbreviations xi

List of Elements xii

Acknowledgements xiii

Dedication xv

Chapter 1 : INTRODUCTION 1

Chapter 2 : LITERATURE REVIEW 4

2.1. Biomaterials 4

2.1.1. Tissue-material Interaction 5

2.1.2. Orthopaedic Implant Materials 6

2.1.2.1. Metallic Alloys 6

2.1.2.2. Polymers 9

2.1.2.3. Ceramics 10

2.2. Magnesium-based Biodegradable Materials 11

2.2.1. History 11

2.2.2. Properties 12

2.2.3. Corrosion Behaviour 12

2.3. Magnesium Alloys 14

2.3.1. Mg-Zn Phase Diagram 15

2.3.2. Effect of Zn on the Mechanical and Corrosion Properties of Mg Alloy 18

2.4. Corrosion Testing 19

2.4.1. *In vitro* Tests 20

2.4.2. *In vivo* Tests 21

2.5. Chapter Summary 21

Chapter 3 : EXPERIMENTAL PROCEDURE 22

3.1. Materials and Casting 22

3.2. Material Hardness 24

3.3. Characterization Techniques 24

3.3.1. Light Optical Microscopy 24

3.3.2. Scanning Electron Microscopy and X-Ray Energy Dispersive Spectroscopy 24

3.3.3. X-Ray Diffraction 25

3.4. Corrosion Testing 25

3.4.1. Solution Preparation 26

3.4.2. Immersion Tests 26

3.4.3. Post-corrosion Characterization 28

3.4.3.1. X-Ray Diffraction and SEM – X-EDS 28

3.4.3.2. Fourier Transform Infrared Spectroscopy 28

3.4.4. Electrochemical Studies 28

3.4.4.1. Tafel Polarization 30

3.4.4.2. Electrochemical Impedance Spectroscopy Tests 30

3.5. Chapter Summary 31

Chapter 4 : RESULTS AND DISCUSSIONS 32

4.1. Casting of Alloys 32

4.2. Effect of Zn on the Grain Size and Hardness of As-cast Alloys 35

4.3. Microstructural Characterization and Chemical Analysis 36

4.3.1. As-cast Microstructure 36

4.3.2. X-Ray Diffraction Studies 42

4.4. Immersion Corrosion Tests 43

4.4.1. Corrosion Surface Morphology 43

4.4.2. Effect of Increasing Zinc Content on the Corrosion Rate 47

4.4.3. Corrosion Product Characterization 48

4.4.3.1. SEM and X-EDS 48
4.4.3.2. Fourier Transform Infrared Spectroscopy 50
4.4.3.3. XRD Results 51
4.5. Electrochemical Behaviour 52
4.5.1. Tafel Polarization 54
4.5.2. Electrochemical Impedance Spectroscopy Tests 58
4.5.4. Post-polarization Microstructure 63
4.6. Variation Among the *in vitro* Techniques 66
Chapter 5 : CONCLUSIONS AND FUTURE WORK 67
5.1. Conclusions 67
5.2. Limitations of Work 69
5.3. Scope for Future Work 69
Bibliography 70
Appendix A: Corrosion Measurement Data for the Repeats of Polarization Test 78
A1: 2nd Repeat of the Electrochemical Test 78
A2: 3rd Repeat of the Electrochemical Test 82

List of Tables

Table 2.1: Application of biomaterials in various branches of medicine [2]..... 4
Table 2.2: Mechanical property comparison of various implant materials [12, 10]..... 9
Table 2.3: Phases present in the Mg-Zn binary phase diagram [40] 17
Table 3.1: Designation of samples..... 22
Table 3.2: Chemical quantities for preparation of 1L of SBF [33]..... 26
Table 4.1: Grain size values and hardness measurements of all samples..... 35
Table 4.2: Functional groups corresponding to FTIR Spectroscopy peaks..... 51
Table 4.3: Corrosion parameters for all samples derived from OCP and Tafel plots..... 54
Table 4.4: Passivation parameters for Z5 alloy 57
Table 4.5: Values of the electrical parameters of the curve fitted EIS data..... 62
Table A1.1: Values of the electrical parameters of the curve-fitted EIS data (Repeat 2).....82
Table A2.1: Values of the electrical parameters of the curve-fitted EIS data (Repeat 3).....86

List of Figures

Figure 1.1: Objectives of research 3
Figure 2.1: Magnesium-Zinc phase diagram [42]..... 16
Figure 2.2: Optical Micrograph of Mg-9Zn (hypoeutectic) alloy with $Mg_{51}Zn_{20}$ particles in α(Mg) matrix [43] 17
Figure 2.3: (a) The dark regions are the interdendritic phase in as-cast Mg-6Zn; (b) After heat treatment uniform microstructure is observed with complete disappearance of interdendritic phase [33]..... 18
Figure 3.1: Photographs of (a) graphite die used for casting; (b) as-cast sectioned specimen of Z2 alloy..... 23
Figure 3.2: Schematic of cut samples used for further study..... 23
Figure 3.3: Schematic of sample cross-section showing the Vickers hardness indentations along the diameter 24
Figure 3.4: Bruker D8 X-Ray Diffractometer..... 25
Figure 3.5: Photographs of (a) specimen of disc sectioned from as-cast ingots and Ex Mg-CP; (b) specimen of cut sample used for immersion tests with Teflon tape covering the sides; (c) temperature controlled water bath..... 27
Figure 3.6: Schematic of Electrochemical cell and Potentiostat [58]..... 29
Figure 3.7: Photographs of the electrochemical cell setup 29
Figure 3.8: Flowchart summarizing the experiments conducted in this thesis..... 31
Figure 4.1: Photograph of as-cast specimens of (a) Mg-CP; (b) sectioned specimen of Z2 with a macro-pore 33
Figure 4.2: X-EDS quantification of elements present in as-cast (a) Z1; (b) Z1.5; (c) Z2; (d) Z5 34
Figure 4.3: Hardness and grain size of all samples..... 35
Figure 4.4: Optical micrographs of the (a) Ex Mg-CP; (b) AC Mg-CP; and as-cast (c) Z1; (d) Z1.5; (e) Z2; (f) Z5 alloys..... 37
Figure 4.5: SEM images of the (a) Ex Mg-CP and as-cast (b) Z1; (c) Z1.5; (d) Z2; (e) Z5 alloys..... 39

Figure 4.6: SEM images of the as-cast (a) Z1; (b) Z1.5; (c) Z2; (d) Z5 alloys showing the spectra chosen for X-EDS analysis (indicated by arrows).. 41
Figure 4.7: XRD patterns of alloys before corrosion..... 42
Figure 4.8: Corroded surfaces of (a) Ex Mg-CP; (b) Z1; (c) Z1.5; (d) Z2; (e) Z5 samples after immersion for 10 days in SBF 44
Figure 4.9: SEM images of corroded surfaces of (a) Ex Mg-CP and as-cast (b) Z1; (c) Z1.5; (d) Z2; (e) Z5 alloys after immersion for 10 days in SBF 46
Figure 4.10: Corrosion rates of the samples after immersion for 10 days in SBF..... 47
Figure 4.11: SEM images of corroded (a) Ex Mg-CP; (b) Z1; (c) Z1.5; (d) Z2; (e) Z5 samples after immersion for 10 days in SBF after immersion for 10 days in SBF showing the area mapped X-EDS spectra 49
Figure 4.12: FTIR spectrum of the filtrate obtained after immersion tests for all as-cast alloys 50
Figure 4.13: XRD patterns of alloys after corrosion..... 52
Figure 4.14: OCP vs. time plots for all samples 54
Figure 4.15: Tafel plots for (a) Ex Mg-CP and as-cast alloys; (b) AC Mg-CP 55
Figure 4.16: Corrosion rates of the samples from Tafel polarization. 56
Figure 4.17: Nyquist plots for (a) Z1 and Z5; (b) AC Mg-CP; (c) Z2 and Ex Mg-CP; (d) Z1.5 samples..... 59
Figure 4.18: Bode (a) magnitude and; (b) phase plots for all samples 60
Figure 4.19: (a) Equivalent electrochemical circuit for the corrosion model; (b) physical model of the electrode/electrolyte interface..... 62
Figure 4.20: SEM images of corroded surfaces of (a) Ex Mg-CP; (b) Z1; (c) Z1.5; (d) Z2; (e) Z5 samples after dynamic polarization tests. 64
Figure 4.21: SEM images of corroded (a) Ex Mg-CP; (b) Z1; (c) Z1.5; (d) Z2; (e) Z5 alloys after dynamic polarization tests showing the area mapped X-EDS spectra 65
Figure A1.1: OCP vs. time plots for all samples (Repeat 2)……78
Figure A1.2: Tafel plots for (a) Ex Mg-CP and as-cast alloys; (b) AC Mg-CP (Repeat 2)....79
Figure A1.3: Nyquist plots for (a) Z1, Z2 and Ex Mg-CP; (b) AC Mg-CP; (c) Z5 and; (d) Z1.5 samples (Repeat 2)…….80

Figure A1.4: Bode (a) magnitude and; (b) phase plots for all samples (Repeat 2)……. 81
Figure A2.1: OCP vs. time plots for all samples (Repeat 3)……82
Figure A2.2: Tafel plots for (a) Ex Mg-CP, Z1, Z1.5 and Z2; (b) Z5 and
AC Mg-CP (Repeat 3)……... 83
Figure A2.3: Nyquist plots for (a) Z1; (b) Z2; (c) AC Mg-CP and Z5;
(d) Ex Mg-CP and Z1.5 samples (Repeat 3)…….. 84
Figure A2.4: Bode (a) magnitude and; (b) phase plots for all samples (Repeat 3)……..85

List of Abbreviations

ACAP	Amorphous Calcium Apatite Precursor
BMG	Bulk Metallic Glass
BSE	Back Scattered Electron
DNA	Deoxyribonucleic Acid
ECAP	Equal Channel Angular Pressing
EIS	Electrochemical Impedance Spectroscopy
FTIR	Fourier Transform Infrared Spectroscopy
GRF	Growth Restriction Factor
HAP	Hydroxyapatite
ICSD	Inorganic Crystal Structure Database
JCPDS	Joint Committee on Powder Diffraction Standards
NDE	Negative Difference Effect
OCP	Open Circuit Potential
PGA	Poly (glycolic acid)
PLA	Poly (lactic acid)
PMMA	Poly(methylmethacrylate)
RNA	Ribonucleic Acid
SBF	Simulated Body Fluid
SCC	Stress Corrosion Cracking
SCE	Standard Calomel Electrode
SE	Secondary Electron
SEM	Scanning Electron Microscope
SHE	Standard Hydrogen Electrode
TCP	β-Tricalcium Phosphate
UHMWPE	Ultra-high Molecular Weight Poly(ethylene)
X-EDS	X-Ray Electron Dispersive Spectroscopy
XRD	X-Ray Diffraction

List of Elements

Al	Aluminum
C	Carbon
Ca	Calcium
Co	Cobalt
Cr	Chromium
Fe	Iron
Li	Lithium
Mg	Magnesium
Mn	Manganese
Mo	Molybdenum
REE	Rare Earth Element
Si	Silicon
Ti	Titanium
V	Vanadium
Y	Yttrium
Zn	Zinc
Zr	Zirconium

Acknowledgements

I am extremely grateful to have had Dr. Lukas Bichler and Dr. Hadi Mohammadi as my supervisors. Dr. Bichler's guidance, teaching and patience helped me grow both as a researcher and a better person. His constant words of encouragement and support kept me going and striving to do better.

Dr. Mohammadi's fruitful insights helped me bridge the gap between medicine and engineering, making my research much more enjoyable. I am grateful for his professional and personal advice and for all the support he has extended towards me.

I would like to sincerely thank Dr. Kallol Mondal for giving me an opportunity to work with him by accommodating me in his lab at IIT Kanpur and introducing me to the wonderful world of corrosion science.

I wish to thank Dr. Andre Phillion for having taught me the various concepts of material science through his challenging courses which helped me immensely during the course of my research and the writing of my thesis.

I am very grateful to Dr. Abhijeet Moon for his support, guidance, advice and for answering all my queries with the utmost patience.

I would like to extend special thanks to Mukund Manish, Manish Jain, Abhinav Varshney, Soumendu Monia, Avijit Mukherjee and Harish Verma for their support and for making my stay in IIT Kanpur a memorable one. I am thankful for the financial support provided by Mitacs, which made my stay possible in the first place.

I wish to thank David Arkinstall for his wonderful insights during the endless SEM hours and my colleague, Mathew Smith for teaching me a few tricks of the trade about metals.

My list would not be complete without appreciating the support from my friends - Pankaj Bokdia and Ashritha Mohan for the beautiful undergraduate years and their constant phone calls to Canada which kept me sane, Tausif Ejaz Khan, who always managed to make me smile and lastly, Abhinav Karanam, who was with me through the ups and downs of graduate life and for making my stay in Canada a wonderful experience.

Finally, I am extremely grateful to my parents for their unconditional love and emotional support in all stages of life and to my sister, who made me laugh at the toughest of times.

To my parents, Nalini and V.S. Mahesh and my baby sister, Namrata.

Chapter 1 : INTRODUCTION

For more than a century, metallic biomaterials have been used as implantation and fixation devices to replace broken bones and to support their healing [1]. The use of metals in orthopaedic applications can be attributed to their high strength and good ductility, which make them suitable for use in load bearing areas of the human skeleton [2]. The need and importance of orthopaedic implants and fixation devices was highlighted in 2011 by Statistics Canada [3]. In 2009 and 2010, broken bones and fractures were found to be a major health risk faced by ~17% of Canadians older than 12 years of age, and were seen limiting at least one everyday activity of the affected individual [3]. Knee and lower leg are one of the most affected body parts among the ~17% of affected individuals [3]. Depending on the severity of the injury, lower leg injuries may have to be either treated with bone replacement implants in extreme scenarios or with temporary fixation devices (e.g. bone plates, screws, rods or intramedullary nails), which internally support the bone during the healing period [2].

Since lower leg bones, like tibia and femur, support the weight of the human body and experience cyclic loading, fixation devices need to have sufficient mechanical properties. Stainless steel, cobalt-chromium based alloys, titanium and titanium based alloys are widely used for such orthopaedic applications, owing to their chemical inertness in the human body [4], and high impact strength and wear resistance [2]. However, their high elastic moduli may lead to problems of stress shielding, causing the regenerated bone at the implant site to grow with a lower density as the applied force transmits through the implant instead of the newly formed bone [5]. This may cause loosening of the implant and lead to secondary fracture as a result of the loss of bone density at the implant site [6]. Also the fracture fixation needs to be removed surgically once the new tissue is regenerated, thus increasing health care costs and possibility of infections [2]. To circumvent these issues, polymers and ceramics are being investigated extensively due to their biodegradable ability [7, 8]. However, their use as materials for temporary fixation devices in load bearing sites is limited by the low stiffness and brittleness of most polymers and ceramics, respectively [2, 9]. It has been suggested that magnesium-based alloys might be a suitable biomaterial for orthopaedic applications, as their controlled corrosion and dissolution in the physiological environment of the human body may avoid the need for a second surgery [10].

The use of magnesium (Mg) as a biomaterial first began in the form of Mg wire ligatures for bleeding vessels in 1878, nearly 120 years after its discovery [1]. Many human and animal experiments were conducted using magnesium wires, tubes, rods, vessels, plates, etc. in the first half of the 20^{th} century [1, 10]. However, the use of magnesium as a biomaterial was overlooked in the mid 1900's owing to its corrosive nature accompanied by hydrogen gas evolution and emergence of more inert and stronger stainless steel and titanium alloys, as surgical implant materials [11]. In recent years, the corroding ability of magnesium combined with its high specific strength has raised interest in magnesium-based biomaterials as plausible resorbable temporary fixation devices [12]. Also, as magnesium is present in ionic form in the human body to aid cellular functions (eg. DNA and RNA stabilization) and acts as an enzymatic cofactor [13], the release of Mg^{2+} ions during *in vivo* corrosion would not only be harmless to the patient, but may further assist in new bone formation and strengthen bone-implant interface [14, 15]. Thus, magnesium is thought to have the potential to be biocompatible with the human body without eliciting any harmful physiological reactions.

Despite the advantages of using magnesium as an orthopaedic biomaterial, its use is limited by two primary reasons: Firstly, the high reactivity of magnesium *in vivo* may cause the implant to lose its mechanical integrity and result in implant failure before the bone reformation process is complete [12]. Secondly, the common alloying elements like aluminum (Al) and rare-earth elements (REEs) improve the corrosion resistance and strength of magnesium alloys, but they are not suitable for use in the human body, since Al is known to be neurotoxic and some REEs accumulate in the liver and bone causing toxic reactions in the body [9, 16]. The corrosion resistance and mechanical properties of magnesium can be considerably improved by precipitation hardening, solid solution strengthening, alloying, and surface modifications [17-19]. The alloying elements have to be chosen such that they are non-toxic and improve the overall mechanical and corrosion properties of the implant. Zinc (Zn), manganese (Mn), and calcium (Ca) are the first preference as alloying elements as they are biocompatible and are already present in the body [9]. However, concentrations of manganese above 0.8 μg/L in the blood serum is known to be neurotoxic and therefore, Mn addition is limited to within 0.5-1.5 weight percent (wt. %) [9, 12]. Increasing additions of calcium results in lower corrosion resistance due to formation of Mg_2Ca phase [6]. Thus, in

this research zinc was chosen as the alloying element. In the future, the Mg-Zn alloys could be tested *in vitro* in a dynamic fluid environment, and *in vivo* in animal models.

The aim of the present study was to investigate the effect of varying Zn concentration in Mg-Zn binary alloy system and study their corrosion characteristics. A few different Mg-Zn alloys were cast and characterized in order to study the corrosion behaviour and identify the corrosion products of the Mg-Zn alloys and commercial purity magnesium. The short and long-term objectives of this research are presented in the form of a flow chart in Figure 1.1.

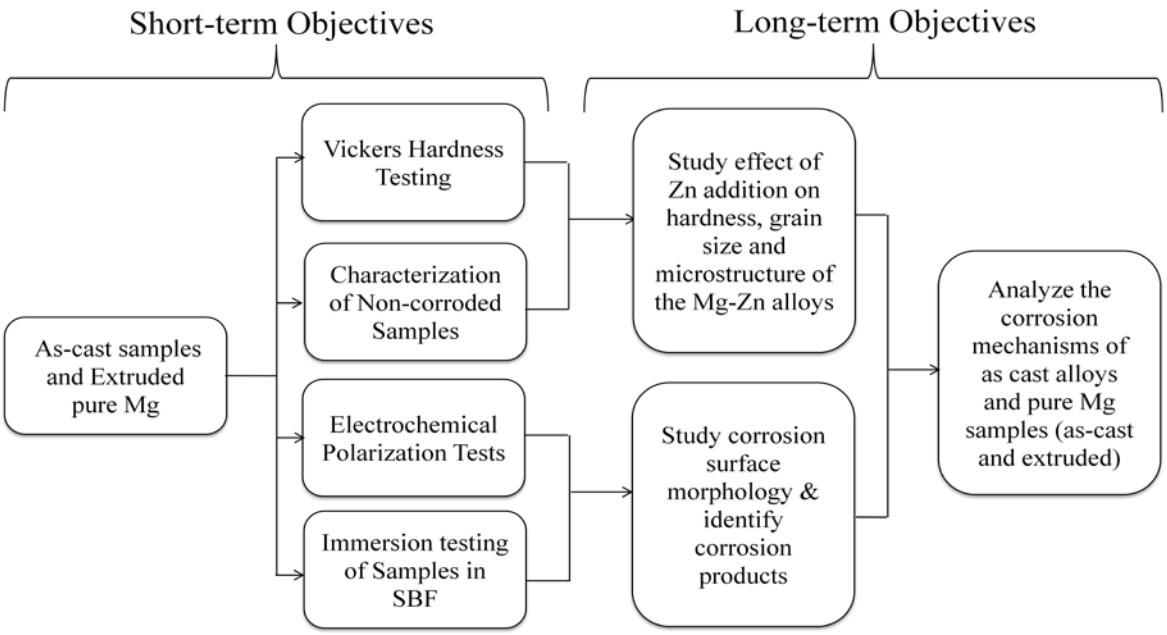

Figure 1.1 Objectives of research

In Chapter 2, a detailed literature review, comprising of recent developments in magnesium-based biomaterials, effects of alloying elements, and corrosion characteristics is presented. In Chapter 3, the experimental approach used in the thesis is described, followed by a discussion of the results in Chapter 4. Finally, the conclusions of the thesis and suggestions for future work are presented in Chapter 5.

Chapter 2 : LITERATURE REVIEW

In this chapter, an overview of traditional orthopaedic materials (non-metallic and metallic) presently used in surgical applications is provided. Then, the history and properties of magnesium and its alloys are discussed, followed by a review of available literature related to *in vivo* and *in vitro* corrosion studies.

2.1. Biomaterials

A biomaterial is defined as any pharmacologically inert material utilized for implantation within a living system to supplement or replace functions of living tissues or organs [2]. A biomaterial thus forms an interface between living and non-living substances. Biomaterials are used in different fields of medicine to serve various functions, some of which are listed in Table 2.1:

Table 2.1 Application of biomaterials in various branches of medicine [2]

Field of medicine	Application of biomaterials
Orthopaedics	Hip and knee implants, tendon and ligament replacement
Dentistry	Dentures, oral cavity implantations, resin
Cardiology	Cardiac stents, heart valves, vascular grafts
Ophthalmology	Lens implants, corneal transplants
Cosmetology	Facial reconstruction, breast prostheses
General surgery	Surgical tapes, sutures

In orthopaedic surgery, the majority of biomaterials are used for mechanical devices for an injured or damaged bone or joint [2]. However, interest in more active materials which could biochemically affect the bone formation process has prompted several studies in this direction [16].

2.1.1. Tissue-material Interaction

The use of any biomaterial is determined by its compatibility with the human body, known as biocompatibility. The definition of biocompatibility itself is quite ambiguous as different sources define the term in different ways [2, 20-22] owing to the evolution in tissue engineering and regenerative medicine. The most recent definition of biocompatibility suggests that "*it is the ability of a biomaterial to perform its desired function with respect to a medical therapy, without eliciting any undesirable local or systemic effects in the recipient or beneficiary of that therapy, but generating the most appropriate beneficial cellular or tissue response in that specific situation, and optimizing the clinically relevant performance of that therapy."* [17]. Ratner [18] defines biocompatibility and biotolerability as contrasting terms accounting for the diametric tissue responses elicited by biochemically reactive and inert biomaterials, respectively.

The human body's immune system rejects foreign entities that are harmful to its functions (e.g. pathogens causing fever). The immune system may also view an implant as a foreign body and may reject the implant. Inert orthopaedic implants made of materials such as stainless steel, titanium alloys, etc., result in a minimal response by forming a thin fibrous tissue around the implant. In contrast, inflammation of the tissue adjacent to the implant is seen in chemically or physically irritating implants [2]. When tissues suffer from chemical, mechanical or thermal trauma, necrosis (cell death) may follow [2].

Depending on the biocompatibility and tissue-material interaction, there are four major groups of biomaterials [2, 19]

(a) Type 1: Inert biomaterials with a smooth surface

Implants fabricated from bioinert materials mostly do not exhibit any sort of chemical reaction when in contact with the body tissue. Only a thin fibrous tissue layer surrounds the bioinert implant, provided that the material used is biocompatible. Metallic materials such as titanium and its alloys, stainless steels, cobalt-chromium alloys, belong to the type 1 category. However, the lack of tissue-implant adhesion may cause loosening of the implant in long-term implantations [2, 19].

(b) Type 2: Inert biomaterials with a porous surface

Bioinert ceramics (e.g., alumina and zirconia) and polymers (e.g., ultra-high molecular weight poly(ethylene) (UHMWPE) and poly(methylmethacrylates) (PMMA)) with a porous surface have been formulated to improve tissue-implant adhesion. The porous surface of these type 2 materials provides a suitable surface for the cells to adhere. Thus, implant stability is greatly improved [2, 19].

(c) Type 3: Biomaterials with controlled reaction surface

These materials interact with the surrounding tissue once they are implanted in the patient's body. These materials are also known as bioactive materials, where the controlled surface reactions promote the structural incorporation of the tissue into the surface layer of the implant. Ceramics like bioglass and ceravital are examples of bioactive materials. Also, metallic inert implants can be coated with bioactive materials, so as to improve cell adhesion and encourage cell proliferation [2, 19].

(d) Type 4: Resorbable biomaterials

Bioresorbable materials degrade in the body over a period of time with the growing tissue replacing the implant. The degradation products are absorbed and/or excreted from the body through metabolic processes. Some of the bioresorbable materials, which are under investigation, are metallic materials (e.g., magnesium and its alloys), biopolymers (e.g., poly(lactic acid) (PLA) and poly(glycolic acid) (PGA)), and ceramics (e.g., β-tricalcium phosphate (TCP) and hydroxyapatite (HAP)) [2, 19].

2.1.2. Orthopaedic Implant Materials

An orthopaedic implant is used to facilitate motion, or align fractured ends of an injured bone to stabilize the affected body part [20]. The three classes of materials used in orthopaedic fracture fixation devices are:

2.1.2.1. Metallic Alloys

Metallic alloys have been used as internal orthopaedic implants and temporary fixation devices due to their high impact strength, wear resistance and non-reactivity in the human

body. Iron (Fe), cobalt (Co), chromium (Cr), and titanium (Ti) can be tolerated in the human body in small amounts, facilitating the use of these elements in the fabrication of metallic bioinert materials to be used in the form of wires, pins, bone plates, screws and intramedullary devices in orthopaedic surgery [20]. Some of the commonly used metallic alloys are:

(a) Stainless Steel

Stainless steel, initially alloyed with vanadium (V) was used for human body implants. However, the amount of V must be controlled due to its impact on increasing the corrosion rate of the implant in the human body [20]. Presently, 316L stainless steel is used as a metallic biomaterial. It has molybdenum additions and a carbon content of 0.03%, which improved the steel's corrosion resistance in chloride solutions [20]. However, even with improved corrosion resistance, the steel has a tendency to corrode in cyclically loaded implants (e.g., lower leg implants) [20]. This may weaken the implant causing secondary fracture and release toxins such as nickel ions (which are known to be neurotoxic) [12].

(b) Cobalt-based Alloys

Broadly known as cobalt-chromium-molybdenum alloys, castable CoCrMo and wrought CoNiCrMo alloys are used as implant materials in high load-bearing applications, such as hip and knee joint prostheses. However, wearing of the implant may result in fragmentation of small particles, which can easily oxidize or corrode, dissolving toxic atoms into the patient's body [20].

(c) Titanium and Titanium-based Alloys

At present, titanium and its alloys are the most commonly used metallic implant biomaterials in orthopaedic surgery due to their low density and high specific strength. The alloys form a passivation layer of TiO_2, which protects the implant against further corrosion [2]. Due to their highly inert nature, Ti and Ti alloys elicit minimal response from the immune system of the body [2]. The most commonly used alloys are commercially pure Ti and Ti6Al4V. However, Ti has a low wear resistance, and aluminum and vanadium are both known to have toxic effects in the human body [12, 21]. Studies with less toxic and biocompatible alloying

elements like silicon (Si) and carbon (C) have been undertaken and the alloys exhibited good mechanical and corrosion properties [22]. However, cytocompatibility testing and *in vivo* tests are required to ascertain their use as biomaterials.

Table 2.2 reveals that all metallic biomaterials currently in use have relatively high elastic modulus. Though it makes the materials strong and there is less probability of fatigue failure, the difference in the elastic moduli of the bone and implant may affect the load transfer through the bone [20]. Human bones have the ability to remodel themselves with respect to the stresses they are subjected to. If an implant with high elastic modulus is used to support bone healing, the applied force transmits through the implant and not through the newly formed bone, causing the bone to have a lower density [5]. This process is known as “stress shielding” and may result in implant loosening, poor healing process, skeletal thickening and inflammation [16].

Metallic alloys are required to have low corrosion rate for use in the human body so that no toxic elements are released and mechanical integrity of the implant is maintained [20, 16]. However, in the case of temporary fixation devices, where the implant is removed after bone healing, it would be advantageous to have biodegradable materials which corrode in the body over a period of time. Such devices would eliminate the need for a second surgery, thus lowering surgery-related complications and reduce health care costs [10].

Table 2.2 Mechanical property comparison of various implant materials [12, 10]

Material		Density (g/cm^3)	Elastic Modulus (GPa)	Yield Strength (MPa)	Tensile Strength (MPa)	Compressive Strength (MPa)	% Elongation	Fracture Toughness ($MPa.m^{1/2}$)
Natural Bone	Cortical bone	1.8 – 2.0	5 – 23	104.9 – 114.3	35 – 283	164 – 240	1.07 – 2.10	3 – 6
	Cancellous bone	1.0 – 1.4	0.1 – 1.57	-	1.5 – 38	-	-	-
Metals	Stainless steel 316L	8.0	193	170 – 310	480 – 620		30 – 40	50 – 200
	Cobalt – chromium alloy	8.3 – 9.2	230	500 – 1500	700 – 1900	450 – 1000	-	-
	Titanium alloy (Ti6Al4V, cast)	4.43	114	760 – 880	830 – 1025	758 – 1117	12	55 – 115
	Mg alloys	1.74 – 2.0	41 – 45	-	185 – 232	65 – 100	2 – 18	15 – 40
Polymers	UHMWPE	-	0.94 – 1.05	39 – 40	-	-	-	-
	D,L – PLA	-	1.9 – 2.4	29 – 35	-	-	5 – 6	-
Ceramics	Synthetic HAP	3.05 – 3.15	70 – 120	-	40 – 200	100 – 900	-	0.7
	Bioactive glass	-	35	-	40 – 60	-	-	-

2.1.2.2. Polymers

Most biodegradable orthopaedic materials used today are thermoplastic polymer materials (e.g., PLA and PGA). These biodegradable polymers are used for fracture fixation devices and in tissue engineering as scaffolds for aiding tissue ingrowth. The presence of biopolymers such as collagens, hyaluronic acids, elastin, keratin, DNA, RNA etc. in the body makes the polymers a highly biocompatible class of materials [20]. Biopolymers degrade as a

result of hydrolysis and enzymatic activity in the human body environment, with the degradation products being resorbed in the body [23]. The use of biopolymers in orthopaedic application is attributed to their biodegradability and the ability to undergo large deformations upon loading, due to the weak van der Waal forces of attraction between the molecules in a polymer chain [2]. However, the use of polymers in load-bearing regions is limited by their lack of sufficient stiffness and strength [2, 9], as seen in Table 2.2. Additionally, the presence of residual monomers due to incomplete polymerization and catalysts used for polymerization may cause irritations in the tissue and need to undergo extensive quality control before being used *in vivo* [20].

2.1.2.3. Ceramics

Ceramics are a preferred class of materials for orthopaedic devices as they have lower elastic modulus than metals, high wear resistance, high strength and are biocompatible [20]. Inert ceramics (e.g., alumina and zirconia) are used in areas with gliding contact (e.g., hip joint [2]) due to their excellent biocompatibility and low friction coefficient [20]. Surface reactive glass ceramic implants (e.g., bioglass and ceravital) strengthen the tissue – implant interface by forming chemical bonds with the surrounding tissues [2]. Completely resorbable ceramics (e.g., TCP and HAP) facilitate easier adhesion to the implant by forming chemical bonds with the hard tissue and degrade in the body over a period of time by completely dissolving, thus leaving behind a newly formed bone. Use of HAP has also shown to aid new bone formation *in vivo* as the bone naturally contains HAP in mineral form [2, 20]. However, in case of load-bearing implants the loss in mechanical property of the implant due to degradation is a deterrent for its use [2, 20]. Though some ceramics exhibit excellent biocompatibility to be used as temporary fixation devices, the brittle nature and low fracture toughness (see Table 2.2) limits their use in load-bearing areas [20].

Another class of new materials, bulk metallic glasses (BMGs) has recently been investigated. They provide excellent mechanical and corrosion properties due to their amorphous nature resulting in controlled corrosion. They combine the properties of glasses, thereby eliminating weak spots such as grain boundaries, with the excellent strength and toughness properties of metals [24]. However, further research is required to confirm the benefits of using these materials in clinical applications.

2.2. Magnesium-based Biodegradable Materials

The interest in the development of magnesium alloys with controlled corrosion rates for use in orthopedic applications is a relatively recent trend [12]. For biomaterials to be used in bone fixation devices, a corrosion rate of 0.5 mm/year in simulated body fluid (SBF) at 37°C along with strength and elongation greater than 200MPa and 10%, respectively, is desired [16]. To be able to successfully use magnesium alloys as bioresorbable metal implants, the time period of degradation should be sufficient to allow the osteoblasts to begin new bone mineralization and deposit an extracellular matrix for their own support before the mechanical integrity of an implant is lost [25]. Alloying, surface modifications, heat treatments have been done in attempt to tailor the corrosion rate of magnesium alloys so as to facilitate slow and uniform corrosion [26].

2.2.1. History

After the first production of metallic magnesium in 1808, the use of magnesium as a biomaterial was experimented as Mg wire ligatures in 1878 to tie bleeding blood vessels [1]. In 1900, the use of magnesium sheets, plates, wires, nails, pegs and pins for joining broken bones with full resorption of the implant after a period of time, was proposed [1]. Subsequent *in vivo* experiments for orthopaedic applications with high purity magnesium sheets and tubes (Chlumsky [1], 1900-1905), pure magnesium plates (Lambotte [1, 10], 1907), Mg-Al-Mn screws, plates, pegs and bands (McBride [1], 1938), Mg-Cd plates and screws (Troitskii and Tristin [10], 1944), and Mg-Al plates and pins (Znameski [10], 1945) were conducted. These tests showed that though the magnesium implants did not cause any inflammation in the tissue or increase the serum magnesium level in the body, it corroded rapidly (at a rate faster than the bone healing rate) resulting in loss of mechanical integrity of the implant [10, 1, 16]. This combined with the emergence of stainless steel and titanium alloys resulted in the investigation of magnesium as a biomaterial to be discontinued [11]. However, the renewed interest in magnesium alloys due to their biodegradable ability has resulted in a number of recent studies [12]. WE43 and AE21 magnesium alloys have recently been clinically tried successfully in humans as a bio-absorbable cardiac stent by BIOTRONIK [16]. Also, the MAGNEZIX screw (Mg-Y-RE-Zr) has recently received the CE mark to be used in medical devices in Europe [16].

2.2.2. Properties

Magnesium, being a lightweight metal with a density of 1.74 g/cm^3 and a tensile strength of ~160 MPa exhibits good strength to weight ratio, making magnesium alloys a popular choice of materials in the automobile and consumer electronics industries [27, 28]. As magnesium and its alloys have an elastic modulus closer to that of the cortical bone (see Table 2.2), they would prevent the "stress shielding" induced by conventional metal implants. Magnesium alloys also exhibit sufficient strength and fracture toughness (see Table 2.2) to be used in load-bearing orthopaedic applications in comparison to polymers and ceramics. Further, the mechanical properties (strength, ductility) of magnesium can be improved by solutionizing, precipitation hardening and alloying [27].

Mg and its alloys are known to corrode in chloride environment of the human body by releasing hydrogen bubbles (which disappear over a period of time [16]), making them a candidate material for temporary fixation devices in orthopaedic surgery [12]. The human body naturally contains ~24 g of magnesium of which 60-70% is located in the bones [13, 29]. The remaining magnesium is absorbed by the intestines and is used by the cellular processes when required [13, 29]. As the kidneys regulate the magnesium content to maintain ionic balance in the human body, the magnesium ions released during implant degradation will likely not cause any harmful reactions [13, 29, 10]. Thus, the use of biodegradable magnesium-based fixation devices could not only prove beneficial for bone healing, but also result in reduced health care costs and benefit the patient since a second surgery to remove the implant may be avoided [10].

2.2.3. Corrosion Behaviour

Due to the high reactivity of pure magnesium owing to its highly negative reduction corrosion potential of -2.37V with respect to the Standard Hydrogen Electrode (SHE), it corrodes readily in an aqueous environment according to Equation 2.1 [16, 9]:

$$Mg_{(s)} + 2H_2O_{(aq)} \rightarrow Mg(OH)_{2(s)} + H_{2(g)} \quad (2.1)$$

$$Anode: Mg \rightarrow Mg^{2+} + 2e^- \quad (2.1(a))$$

$$Cathode: 2H_2O + 2e^- \rightarrow H_2 + 2OH^- \quad (2.1(b))$$

$$Product\ formation: Mg^{2+} + 2OH^{-} \rightarrow Mg(OH)_2 \quad (2.1(c))$$

If the electrochemical reaction given by Equation 2.1 is split into its anodic and cathodic half-cell reactions, then at the anode the metallic magnesium is oxidizing into its ionic form by releasing two electrons (given by Equation 2.1(a)) [30]. Hydrogen gas is released along with hydroxyl ion by reduction of the water molecules with acceptance of the electrons released in the previous step (given by Equation 2.1(b)) [30]. Equation 2.1(c) shows the formation of magnesium hydroxide film on the surface as a corrosion product [30]. It is a passive oxide film, which prevents further corrosion of the underlying magnesium [31, 16].

The evolution of hydrogen gas in large amounts could cause accumulation of gas bubbles at the implant site resulting in blockage of the blood stream, delayed healing and necrosis (cell death) of the tissue [32, 16]. Excessive gas bubbles may even increase the pH of the body fluid next to the implant site affecting the pH dependent physiological reactions and causing alkaline poisoning effect at a pH>7.8 [32]. Some studies, however, report that the hydrogen gas is subcutaneously released from the skin through diffusion into the tissues [4, 16]. *In vivo* tests have shown that the H_2 gas bubbles are seen a few weeks after implantation, but completely disappear by the end of bone healing without causing any inflammation [14, 33, 15]. This could happen when the magnesium-based implant corrodes at a sufficiently slow rate allowing time for diffusion of the gas bubbles [34].

When chloride concentration exceeds 30mmol/L, the $Mg(OH)_2$ protective layer readily reacts with chloride ions present in the surrounding fluid according to Equation 2.2 [31, 33, 16]:

$$Mg(OH)_2 + 2Cl^{-} \rightarrow MgCl_2 + 2OH^{-} \quad (2.2)$$

The $MgCl_2$ is a highly soluble compound, which dissolves in the body fluid. As a result, due to its dissolution more of the metallic magnesium continues to degrade [16]. Pure magnesium undergoes pitting corrosion when exposed to chloride ions in a non-oxidizing medium [30]. As a result, magnesium is rarely used in its pure form, and alloying, surface treatments, anodizing etc. have been employed to control its corrosion rate [25]. Though the above reactions and corrosion mechanism may be true for pure magnesium in an aqueous environment, the same cannot be said for magnesium alloys, as the second phases and intermetallics in the alloy will promote microgalvanic corrosion by acting as cathodic sites

with respect to the Mg matrix (anodic site) [16]. Conductivity of the corrosion medium, potential difference between the anode and cathode, area ratio of cathode to anode are some of the factors which control the galvanic corrosion rate [30]. Corrosion of magnesium alloys in salt solutions is typically highly localized and takes the form of pitting [30].

One of the most common modes of failure of metallic implants is corrosion fatigue, where the implant is simultaneously subjected to cyclic loading and corrosion [16]. The fatigue cracks are found to originate from the corrosion pits and the alloys are found to have lower fatigue limits at lower number of cycles in the simulated physiological environment as compared to tests in air [30, 16]. The second mode is stress corrosion cracking (SCC), where crack propagation usually occurs as transgranular cracking [30, 35]. A study by Choudhary and Raman [35] showed that the AZ91D alloy was more sensitive to SCC in SBF than in air due to the combined effect of anodic corrosion and cracking of the oxide layer by hydrogen evolution.

Processing of the metallic materials also influences the corrosion rates [16]. Studies have shown that extruded and as-rolled materials with finer grain size have better mechanical properties and higher corrosion resistance than as-cast materials [31, 36, 37, 38]. This is due to the higher density of grain boundaries, which not only mechanically strengthen the alloy by impeding dislocation movement, but also reduce the corrosion rate, the reason for which is still unclear [16]. Though it seems from these results that a finer grain size corresponds to lower corrosion rate, it is not always the case. Wang *et al*. [16] found that although ECAPed AZ31 had a finer grain size in comparison to as-rolled AZ31, there was no significant change in the corrosion rate. A study by Chou *et al*. [39] on Mg-Y-Ca-Zr alloys showed that a heat treated alloy has better corrosion resistance even though it has a larger grain size in comparison to the as-cast alloys. One possible explanation was that the decrease in microgalvanic corrosion due to dissolution of the secondary phases into the matrix on heat treatment of the alloys influences the corrosion rate [39, 16].

2.3. Magnesium Alloys

Alloying of magnesium is one of the techniques to improve the corrosion resistance of pure Mg [26]. Apart from corrosion, alloying also increases strength and ductility of the material

by solid solution strengthening, precipitation hardening and grain refinement [16]. The hexagonal close packed crystal structure and small atomic diameter of Mg permit it to form solid solutions with many elements [16]. However, the most common alloying elements in magnesium for implant applications are Al, Mn, Zn, Ca, lithium (Li), zirconium (Zr), yttrium (Y), and some REEs [12]. The concentration of the alloying elements can be chosen based on analysis of the phases and intermetallics indicated in the appropriate phase diagram.

The Mg-Al alloy system is the most common and commercially used alloy system. Aluminum improves corrosion resistance and increases strength of Mg [16]. In Mg-Al alloys, pitting corrosion is observed due to selective attack along the $Mg_{17}Al_{12}$ network which is followed by the undercutting and falling out of grains [30]. However, aluminum is a neurotoxic element known to cause dementia [32] and Alzheimer's disease [12, 9]. Zinc, calcium, and manganese are biocompatible elements and can be used in limited quantities for alloying with magnesium [9]. The following discussion will focus on Mg-Zn alloy system as the other systems are out of the scope of this thesis.

2.3.1. Mg-Zn Phase Diagram

The effect of zinc on magnesium can be examined via the Mg-Zn binary phase diagram (Figure 2.1). The Mg-Zn binary phase diagram has two terminal solid solutions and five intermetallic phases listed in Table 2.3 [40]. The maximum solid solubility of Zn in Mg is 6.2 wt.%.

The stoichiometry of the Mg_7Zn_3 phase has been corrected to $Mg_{51}Zn_{20}$, after X-Ray Diffraction (XRD) studies done by Higashi *et al.* [41]. Also, the $MgZn_2$ phase was confirmed to be an intermediate solid solution [41].

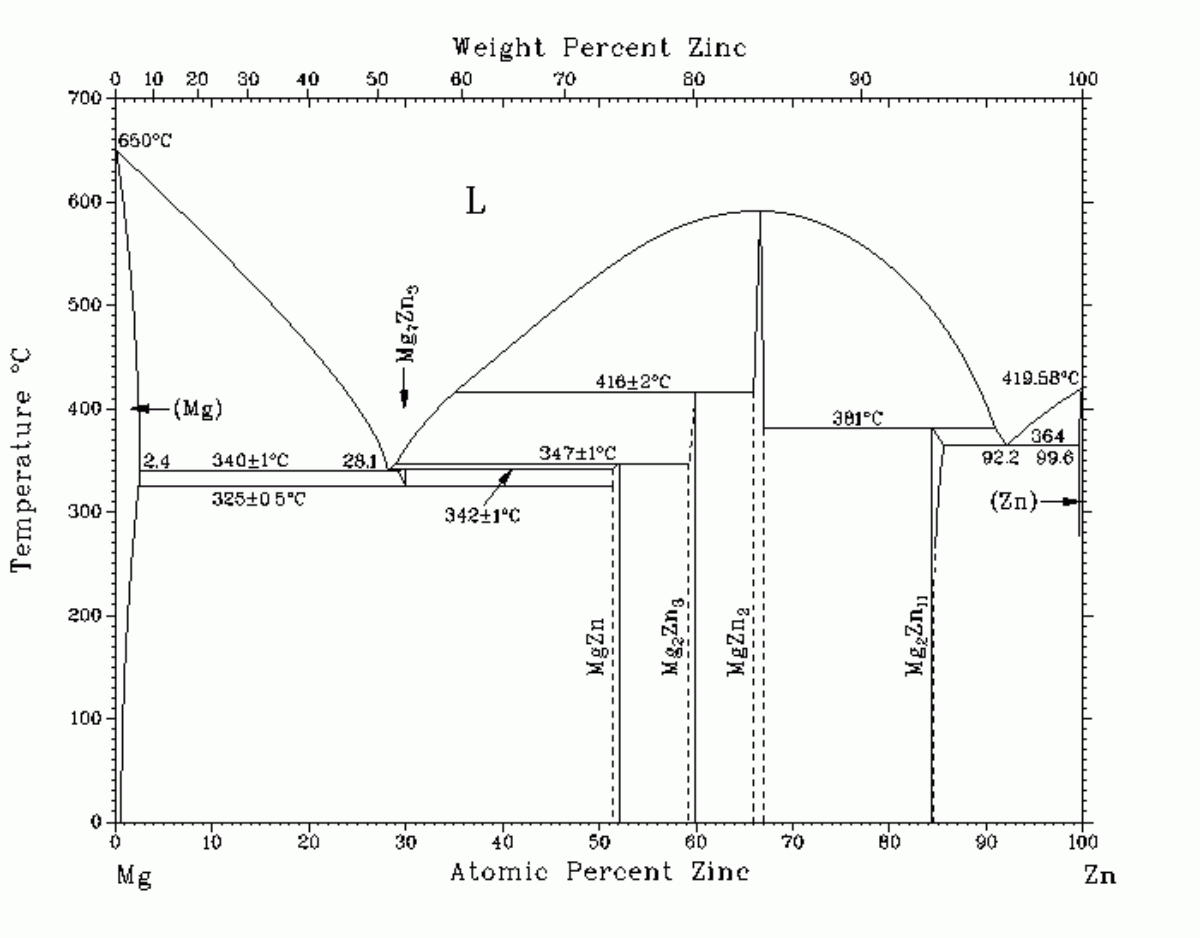

Figure 2.1 Magnesium-Zinc phase diagram [42]

Unlike most binary alloy systems, the Mg-Zn system exhibits a divorced eutectic reaction, where dendritic solidification is seen with the $Mg_{51}Zn_{20}$ forming the interdendritic phase between the α(Mg) matrix, as seen in Figure 2.2 [43, 44]. This occurrence can be explained thermodynamically by a total reduction in surface free energy [45]. In heterogeneous nucleation, surface energies of the different interfaces play a role in determining the critical free energy or activation energy required for a transformation to occur. The alloy system tries to lower the net free energy by choosing the interface with the lowest surface free energy, which in this case appears to be the liquid - $Mg_{51}Zn_{20}$ interface, facilitating the nucleation and growth of the $Mg_{51}Zn_{20}$ phase first. The remaining liquid then solidifies to form α(Mg) matrix [45].

Table 2.3 Phases present in the Mg-Zn binary phase diagram [40]

Phase	Composition (in wt. % of Zn)
α(Mg)	0 - 6.2
$Mg_{51}Zn_{20}$	53.6
MgZn	74.0
Mg_2Zn_3	80.1
$MgZn_2$	84 - 84.6
Mg_2Zn_{11}	93.7

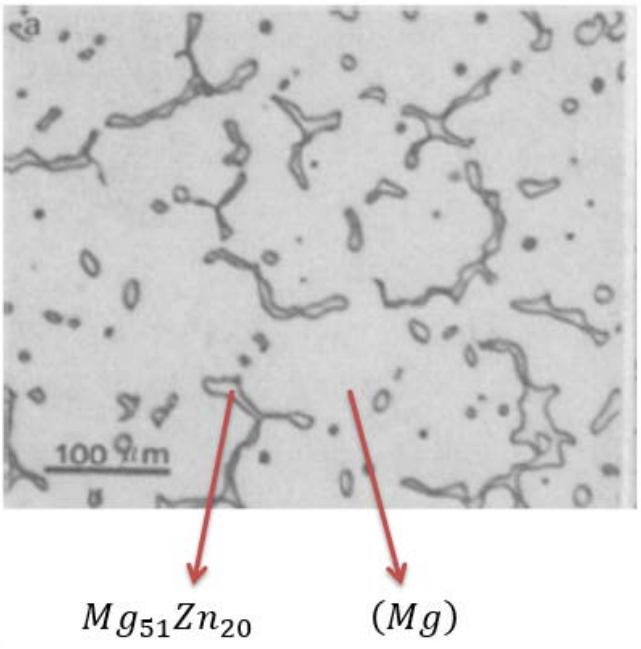

Figure 2.2 Optical Micrograph of Mg-9Zn (hypoeutectic) alloy with $Mg_{51}Zn_{20}$ particles in α(Mg) matrix [43]

The $Mg_{51}Zn_{20}$ phase decomposes into eutectoid products α(Mg) and MgZn, at 325°C and 53.6 wt. % Zn [42]43. In eutectoid reactions the structure and composition of the products are different from the parent phase. The eutectoid products may appear as alternating lamellae or

granular structures [43]. According to the equilibrium phase diagram, the $Mg_{51}Zn_{20}$ phase should disappear below the eutectoid temperature. However, depending on cooling rate and alloy composition, the $Mg_{51}Zn_{20}$ phase may be found in the interdendritic regions of the alloys at room temperature [43]. Interestingly, it was found by Zhang *et al*. [33] that the interdendritic phase, MgZn disappears completely upon heat treatment of the hypoeutectic alloy, as seen in Figure 2.3. This disappearance of the interdendritic phase on heat treatment was also confirmed by Wei *et al*. [43], and was related to the metastable nature of MgZn phase (which is unstable below 315°C). The decomposition results in the formation of a stable intermediate equilibrium phase, $MgZn_2$ [43].

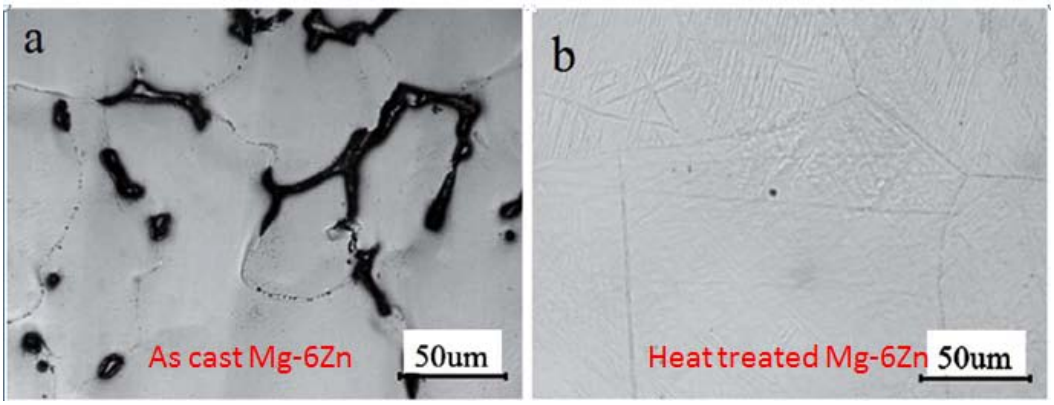

Figure 2.3 (a) The dark regions are the interdendritic phase in as-cast Mg-6Zn; (b) After heat treatment uniform microstructure is observed with complete disappearance of interdendritic phase [33]

2.3.2. Effect of Zn on the Mechanical and Corrosion Properties of Mg Alloy

Zn is known to decrease the corrosion rate as well as improve the strength and ductility of the magnesium alloy [16]. In concentrations lower than 2 wt. % of Zn, the strength of the alloy is improved due to solid solution strengthening [12]. A study by Zhang *et al*. [36] showed the reduction in average grain size with increasing concentration of Zn in the Mg-Zn-Mn alloy. This refining ability of zinc can be related to the Growth Restriction Factor (GRF), which has been calculated from the Mg-Zn binary phase diagram to be 5.31 (higher than that of aluminum (4.32)) [36, 16]. However, in another study, with increasing concentration of Zn there was no significant change in the average grain size, though the grain sizes within each alloy were found to be highly inhomogeneous [46]. Though increasing Zn concentration reduces grain size and improves the strength of the Mg alloy according to the Hall Petch

relationship, Zn also lowers the corrosion resistance of the alloy from 12.35 to 4.54 kilo-ohms [36, 16].

The mechanical properties of Mg-Zn alloys can be further be improved by age hardening [47, 27]. Brar *et al*. [25] observed localized pitting corrosion on the ZX152 alloy which they compared to the microgalvanic and preferential corrosion exhibited by AZ91. The occurrence of microgalvanic corrosion was later confirmed by Song *et al*. [46] in their study of Mg-xZn (x = 2,3,4,5 wt. %) alloys, which showed that since corrosion is an electrochemical process, the Mg-Zn phases (which formed in the alloys) act as micro-cathodic sites and the primary Mg matrix acts as micro-anodic site. Thus, the Mg matrix may corrode with respect to the Mg-Zn phases and the corrosion rate increased with increasing additions of zinc as the volume fraction of the Mg-Zn phases increased [46]. In Mg-Zn alloys, with the evolution of the second phases the effect of microgalvanic corrosion is less pronounced since the potential difference between the anode and the cathode is lowered [48, 16, 30]. In Mg-Ca binary alloys, it was seen that additions of Zn improved the tensile strength, yield strength, and ductility due to grain refinement. Also, Zn significantly reduced the corrosion rate due to the formation of the $Ca_2Mg_6Zn_3$ phase, which prevented the excessive pitting corrosion of Mg_2Ca phase [51-53]. However, the Zn:Ca atomic ratio played an important role on the corrosion properties of the alloy [49, 50]. It was found that the alloy with the lowest Zn:Ca ratio exhibited the highest corrosion resistance due to the formation of the eutectic (α(Mg) + Mg_2Ca + $Ca_2Mg_6Zn_3$) phase, where the α(Mg) acted as the cathode and Mg_2Ca acted as the anode, corroding the Mg_2Ca phase completely [49]. Then, the $Ca_2Mg_6Zn_3$ phase acted as the cathode and the α(Mg) acted as the anode resulting in corrosion of the matrix [49]. A similar observation was reported in another study [51]. In a study conducted by Zhang *et al*. [50], the increasing additions of zinc content considerably improved the mechanical properties upto 4 wt. % of Zn. However, the corrosion rate of the alloys increased with zinc additions, possibly due to the formation of more microgalvanic couples [50].

2.4. Corrosion Testing

Corrosion testing of magnesium is done *in vitro* in simulated conditions in the laboratory and if the alloy is biocompatible *in vivo* corrosion testing is conducted in animal models.

2.4.1. *In vitro* Tests

Immersion testing and electrochemical testing (polarization and Electrochemical Impedance Spectroscopy) are the common methods of corrosion testing of materials in the laboratory [12]. The calculation of corrosion rates from both the techniques is defined by ASTM standards, G31-2012a [52] and G102-89 [53], respectively. The degradation rate of material for immersion testing can be calculted either by using the weight loss measurement or by measuring the volume of hydrogen released during the chemical reaction which is a direct measure of the amount of dissolved magnesium [54]. However, there is a possibility of leak of the hydrogen gas and changes in atmopheric pressure may hinder the measurement [12]. It is also observed that the rate of degradation reduces when the material is tested over a period of time, possibly due to formation of insoluble corrosion products on the sample surface [25, 54]. To simulate the human body environment, studies have incorporated dynamic electrolyte movement apart from maintaing the fluid at the physiological temperature and pH [54]. The temperature at which the experiment is conducted is another important parameter, which is to be controlled during *in vitro* testing as there is an increase in corrosion rates by about 100% when testing at 37°C as compared to 20°C [55].

Studies on corrosion rates in different corrosion media (e.g., Hank's solution, Simulated Body Fluid, Phosphate Buffred Saline etc.) are available in literature [12, 54, 33, 39]. The primary difference between them is the presence of different amounts of inorganic and organic ion concentrations. The concentration of inorganic ions in SBF is similar to that in the body plasma [54]. The inclusion of proteins, like albumin and amino acids in the corrosion medium is also known to affect the corrosion rate significantly [54, 55]. A study conducted by Walker *et al.* [56] found that the *in vitro* corrosion rates of magnesium alloys in Earle's Balanced Salt Solution, without any protein content, were comparable to the *in vivo* corrosion rates. Contrastingly, the corrosion rates obtained in media containing proteins had significantly higher corrosion rates compared to the *in vivo* tests [56]. The effect of protein on Mg alloy corrosion is not yet clearly understood [56], but the significant variation in corrosion rates in different media necessitates the need of a universal corrosion testing protocol specifically for Mg and its alloys [54].

2.4.2. *In vivo* Tests

Many studies with testing of magnesium alloys on different animal models (e.g., rats and rabbits) have been conducted [15, 14, 33, 34, 39]. *In vivo* testing provided an atmosphere with varying load cycles, dynamic circulation of fluid, and presence of different biological molecules, thus making the corrosion testing more valid for use in the human body. However, it was found that testing of materials in different animal models at different locations rendered the various studies incomparable with regard to their corrosion rates [12]. Many *in vivo* studies with magnesium alloys showed that magnesium alloys facilitated the adhesion of cells and formation of new bones [15, 33, 14]. Further details on *in vivo* testing are out of the scope of this thesis.

2.5. Chapter Summary

The above studies suggest that magnesium alloys are possible candidate materials for use in orthopaedic surgery as temporary fixation devices. Zinc was chosen as an alloying element owing to its biocompatibility in the human body and grain refining ability so as to improve both the mechanical and corrosion properties of the alloy. In this research, zinc concentrations of 1, 1.5, 2, and 5 wt. % were chosen for alloying to study the corrosion behavior of the alloys. Immersion tests and electrochemical test were done to study the corrosion rates in Simulated Body Fluid (SBF) in the absence of proteins.

Chapter 3 : EXPERIMENTAL PROCEDURE

This chapter describes the procedures carried out during casting of Mg-Zn alloys, sample preparation methods and the various characterization techniques carried out in this research. The procedure carried out for performing the corrosion experiments and the post-corrosion analysis is detailed.

3.1. Materials and Casting

The materials used in this thesis are given in Table 3.1. All the compositions are given in weight percent.

Table 3.1 Designation of samples

Material		**Designated Name**	**Elemental Composition (wt%.)**	
			Zn	**Mg**
Commercially pure (CP) magnesium	Extruded (as-received)	Ex Mg-CP	0	Bal.
	As-cast	AC Mg-CP	0	Bal.
Mg-1.0Zn		Z1	1.0	Bal.
Mg-1.5Zn		Z1.5	1.5	Bal.
Mg-2.0Zn		Z2	2.0	Bal.
Mg-5.0Zn		Z5	5.0	Bal.

Commercially pure Mg in its extruded form was obtained as 1 lb. magnesium sticks (99.8% pure) along with 50 lb. zinc ingot (99.99% pure) from Belmont Metals Inc. (New York, USA). All alloys were cast using permanent mould casting at the Casting Laboratory, UBC, Kelowna, Canada. For each of the alloys, the Ex Mg-CP was melted in a steel crucible and calculated amount of zinc was added to the melt and stirred at about 750°C and held for five minutes. As shown in Figure 3.1(a), the molten alloy was poured into graphite dies (4” height and 1” diameter) and allowed to solidify. A photograph of the as-cast sectioned specimen of the Z2 alloy is shown in Figure 3.1(b). All the melting and castings were carried out under a protective carbon dioxide atmosphere [33].

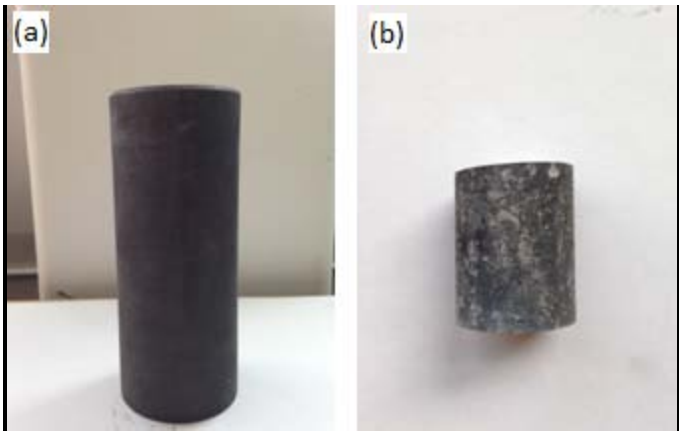

Figure 3.1 Photographs of (a) graphite die used for casting; (b) as-cast sectioned specimen of Z2 alloy

As shown in Figure 3.2, two discs of about 15mm thickness were cut from one end of the as-cast rods of each alloy using Baincut cut-off saw (Chennai Metco Pvt. Ltd., India), at the Materials Science and Engineering Department, IIT Kanpur, India. One of the discs was used for electrochemical studies, while the other disc was further cut into four quarters using a Baincut low speed saw (Chennai Metco Pvt. Ltd., India). One quarter was used for metallographic characterization and the remaining for immersion testing. A third disc was cut from the remaining rod using a lathe at the Machine Shop, UBC, Kelowna, Canada for Vickers hardness testing.

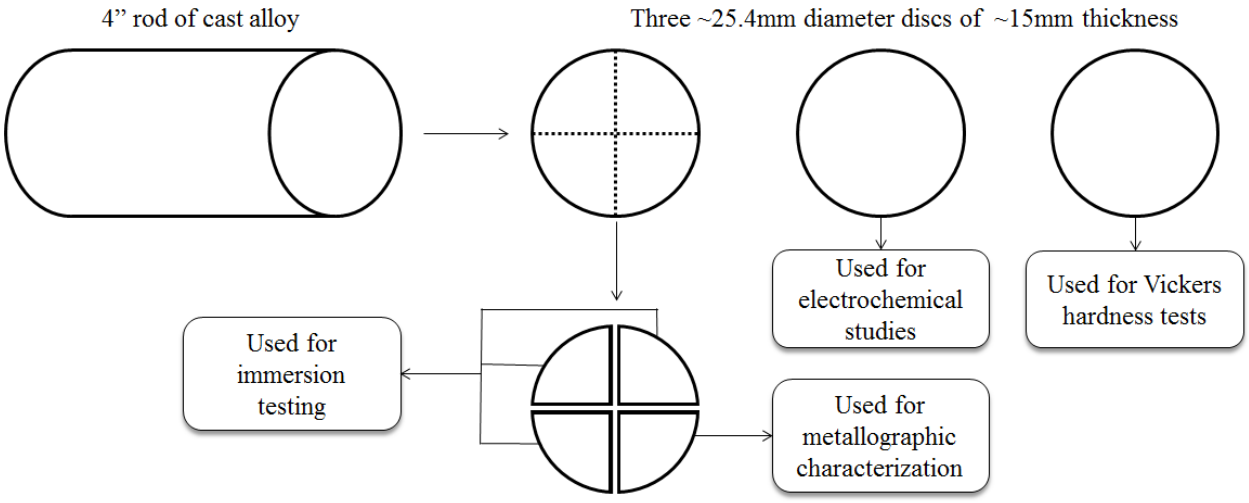

Figure 3.2 Schematic of cut samples used for further study

3.2. Material Hardness

All samples were polished with 600 grit SiC papers. Hardness tests were conducted using a Buehler Automatic Vickers Hardness Tester, model Wilson VH 3100. 10 indentations were made along the diameter of the sample, as shown in Figure 3.3. A load of 0.05 kgf was applied for a dwell time of 10 seconds.

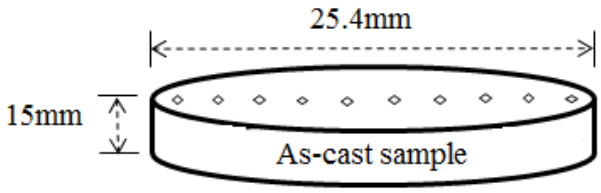

Figure 3.3 Schematic of sample cross-section showing the Vickers hardness indentations along the diameter

3.3. Characterization Techniques

For microscopy and compositional analyses, the samples were polished with SiC paper up to 1200 grit and then cloth polished with diamond pastes and colloidal silica to obtain a mirror finish. The samples were then etched in Kroll's reagent (92 ml distilled water, 6 ml Nitric acid, and 2 ml Hydrofluoric acid) for 10 seconds and stored in a vacuum sealed desiccator before microstructure analysis. The following techniques were used for characterization of the polished sample:

3.3.1. Light Optical Microscopy

Zeiss A1m microscope, fitted with a Zeiss AxioCam MRc digital camera at the Material Testing Laboratory (IIT Kanpur, India) was used for taking optical images of the etched samples.

3.3.2. Scanning Electron Microscopy and X-Ray Energy Dispersive Spectroscopy

The etched samples were observed with a Scanning Electron Microscope (SEM) with an X-Ray Energy Dispersive Spectroscopy (X-EDS) attachment. Carl Zeiss EVO 50 SEM was used in back scattered electron (BSE) mode to analyze the samples before corrosion at the SEM Facility, Materials Science and Engineering Department (IIT Kanpur, India). After immersion corrosion tests the samples were chemically cleaned and the corroded surface was

analyzed with a Jeol JSM-T100F Field Emission SEM at the Advanced Centre for Materials Science (IIT Kanpur, India). The corroded surfaces of the samples after electrochemical studies were analyzed using the SEM facility at UBC (Kelowna, Canada) using a Tescan Mira3 XMU SEM with Oxford X-max X-EDS detector.

3.3.3. X-Ray Diffraction

Bruker D8 X-Ray Diffractometer (XRD) shown in Figure 3.4, at the Department of Materials Science and Engineering (IIT Kanpur, India), was used to detect the phases present in the studied alloys before and after immersion corrosion tests of all the samples. The 2θ range was set between 30° – 90° at a scan rate of 0.3 seconds/step with a Cu target.

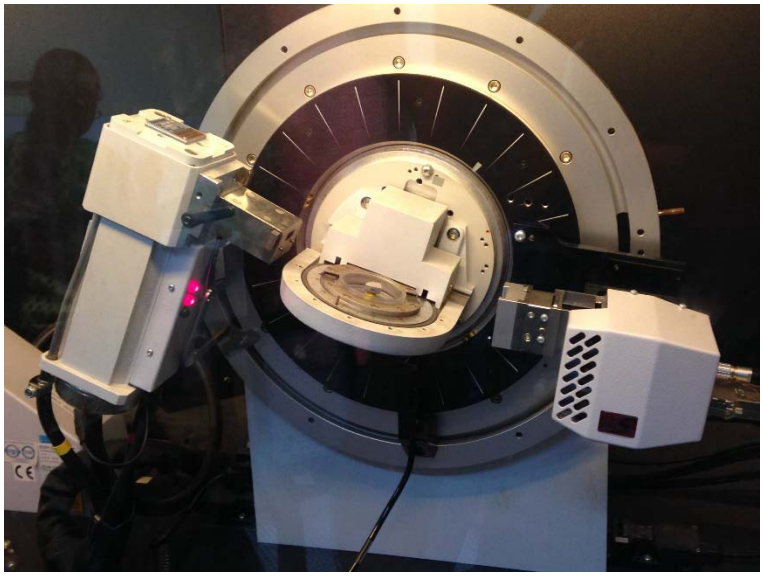

Figure 3.4 Bruker D8 X-Ray Diffractometer

The XRD data were plotted in Origin 8.5 and the indexing was done by comparing the data with existing standard diffractograms available in JCPDS (Joint Committee on Powder Diffraction Standards) and ICSD (Inorganic Crystal Structure Database) databases using X'Pert HighScore software.

3.4. Corrosion Testing

In vitro degradation properties of all samples were evaluated by conducting immersion and electrochemical polarization tests to calculate the corrosion rate and understand the corrosion

behaviour of the alloys. All corrosion experiments were conducted in the Non Equilibrium Processing and Corrosion Laboratory (IIT Kanpur, India).

3.4.1. Solution Preparation

Simulated Body Fluid (SBF) solution was chosen as the corrosion medium for both immersion and electrochemical tests, as it has previously been used in many studies [19, 35-37]. The concentrations of chemicals used to prepare the SBF were adapted from Zhang *et al.* [33] and are presented in Table 3.2. A large 5L flask was filled with distilled water along with a thermometer to monitor the temperature of the SBF during preparation. The temperature of the stirrer was set to 38 ± 1°C, as this was when the thermometer placed in the flask indicated a temperature of 37 ± 0.2°C, which is in the human body temperature range [57]. Each chemical in Table 3.2 was successively added to the distilled water after the previous chemical dissolved. After all the chemicals were added, the pH of the SBF was adjusted to 7.4 by adding required amounts of 1M HCL and NaOH pellets, respectively.

Table 3.2 Chemical quantities for preparation of 1L of SBF [33]

Chemical	NaCl	$CaCl_2$	KCl	$MgSO_4$	$NaHCO_3$	Na_2HPO_4	NaH_2PO_4
Amount (g/L)	6.8	0.2	0.4	0.1	2.2	0.126	0.026

3.4.2. Immersion Tests

The discs sectioned from the pure Mg (extruded and as-cast) samples and each alloy composition (one specimen shown in Figure 3.5(a)) were further cut into four quarters. Each quarter of the specimen were appropriately polished, ultrasonically cleaned in acetone and weighed. They were circumferentially covered with Teflon tape, as shown in Figure 3.5(b), so as to limit the exposed surface area for corrosion to the two quarter-circle faces only. All eighteen samples were immersed completely into 200mL of SBF (pre-heated to 38 ± 1°C) and were placed in a water bath (shown in Figure 3.5(c)) for an exposure time of 10 days. The temperature of the water bath was set such that the internal temperature of the water after heat loss varied in the range of 37.3 ± 0.3°C which is within the physiological human body temperature range [57].

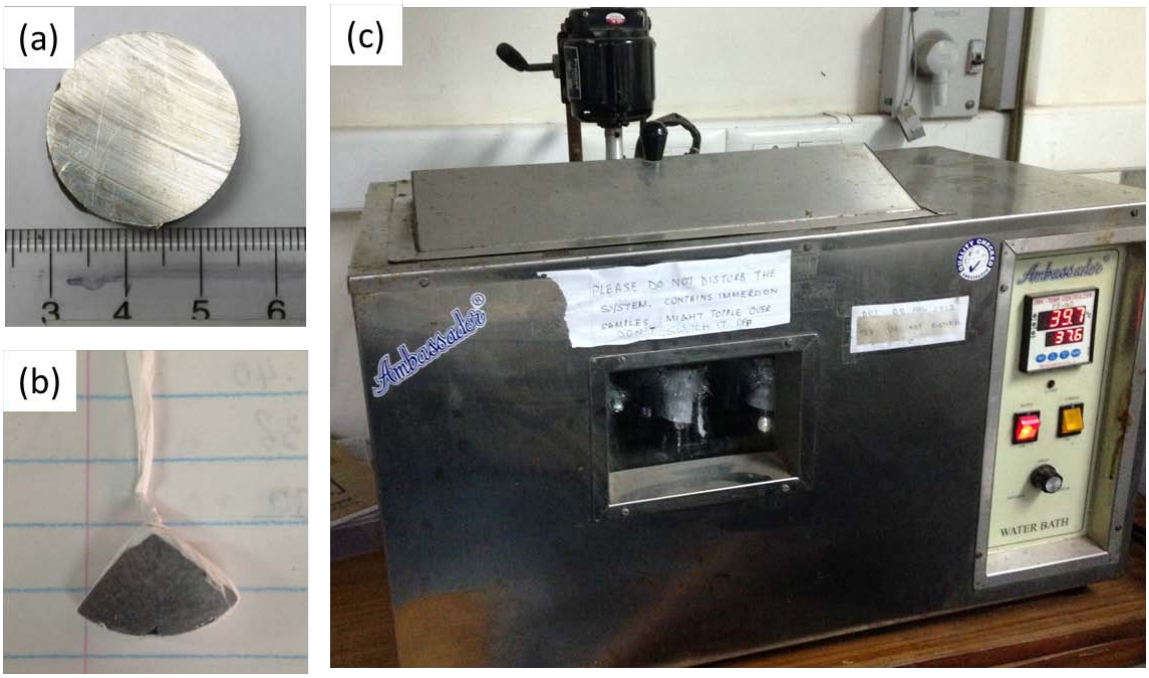

Figure 3.5 Photographs of (a) specimen of disc sectioned from as-cast ingots and Ex Mg-CP; (b) specimen of cut sample used for immersion tests with Teflon tape covering the sides; (c) temperature controlled water bath

After the exposure time was complete, the samples were removed from the conical flasks and ultrasonically cleaned in acetone. To remove the oxide layer, a chemical solution (prepared with 1.69M chromium trioxide, 0.058M silver nitrate and 0.076M barium nitrate dissolved in distilled water) was used [27]. The weight of the samples was measured after corrosion product removal. The weight loss for the samples was calculated as the difference between the initial and the final weights.

The immersion corrosion rates were calculated according to ASTM G31-12a [52] by Equation 3.1:

$$Corrosion\ Rate = \frac{K \times W}{A \times t \times D} \tag{3.1}$$

where, *'W'* was the weight loss in grams (g), *'A'* was the surface area exposed to the test solution in sq. centimeters (cm^2), *'t'* was the time of exposure in hours, *'D'* was the density of the sample in grams per cubic centimeter (g/cm^3), and constant *'K'* = 8.76×10^7 for converting the corrosion rate units from cm/h to µm/y [52].

3.4.3. Post-corrosion Characterization

3.4.3.1. X-Ray Diffraction and SEM – X-EDS

Before removal of the corrosion products, all samples were characterized using the Bruker D8 X-Ray Diffractometer (XRD) in order to identify the corrosion products. The corroded surface morphology of each alloy sample was studied under a Scanning Electron Microscope.

3.4.3.2. Fourier Transform Infrared Spectroscopy

The precipitates left over at the bottom of the conical flasks at the end of the immersion test were filtered out using filter paper, air dried, and subjected to Fourier Transform Infrared Spectroscopy (FTIR). 3mg of the filtrate was mixed with 50mg of dried IR grade Pottasium Bromide (KBr) and ground to a fine size. Pellets of ~1mm thickness were made by applying suitable pressure and equal amount of filtrate was used in preparing the pellet in each case, which allowed the determination of the relative amount of the different phases. The FTIR spectra were obtained using a Perkin Elmer FTIR system at an acquisition rate of 16 spectra/second. The obtained spectra for the filtrates from the alloys and the pure Mg (extruded and as-cast) samples were plotted in Origin 8.5 and compared with available literature to identify the characteristic peaks.

3.4.4. Electrochemical Studies

The electrochemical tests were conducted using an electrochemical cell and potentiostat, interfaced with a computer. The electrochemical cell consisted of three electrodes, as shown in Figure 3.6. The working electrode was the sample being tested. The Saturated Calomel Electrode (SCE) with an electrode potential of 0.241V was used as the reference electrode with respect to which the potential of the working electrode was measured. The third electrode was an inert platinum mesh counter/auxiliary electrode, which allowed a path for current to flow out from the working electrode.

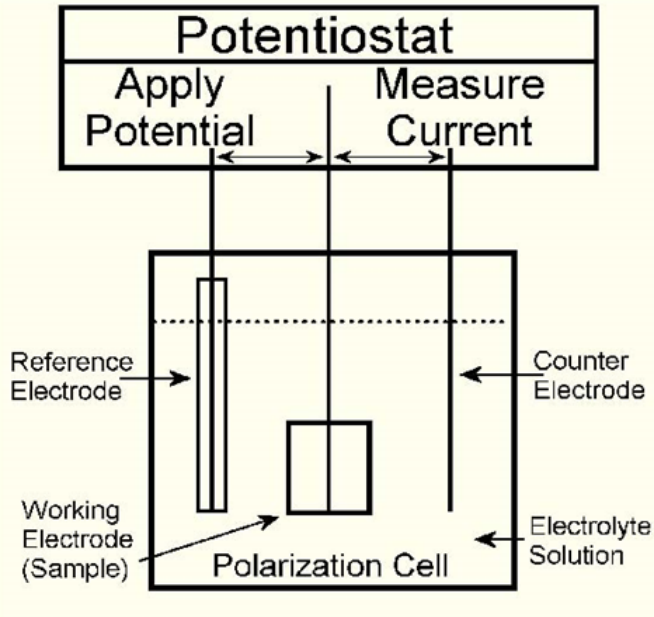

Figure 3.6 Schematic of Electrochemical cell and Potentiostat [58]

Potentiostat Model 2263 PARSTAT (Princeton Applied Research, USA) was used to conduct the potentiodynamic polarization tests and the electrochemical impedance spectroscopy tests. PowerSuite (version 2.58) software was used to drive the potentiostat and collect the experimental data. The setup of the electrochemical experiment is shown in Figure 3.7.

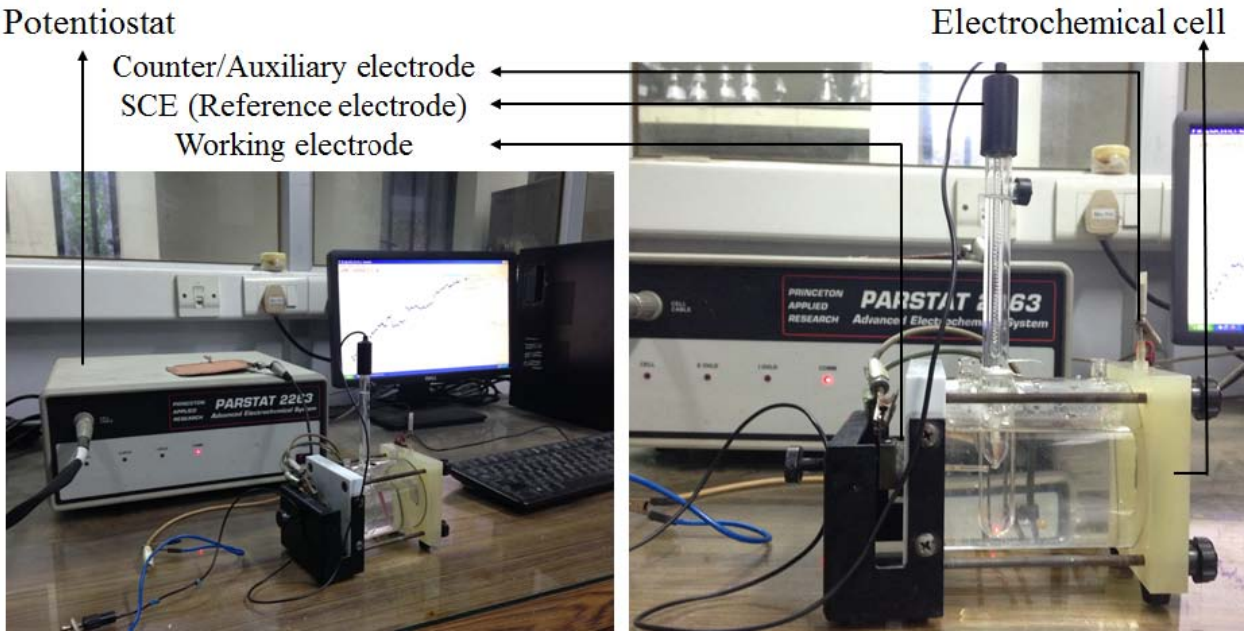

Figure 3.7 Photographs of the electrochemical cell setup

The polished disc of each sample was ultrasonically cleaned in acetone before it was affixed to the cell. The prepared SBF was filled in the cell as an electrolyte. Four probes from the potentiostat were then connected to the electrodes and a fifth probe was grounded. All the polarization and EIS experiments were conducted in ambient room temperature and in a freely aerated SBF solution. Both polarization and EIS tests were repeated three times for each of the alloy samples. Fresh SBF solution was used for every run of the electrochemical test.

3.4.4.1. Tafel Polarization

The open circuit potential (OCP) of the cell was obtained for one hour, by switching on the potentiostat without applying any potential. OCP was the potential of the working electrode with respect to the reference electrode in the absence of applied potential. This was done to ensure that the surface corrosion reactions have attained a constant rate indicating a stable OCP. The Tafel polarization tests were conducted from 250 mV below the OCP to 250 mV above the OCP at a scan rate of 0.166mV/s. A plot between the applied potential (E) and logarithm of current density (log i) was obtained. These curves were extrapolated to obtain the corrosion current density (i_{corr}), which was a direct measure of the corrosion rate of the sample, as given by Equation 3.2 obtained from Faraday's Law [53]:

$$Corrosion\ Rate = \frac{K_1 i_{corr}(EW)}{\rho} \tag{3.2}$$

where, 'i_{corr}' was in µA/cm^2, '*EW*' was the equivalent weight of metal being tested which is equal to 12.15 (dimensionless quantity) for Mg and its alloys, and 'ρ' was the density of the sample in g/cm^3. The constant 'K_1' had a value of 3.27x10^{-3} mm.g/µA.cm.y to obtain the corrosion rate in mm/y [53]. It was converted to µm/y by multiplying the right side of Equation 3.3 by 10^3.

3.4.4.2. Electrochemical Impedance Spectroscopy Tests

Electrochemical Impedance Spectroscopy (EIS) tests were performed using the same setup on the same samples after letting them stabilize in the SBF and attain OCP. An excitation AC signal of 10mV was applied to the cell and the impedance spectrum was measured between the frequency range of 100kHz to 10mHz with 36 data points being recorded for each

experiment. ZSimpWin (version 3.10) software (EChem Software, Ann Arbor, USA) was used for curve fitting of the EIS plots. Analysis of the Nyquist, Bode phase and Bode magnitude plots yielded the best fit circuit for the electrochemical interface between the metal/alloy and the electrolyte.

3.5. Chapter Summary

The flowchart presented in Figure 3.8 summarizes the experiments carried out on the alloys and pure Mg (extruded and as-cast) samples.

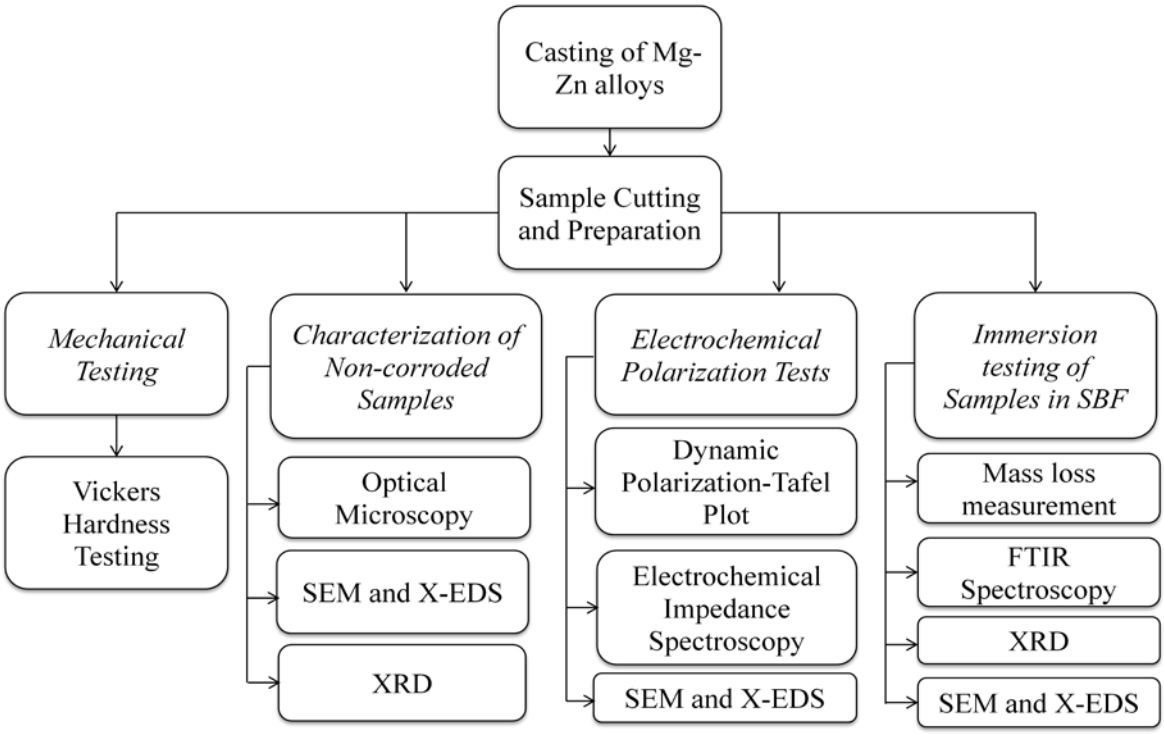

Figure 3.8 Flowchart summarizing the experiments conducted in this thesis

Chapter 4 : RESULTS AND DISCUSSIONS

This section presents the results obtained during the course of the thesis research. All the results are discussed in the order in which the experiments were conducted, as described in Chapter 3 of this thesis.

4.1. Casting of Alloys

During the casting of the molten alloy, care had to be taken to minimize exposure of liquid magnesium to ambient air. Oxidation of liquid Mg was observed during the melting and the pouring stage. As a result, it was possible that some magnesium oxide was introduced into the mould. Further, the cast ingots had a dark gray coloration on the outer surface, as seen in Figure 4.1. This was likely due to carbon diffusion from the uncoated graphite die onto the alloy surface during solidification.

Centerline porosity was observed in one of the as-cast alloys (see Figure 4.1(b)). This centerline porosity was the result of turbulent liquid metal flow from the crucible into the mould. With the turbulence, air trapped in the liquid melt remained in the casting. Although macroporosity was not generally observed with the naked eye in the castings, microporosity might have been induced in the sample leading to inhomogeneity in the as-cast alloys.

Figure 4.1 Photograph of as-cast specimens of (a) Mg-CP; (b) sectioned specimen of Z2 with a macro-pore

X-EDS analysis on the matrix grains of the as-cast alloys revealed that Zn atoms entered into the solid solution, as seen in Figure 4.2. A higher content of Zn was found in the interdendritic regions than in the matrix, indicating that the rapid solidification rate did not allow sufficient time for homogenous diffusion of all solutes. Despite the inhomogenity in the as-cast samples, their bulk compostion, shown in Figure 4.2 corresponded to their nominal composition, thus validating the preparation method used.

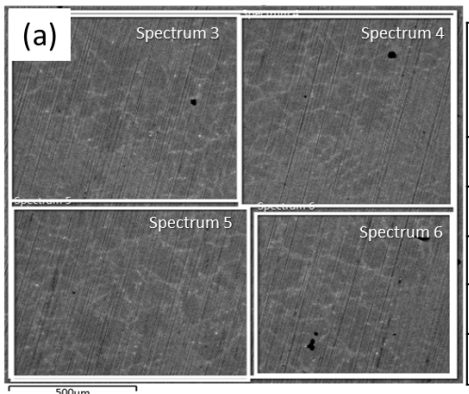

Element	Spectrum 2	Spectrum 3	Spectrum 4	Spectrum 5	Spectrum 6
	(weight %)				
C	6.4	5.2	5.5	6.0	6.0
O	2.0	2.1	2.0	2.1	2.2
Mg	90.6	91.6	91.5	90.8	90.8
Zn	1.0	1.1	1.0	1.1	1.0
Total	100.0	100.0	100.0	100.0	100.0

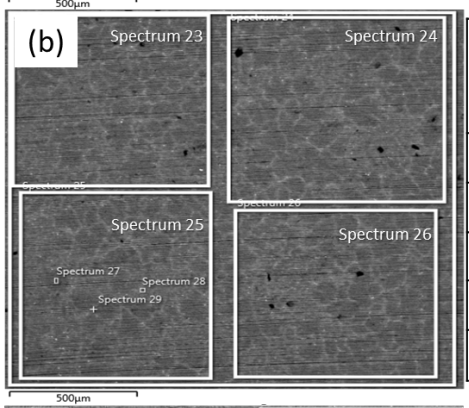

Element	Spectrum 22	Spectrum 23	Spectrum 24	Spectrum 25	Spectrum 26
	(weight %)				
C	13.5	13.6	13.6	13.6	13.7
O	2.5	2.5	2.3	2.5	2.5
Mg	82.6	82.6	82.8	82.5	82.5
Zn	1.4	1.3	1.3	1.4	1.3
Total	100.0	100.0	100.0	100.0	100.0

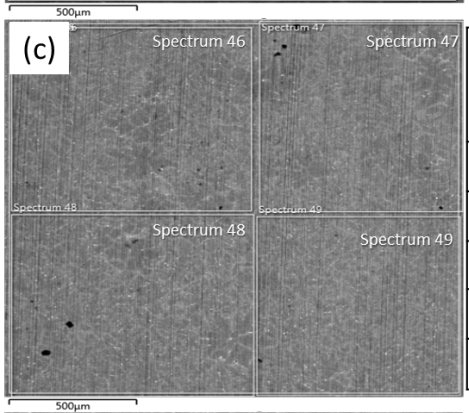

Element	Spectrum 45	Spectrum 46	Spectrum 47	Spectrum 48	Spectrum 49
	(weight %)				
C	15.3	16.2	15.2	14.9	14.4
O	3.0	3.4	3.1	2.6	2.8
Mg	79.9	78.8	79.9	80.6	81.0
Zn	1.8	1.6	1.8	1.9	1.8
Total	100.0	100.0	100.0	100.0	100.0

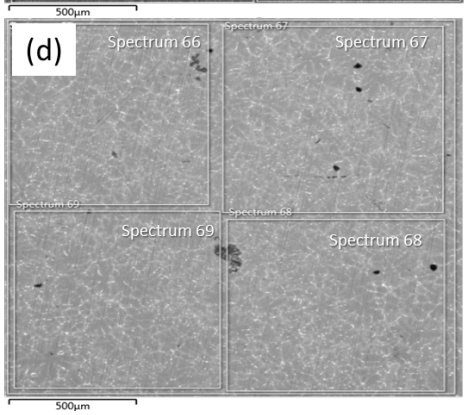

Element	Spectrum 65	Spectrum 66	Spectrum 67	Spectrum 68	Spectrum 69
	(weight %)				
C	6.9	6.4	7.6	7.5	6.6
O	2.1	2.0	2.2	2.3	2.0
Mg	86.0	86.5	85.1	84.9	86.3
Zn	5.0	5.1	5.1	5.3	5.1
Total	100.0	100.0	100.0	100.0	100.0

Figure 4.2 X-EDS quantification of elements present in as-cast (a) Z1; (b) Z1.5; (c) Z2; (d) Z5

4.2. Effect of Zn on the Grain Size and Hardness of As-cast Alloys

Table 4.1 provides the results of grain size and Vickers hardness measurements for all samples investigated. The high GRF of Zn is known to refine the grains with increasing addition of the alloying element [36]. As seen in Figure 4.3, the hardness and grain size of all samples was influenced by Zn concentration. In general, the increase in hardness coincided with increasing Zn concentration and decreasing average grain size of the alloys. However, it was recognized that other factors may have contributed to the hardness response of the alloys (e.g., porosity, solute strengthening, dispersion of oxides, etc.).

Table 4.1 Grain size values and hardness measurements of all samples

Material	Vickers Hardness (HV) *	Grain Size (μm) *
Ex Mg-CP	46.7 ± 6.3	103.64 ± 8.90
AC Mg-CP	37.2 ± 2.6	781.70 ± 113.14
Z1	51.5 ± 7.1	404.77 ± 52.38
Z1.5	51.6 ± 6.1	262.61 ± 24.87
Z2	54.4 ± 2.6	230.09 ± 22.50
Z5	58.5 ± 3.0	195.03 ± 16.74

** The errors are calculated from the 95% confidence interval.*

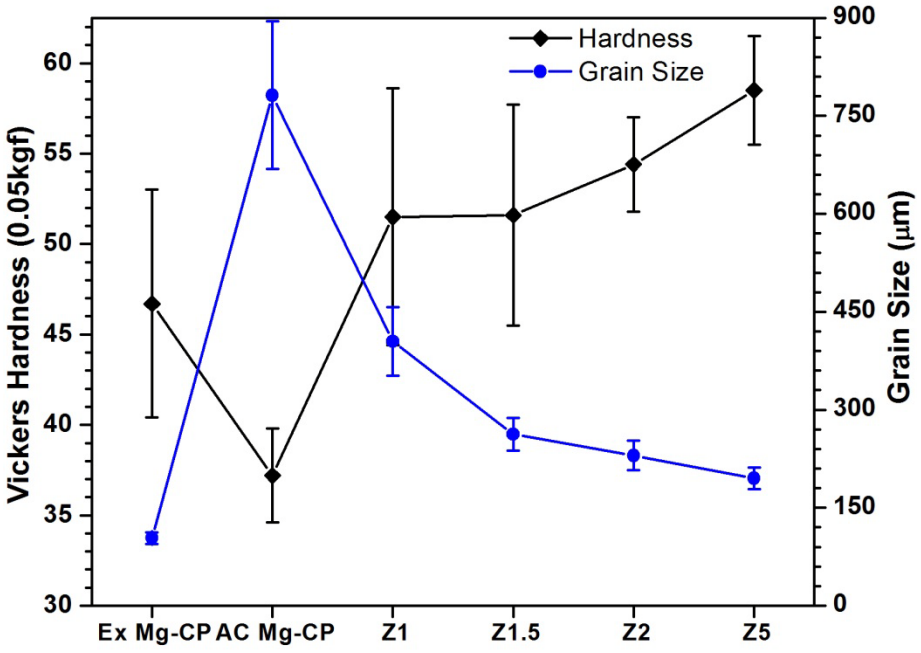

Figure 4.3 Hardness and grain size of all samples. The error bar represents 95% confidence interval

The increase in hardness was attributed to several mechanisms, namely; solid solution strengthening caused by Zn atoms [12, 61-63], Hall-Petch or grain boundary strengthening caused by the grain refining ability of Zn [36, 12, 59] and dispersion or second phase strengthening in alloys with higher Zn content [59]. The difference in hardness values of the extruded and as-cast pure Mg indicates that the finer grains (resulting from the plastic deformation of the alloy during extrusion) of the Ex Mg-CP resulted in a higher hardness due to Hall-Petch strengthening. However, with the addition of Zn, the hardness of the Z1 alloy increased irrespective of the presence of coarse grains, as compared to Ex Mg-CP. This indicates that the addition of Zn increased hardness by solid solution and second phase strengthening. It was noted that the addition of 1 wt. % Zn to the AC Mg-CP refined the grain size by ~50%, thus confirming the grain refining ability of Zn. With subsequent additions of Zn, the hardness was found to increase along with refinement of grains.

Although further mechanical tests were not conducted in this research, it can be predicted from the hardness results and available literature [36, 50, 60] that the Zn additions would likely also improve the tensile and yield strength of the alloys.

4.3. Microstructural Characterization and Chemical Analysis

4.3.1. As-cast Microstructure

Figure 4.4 shows the general microstructure of the alloys. The grains of the extruded pure Mg are seen clearly in Figure 4.4(a). The grains of the as-cast Mg were large enough to be seen with the naked eye, as shown in Figure 4.4(b). The AC Mg-CP specimen had columnar grains at the circumference of the disc and equiaxed grains near the center. This characteristic directional solidification suggests that grain growth first started at the mould wall and proceeded inwards.

Among the Zn containing alloys, both primary and secondary dendrites were seen in the optical micrographs and indicate that non-equilibrium solidification of the alloys occurred, leading to non-homogeneous distribution of alloying elements in the as-cast materials. The microstructure evolution during solidification is mainly dependent on the type of casting process, cooling rate of the melt, solute concentration, thermal gradient in the casting, and the velocity of the solid-liquid interface [44]. In alloys, heat generation and solute rejection at the

solid-liquid interface resulted in interface instability leading to formation of a perturbation which eventually led to the growth of dendrites [61]. Qualitatively, both primary and secondary dendrite arm spacings decreased with increasing Zn content in the alloys. This could be due to the refining ability of Zn causing finer dendrites.

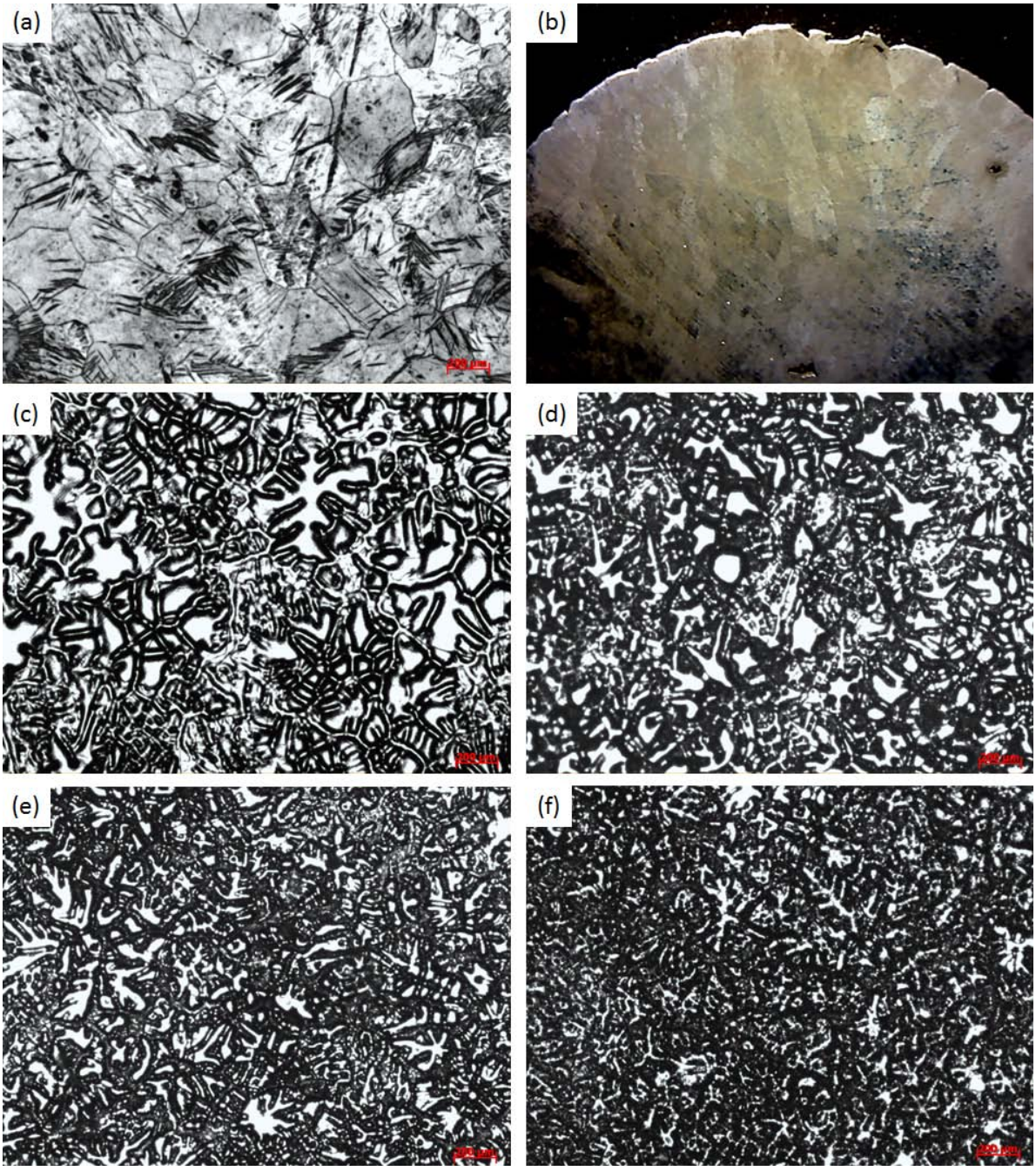

Figure 4.4 Optical micrographs of the (a) Ex Mg-CP; (b) AC Mg-CP; and as-cast (c) Z1; (d) Z1.5; (e) Z2; (f) Z5 alloys

Back Scattered Electron (BSE) mode in SEM revealed the compositional contrast in the microstructure of the as-cast alloys, as seen in Figure 4.5. The Ex Mg-CP (Figure 4.5(a)) contained twins [62, 63]. These twins were likely the result of the high plastic deformation experienced by the magnesium material during extrusion. In the Z1 alloy (Figure 4.5(a)), white precipitates were seen in the interdendritic regions. This could have occurred due to solidification of solute-rich liquid trapped between the dendrite arms, which would enable precipitation of Zn-rich particles [61]. In Figure 4.5(b), appearance of second phase developing along the dendrite boundaries was seen in the Z1.5 alloy. Similar morphology was also found in Mg alloys with ≥ 5 wt.% Zn content in a study conducted by Cai *et al.* [64] in the form of white islands. The amount of the second phases increased with increasing addition of Zn, as seen by comparing the Z2 and Z5 alloys (see Figure 4.5(c), (d)). In the Z2 alloy, the second phases began to form network-like connections, which were also reported in the literature [64]. However, with further increase in Zn content these network structures seemed to break down, as seen in Figure 4.5(d). The presence of these network structures may have an effect on the mechanical and corrosion properties of the material [64] as these second phases may act as dispersion strengthening sites [59] and as micro-electrodes during corrosion, effectively creating a microgalvanic cell [65]. As the second phases in general are nobler than pure Mg [12], the corrosion rate might be significantly affected by these second phases.

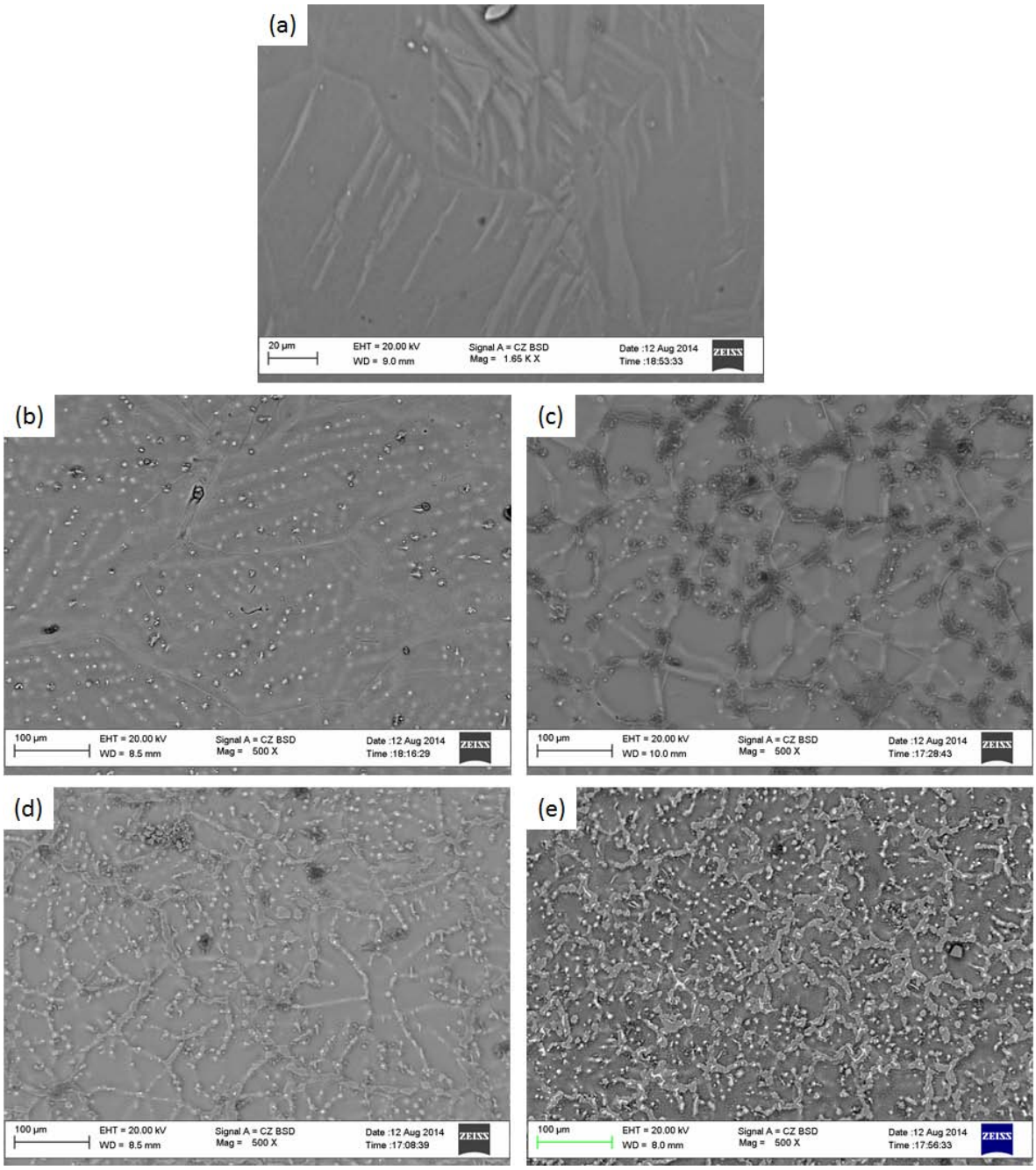

Figure 4.5 SEM images of the (a) Ex Mg-CP and as-cast (b) Z1; (c) Z1.5; (d) Z2; (e) Z5 alloys

From the chemical analysis done through X-EDS, Mg and O were found in pure Mg (extruded and as-cast) and oxide inclusions were found to be present in all of the alloys. Formation of oxide inclusions was likely the result of the turbulent liquid metal oxidizing during casting pouring. Presence of oxide films and inclusions is detrimental for the mechanical properties of the alloys, since these undesirable constituents act as stress concentrations during mechanical loading. However, the presence of the second phases along

the grain boundaries reveals a relatively uniform distribution. From the X-EDS data for all alloys, given in Figure 4.6, the matrix contained dissolved Zn. The white nodules seen in the alloys have a higher content of Zn as compared to the matrix. Thus, the nodules likely formed once the maximum solid solubility of Zn in the Mg matrix was attained. For equilibrium conditions the maximum solid solubility of Zn in Mg is 6.2 wt. %. It was observed that at the room temperature, the solid solubility limit of Zn in Mg is ~2 wt. %. Therefore, for the Z1 and Z1.5 alloys, the Zn would be dissolved in the matrix. In case of the Z2 and Z5 alloys, formation of Mg_xZn_y phases would be expected. Due to the rapid solidification of the alloy, Zn-enriched liquid in the interdendritic regions enabled formation of the Mg_xZn_y particles.

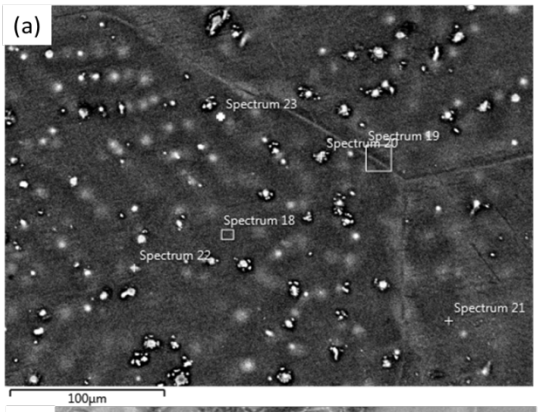

Element	Matrix	Particles	
	Spectrum 18	Spectrum 22	Spectrum 23
	(weight %)		
O	2.4	12.8	5.2
Mg	96.8	80.4	88.8
Zn	0.8	6.8	6.0
Total	100.0	100.0	100.0

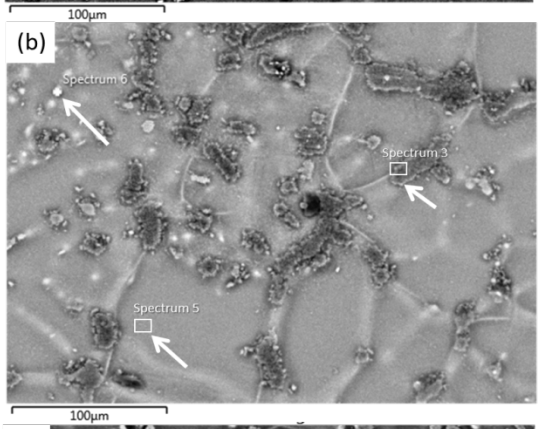

Element	Matrix	2nd phase	Particle
	Spectrum 5	Spectrum 3	Spectrum 6
	(weight %)		
O	3.2	13.8	7.6
Mg	96.8	79.4	74.9
Zn	0	6.8	17.5
Total	100.0	100.0	100.0

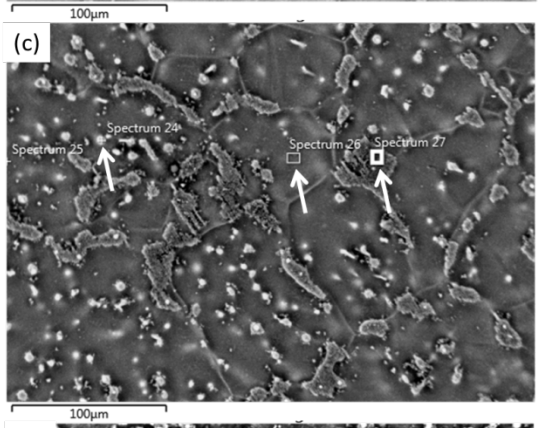

Element	Matrix	2nd phase	Particle
	Spectrum 26	Spectrum 27	Spectrum 24
	(weight %)		
O	3.6	7.6	7.1
Mg	94.2	74.9	64.7
Zn	2.2	17.5	28.2
Total	100.0	100.0	100.0

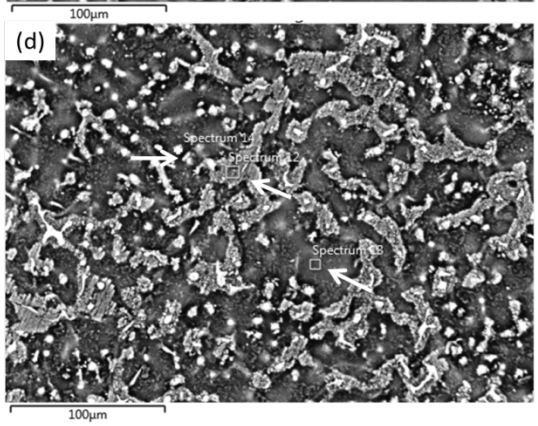

Element	Matrix	2nd phase	Particle
	Spectrum 13	Spectrum 12	Spectrum 14
	(weight %)		
O	5.9	15.4	18.4
Mg	91.3	72.2	32.6
Zn	2.8	12.4	49.0
Total	100.0	100.0	100.0

Figure 4.6 SEM images of the as-cast (a) Z1; (b) Z1.5; (c) Z2; (d) Z5 alloys showing the spectra chosen for X-EDS analysis (indicated by arrows). The adjoining tables show an estimate of the various elements present.

4.3.2. X-Ray Diffraction Studies

The XRD plots of the as-cast alloys are provided in Figure 4.7. The $MgZn_2$ phase was seen only in the XRD pattern of the Z5 alloy, although there is evidence of second phases in the other alloys from the SEM and X-EDS results. This is probably due to the low volume fraction of the second phases in the Z1.5 and Z2 alloys, which could be below the detection limit of the XRD machine. Absence of second phases in the XRD peaks of magnesium-zinc alloys with zinc additions ≤ 5 wt. % was seen in other studies as well [50, 64, 46].

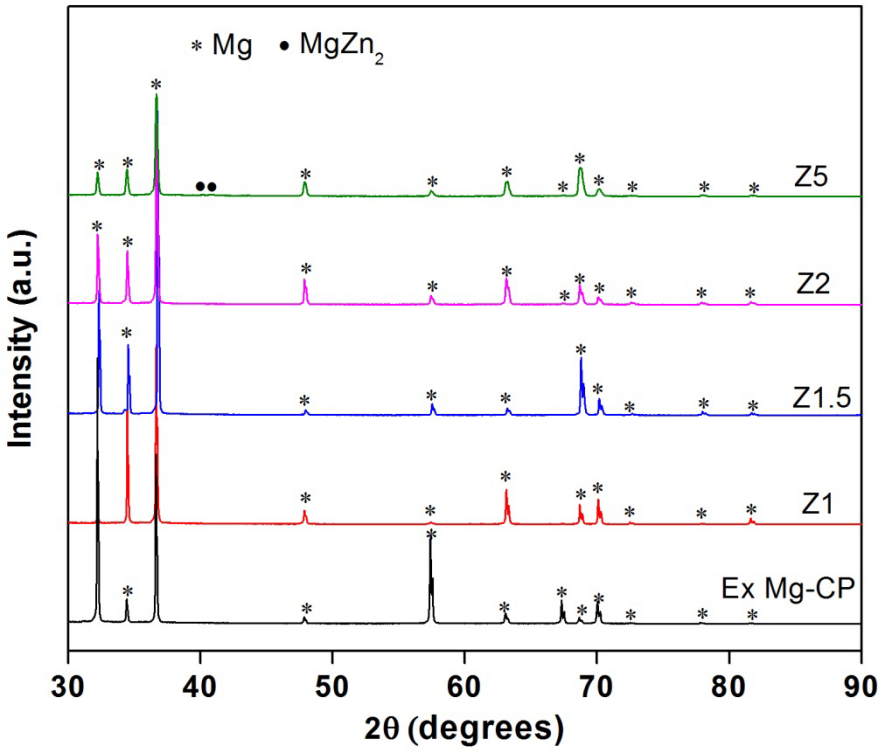

Figure 4.7 XRD patterns of alloys before corrosion

The low volume fraction of second phases and their absence from the XRD plot can be explained by referring to the binary phase diagram in Figure 2.1. In the Z1, Z1.5 and Z2 alloys, Zn is mostly incorporated into the α(Mg) matrix and only a small fraction is evolving as a second phase, thus resulting in low volume fraction [50, 64]. However, when 5 wt. % of Zn is added, the solid solubility limit at room temperature is exceeded resulting in the evolution of large volume fraction of second phases. The $MgZn_2$ phase is an intermediate solid solution of the Mg-Zn system. During the solidification process, the $Mg_{51}Zn_{20}$ eutectic product decomposes at 325°C into α(Mg) and MgZn. The MgZn being metastable in nature,

subsequently transforms into the stable $MgZn_2$ phase, which was detected in the XRD spectra.

4.4. Immersion Corrosion Tests

4.4.1. Corrosion Surface Morphology

Figure 4.8 shows the immersion samples of all four alloys after exposure to SBF for 10 days. The extruded Mg sample (Figure 4.8(a)) does not show severely corroded regions as seen in the Zn containing alloys. This is probably due to its single phase microstructure leading to localized corrosion where the irregular pits are formed and the corrosion front proceeds laterally instead of forming deep pits [65]. In the case of the Zn alloys, non-uniform corrosion was observed indicating that there was preferential corrosion occurring. A black corroded area on the surfaces of Z1, Z1.5 and Z2 alloys (Figure 4.8(b), (c), (d)) was observed. In the case of the Z5 alloy, the black corroded area covered almost the entire surface of the sample. A similar surface appearance was found in a study conducted in 2012 [46].

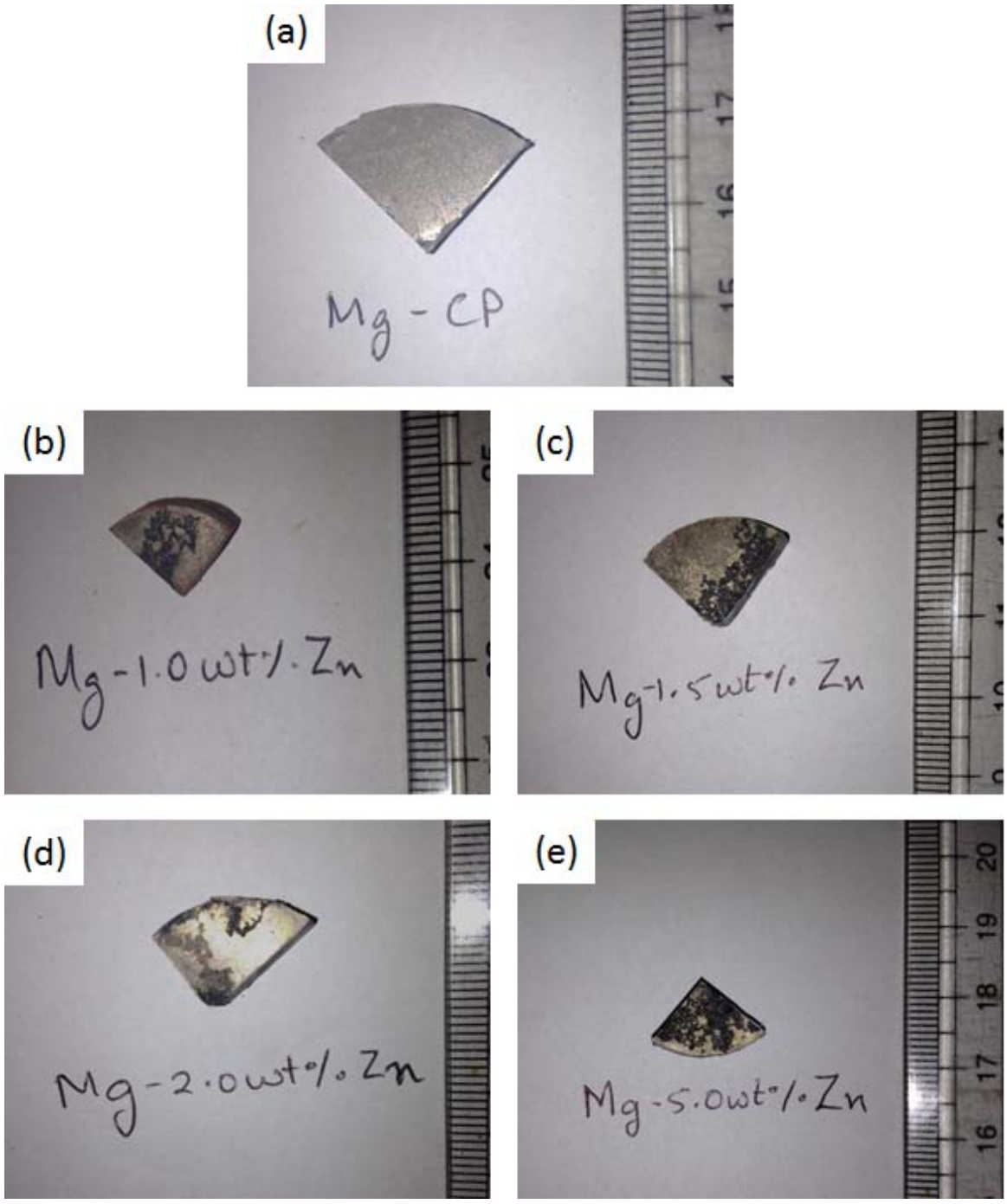

Figure 4.8 Corroded surfaces of (a) Ex Mg-CP; (b) Z1; (c) Z1.5; (d) Z2; (e) Z5 samples after immersion for 10 days in SBF

Closer examination of the corroded surface revealed pitting corrosion in the alloys on the micro-scale with the aid of SEM in the secondary electron (SE) mode, as shown in Figure 4.9. The extruded Mg sample in Figure 4.9(a) exhibited irregular pits (indicated by arrows). These pits might have been formed due to particle undermining as different corrosion fronts

proceeded laterally on the surface of the sample. However, in the Zn containing alloys, non-uniform corrosion was observed, as some regions of the samples remained intact. In Figure 4.9(b), non-corroded network like connections were observed (shown by the arrow) indicating that some preferential corrosion occurred. This could suggest that the second phases acted as a passive electrode, while the Mg-rich matrix was the active electrode during corrosion. Therefore, the network-like layered structure appearing in the Z5 alloy (Figure 4.8(d)) could enhance the corrosion rate.

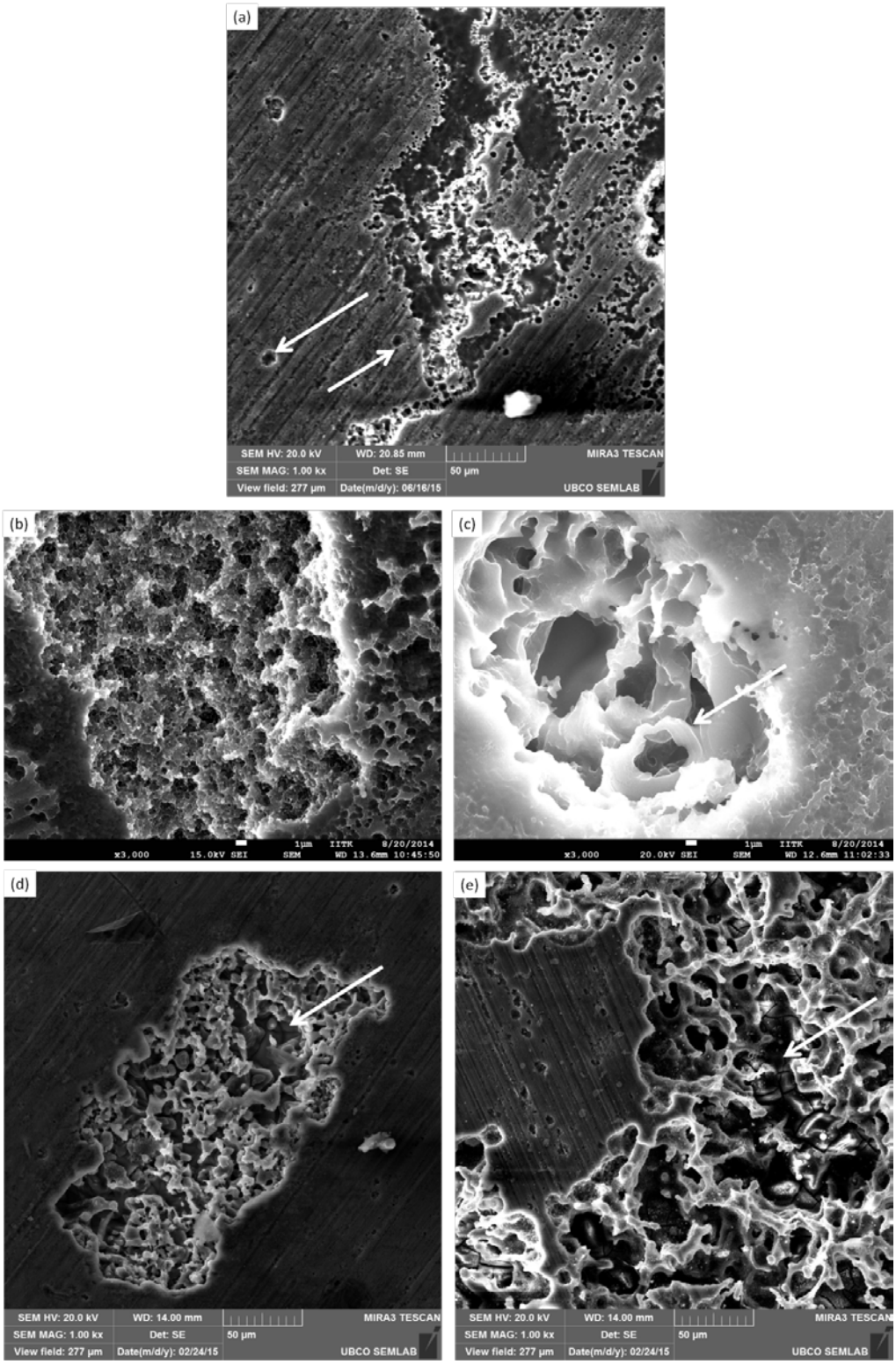

Figure 4.9 SEM images of corroded surfaces of (a) Ex Mg-CP* and as-cast (b) Z1; (c) Z1.5[#]; (d) Z2[#]; (e) Z5[#] alloys after immersion for 10 days in SBF
***arrow indicates irregular pits; [#]arrow indicates network-like connections**

4.4.2. Effect of Increasing Zinc Content on the Corrosion Rate

As can be seen from Figure 4.10, the immersion corrosion rates of the alloys, calculated from the weight loss measurements using Equation 3.1, varied with the addition and increase in Zn concentration. In the as-cast samples, with the addition of Zn, the corrosion rate dropped by more than 50%, proving that Zn substantially improved the corrosion resistance of Mg. Among the Z1, Z1.5 and Z2 alloys, the Z1 alloy exhibited the highest corrosion rate, while with the appearance of second phases in the remaining alloys (as seen in Figure 4.5), the corrosion resistance improved. In the Z1.5 alloy, the $MgZn_2$ second phase could be acting as a physical barrier to the α(Mg) matrix, thus preventing its continuous corrosion. Such behaviour was seen previously in other studies as well [65, 51]. In the case of the Z2 alloy, the $MgZn_2$ phase formed network-like connections (as seen in Figure 4.5(c)), thus further isolating the matrix and reducing the corrosion rate. However, further increase in Zn content resulted in the fragmentation of the $MgZn_2$ networks into small islands thus creating many microgalvanic cells. These cells consisted of micro-cathodic ($MgZn_2$) and micro-anodic (α(Mg)) sites, thus enhancing the corrosion rate of the Z5 alloy.

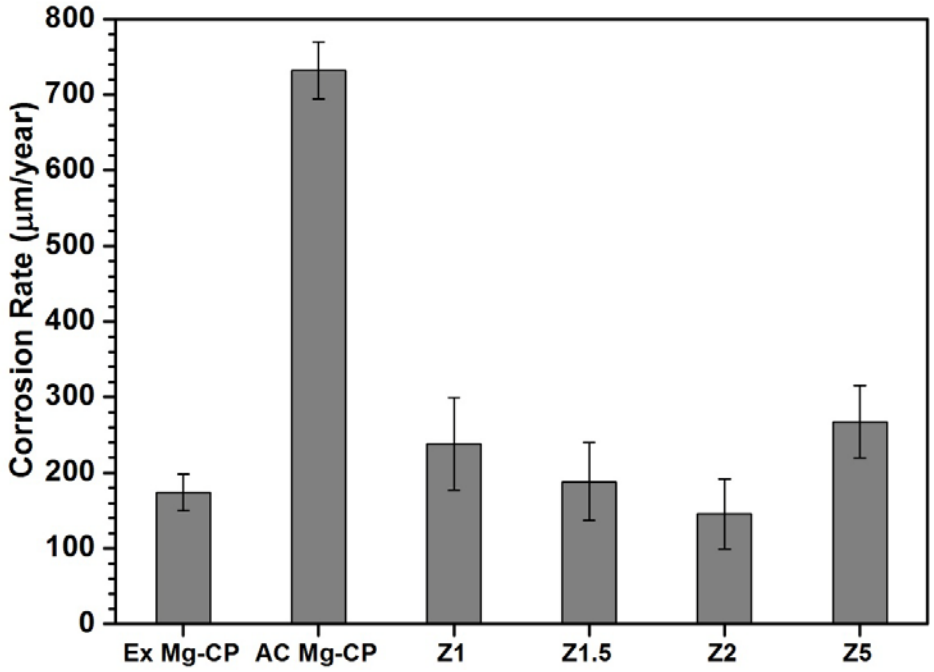

Figure 4.10 Corrosion rates of the samples after immersion for 10 days in SBF. All corrosion rates were averaged for three specimens of the same sample. The error bars represent the standard deviation.

The extremely low corrosion rate of the Ex Mg-CP, in comparison to AC Mg-CP can be accounted for by its small and homogenous grain size (see Table 4.1). The reduction in grain size by ~86% in the extruded Mg as compared to the as-cast Mg resulted in more uniform and homogenous corrosion, as seen in Figure 4.8(a) [12]. It was reported that the refinement in grain size significantly reduced the corrosion rates in a material, probably due to the high grain boundary and dislocation densities [16]. However the underlying principle relevant to the present study remains unclear.

4.4.3. Corrosion Product Characterization

4.4.3.1. SEM and X-EDS

Performing X-EDS on the corroded surface of all four alloys revealed the presence of Mg, O and Zn, as shown in Figure 4.11. Some C was detected on the surface due to contamination from the SEM instrument. In Figure 4.11(e), the EDS map for Zn traces the network-like interdendritic regions. This could possibly be a $MgZn_2$ phase which acts as the cathode, facilitating the corrosion of the matrix (anode) surrounding it. These networks could have formed in all the alloys, but were more obvious in the Z5 alloy, where $MgZn_2$ had the highest volume fraction.

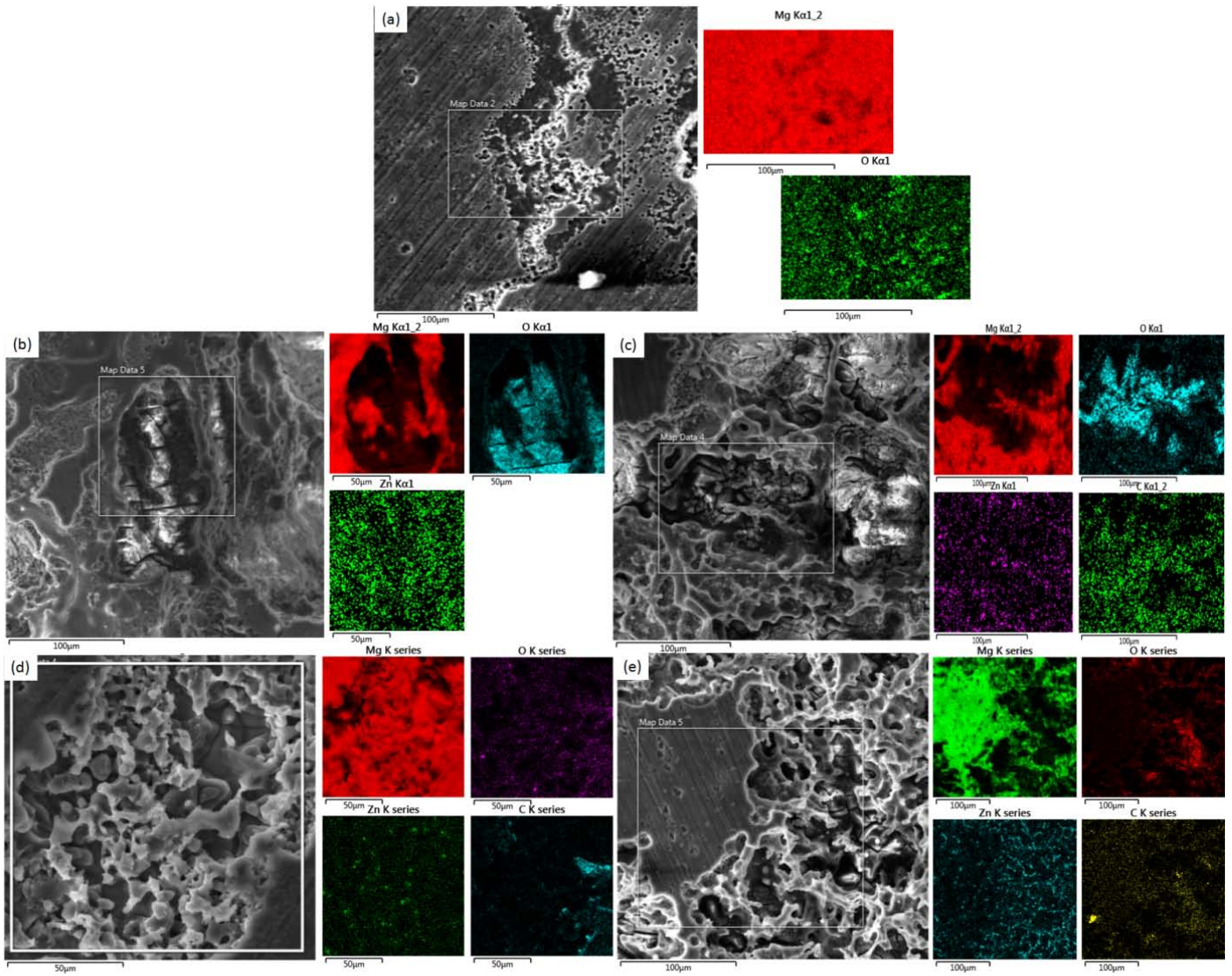

Figure 4.11 SEM images of corroded (a) Ex Mg-CP; (b) Z1; (c) Z1.5; (d) Z2; (e) Z5 samples after immersion for 10 days in SBF after immersion for 10 days in SBF showing the area mapped X-EDS spectra

4.4.3.2. Fourier Transform Infrared Spectroscopy

The FTIR conducted on the filtered corrosion products from the SBF after 10 days of immersion resulted in the transmission peaks, as shown in Figure 4.12. Comparing the peaks with available literature, the functional groups listed in Table 4.2 were identified. The results suggest that carbonates, phosphates and hydroxides were found in the filtrate. This may suggest the formation and subsequent dissolution of a protective film composed of magnesium carbonates, magnesium hydroxides and some form of phosphates.

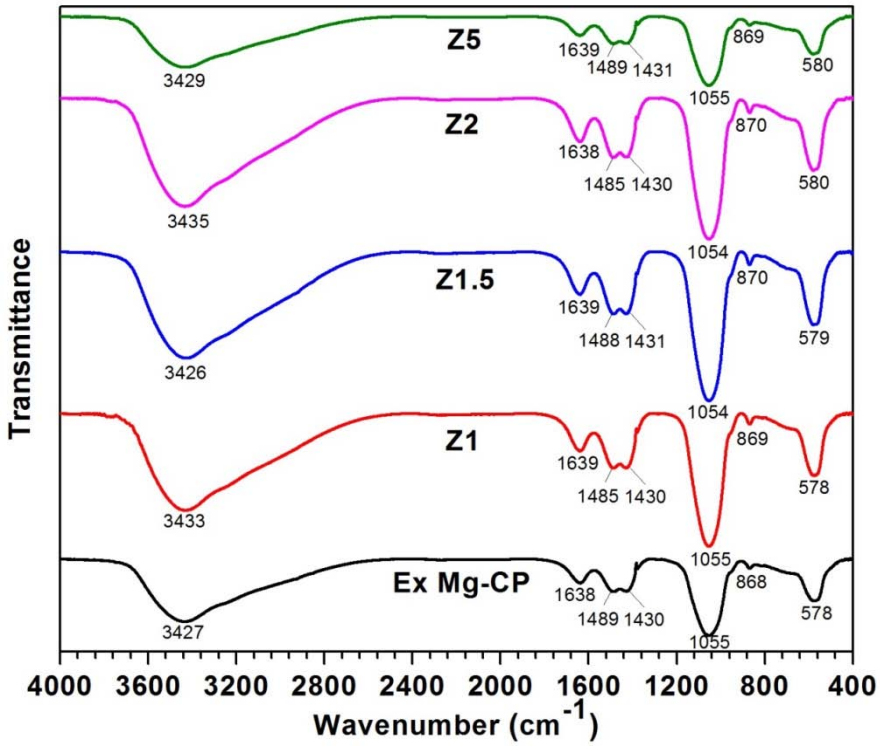

Figure 4.12 FTIR spectrum of the filtrate obtained after immersion tests for all as-cast alloys

Table 4.2 Functional groups corresponding to FTIR Spectroscopy peaks

Wavenumber (cm^{-1})	Functional group [Reference]
3700-2500	-OH [66, 67, 68]
1638,1639	-OH [66, 67, 68, 69, 70]
~1490,1430	$-CO_3^{-2}$ [67, 68, 69, 70, 71]
1054,1055	$-PO_4^{-3}$ [68, 69]
868-870	$-CO_3^{-2}$ [67, 68, 69, 70, 71]
578-580	$-PO_4^{-3}$ [68, 69]

A similar FTIR spectrum was observed by Zhu *et al.* [68] in an AZ31 alloy where one of the corrosion products was deemed to be amorphous calcium apatite precursor (ACAP). It was also postulated that ACAP can be converted to calcium apatite, which along with Mg ions released during degradation might aid in the healing of the fractured bone [72].

4.4.3.3. XRD Results

After the immersion tests, one specimen from each alloy was used to conduct an XRD test in an attempt to identify the corrosion products on the surface of the alloys. However, it was noted that most of the corrosion products were found at the bottom of the flask at the end of the immersion test. Therefore, Z1.5 alloy did not show the presence of any corrosion products as seen in Figure 4.13. The other alloys showed presence of magnesium hydroxide, calcium phosphates, and magnesium carbonates, thus confirming the FTIR results. The minimal presence of corrosion products on the surface of the alloys indicates that a protective passive film was formed on the alloys during the immersion period. However, due to the weak adhesion of the film, the strong electrolyte ions from the SBF penetrated the film to the matrix, disintegrating it in the process.

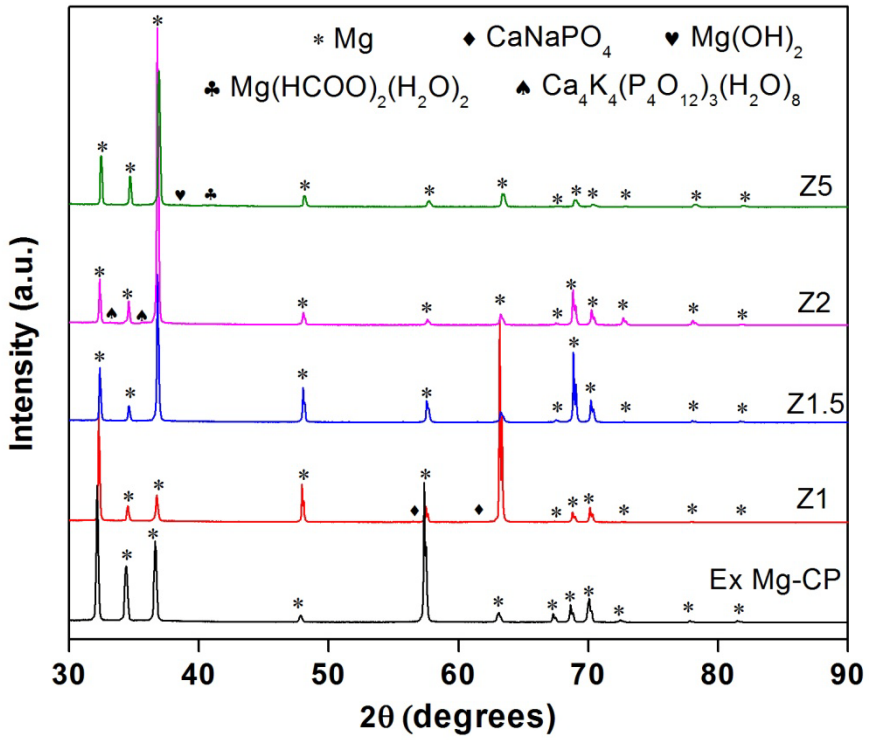

Figure 4.13 XRD patterns of alloys after corrosion

Though the XRD data suggests the presence of some complex phosphates as seen in Figure 4.13, it was noted that the Ca^{2+} cation may be substituted by other metal cations (K^{+}, Na^{+}, Mg^{2+}, Zn^{2+}) present in the SBF [68]. Thus, part of the Ca^{2+} in the apatite may be substituted by the above mentioned metallic cations.

4.5. Electrochemical Behaviour

The Tafel polarization and EIS experiments were conducted after immersion of all the samples in freely aerated SBF at room temperature for one hour to obtain the stable Open Circuit Potential (OCP), as explained in section 3.4.4.1.

The OCP vs. time plots for the two pure Mg samples and all four alloys is shown in Figure 4.14. The stable OCP at the end of the one hour immersion time varied widely for all samples. The Ex Mg-CP exhibited a gradually increasing variation in OCP from -0.99V to -0.67V. The relatively positive OCP value at the end of the stabilization time may indicate towards the gradual formation of a protective film making the sample more passive. In stark contrast, the AC Mg-CP sample however has a much lower OCP value (-1.55V) at the

beginning of immersion and stabilized at -1.53V, which is close to the expected value for pure Mg (-1.7V) [65]. On closer inspection it can be seen that there was a gradual increase in OCP at the beginning of the immersion period and then a drop at ~400s, followed by a slight increase for the remainder of the test. A sudden drop in corrosion potential has been associated with localized passivation film breakdown [73]. The gradual increase in OCP could indicate to the formation of a passive layer of $Mg(OH)_2$. The film integrity is maintained by the release of hydroxyl (OH^-) ions during the reduction of water (Equation 2.1(b)), increasing the pH locally [65]. However, due to the presence of the chloride containing corrosive electrolyte and the low pH (<10), the passive film breaks down at ~400s leading to the drop in OCP. The difference in OCP values between extruded Mg and as-cast samples indicates to the significant improvement in the corrosion potential with refinement and homogeneity of grain size as was exhibited previously by the immersion corrosion results in section 4.4.2.

As seen in Figure 4.14, among the as-cast samples, the alloys had considerably higher OCP values in comparison to AC Mg-CP, which confirms that Zn acts as a passivating element by pushing the OCP towards more noble values. The Z1 and Z2 alloys show high and similar OCP values. The decreasing potential values of the Z1.5 alloy with time indicate the shift in OCP towards the active direction, making it more susceptible to corrosion. The potential of the Z5 alloy also decreased slightly and then stabilized, yielding the lowest OCP among the alloys. It was noted that due to inhomogeneity in the as-cast samples, there was deviation in OCP values between the different repeats. The average OCP values for the different repeats are shown in Table 4.3, along with the average corrosion potentials (E_{corr}), average corrosion current densities (i_{corr}) and the average corrosion rates.

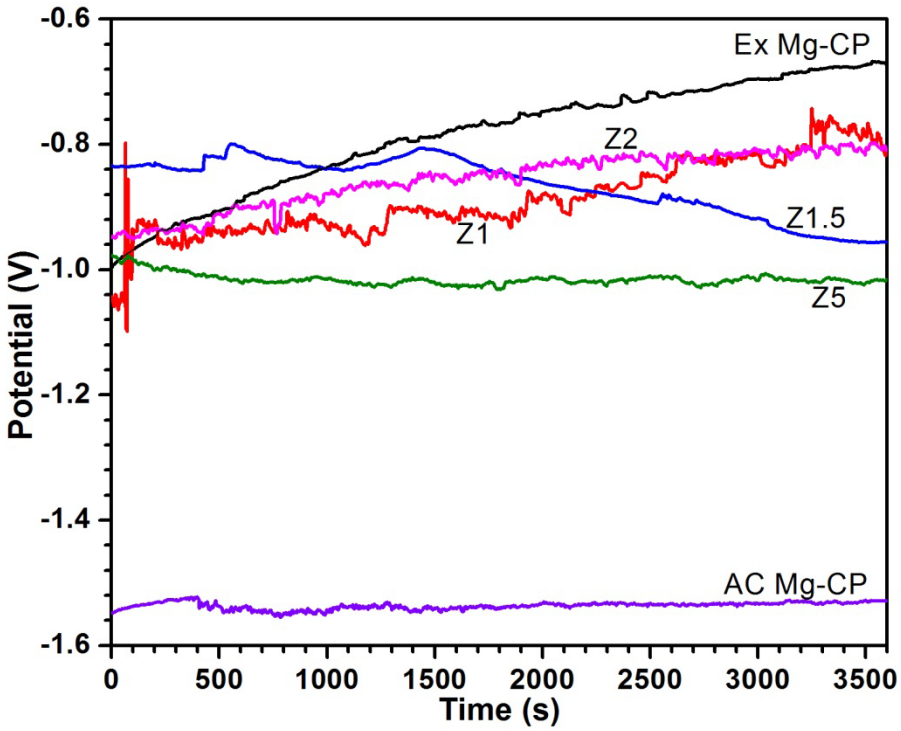

Figure 4.14 OCP vs. time plots for all samples

Table 4.3 Corrosion parameters for all samples derived from OCP and Tafel plots

Material	OCP (V vs. SCE) *	E_{corr} (V) *	i_{corr} (µA/cm^2) *	Corrosion Rate (µm/year) *
Ex Mg-CP	-0.705 ± 0.052	-0.681 ± 0.031	.058 ± 0.065	1.33 ± 0.74
AC Mg-CP	-1.535 ± 0.005	-1.505 ± 0.058	8.617 ± 3.020	197.11 ± 34.54
Z1	-0.808 ± 0.021	-0.753 ± 0.048	.003 ± 0.002	0.07 ± 0.03
Z1.5	-0.799 ± 0.081	-0.847 ± 0.087	.072 ± 0.072	1.63 ± 0.81
Z2	-0.803 ± 0.067	-0.788 ± 0.053	.017 ± 0.026	0.37 ± 0.29
Z5	-1.074 ± 0.233	-1.101 ± 0.202	0.051 ± 0.066	1.15 ± 0.75

** Average values from the three runs. The error is given in terms of the standard deviation*

4.5.1. Tafel Polarization

The Tafel plots obtained between a potential range of -250mV to +250mV of the OCP for all the samples are shown in Figure 4.15. The intersection points of the extrapolated anodic and cathodic curves were used to determine the corrosion potentials (E_{corr}) and corrosion current

densities (i_{corr}), whose values are given in Table 4.3. The graphs for the remaining repeats can be found in Appendix A.

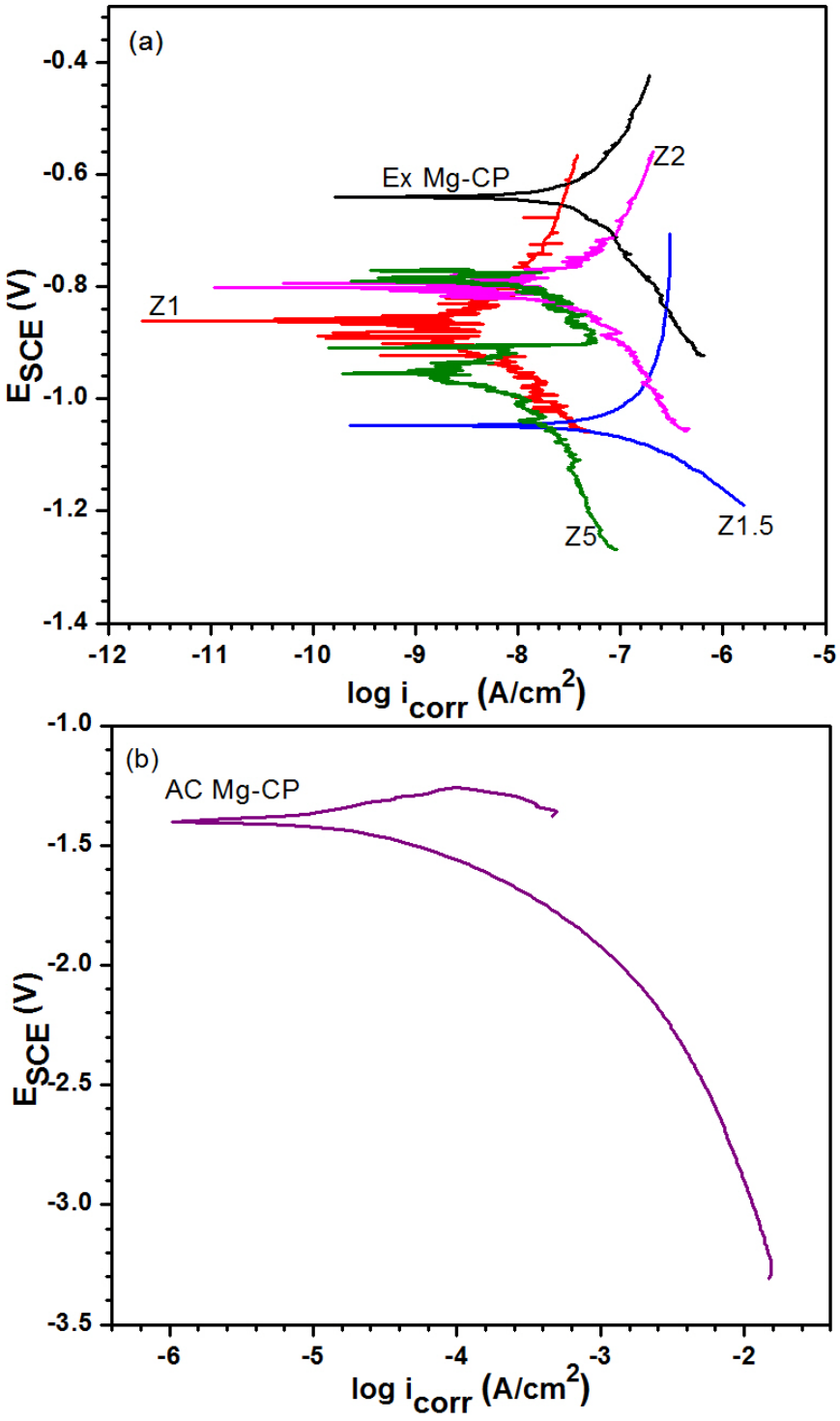

Figure 4.15 Tafel plots for (a) Ex Mg-CP and as-cast alloys; (b) AC Mg-CP

The corrosion rates calculated from the i_{corr} values using Equation 3.2, are given in Table 4.3 and graphically represented in Figure 4.16. As expected, the AC Mg-CP has the highest i_{corr} value and corrosion rates. The Tafel plot of the AC Mg-CP can be explained by the Negative Difference Effect (NDE) model proposed by Song and Atrens [65]. The linearity of the cathodic branch corresponds to hydrogen evolution and $Mg(OH)_2$ film formation (Equation 2.1) [65]. During the anodic cycle, with increasing applied potential, breakdown of the passive film occurs at the pitting potential (~1.322V in this case) creating a film-free area, resulting in an increase in the hydrogen evolution and Mg dissolution thus accelerating the current density [65], as seen in Figure 4.15(b). This indicates that the corrosion rate of AC Mg-CP is primarily dictated by the cathodic reaction rate. The dependence of corrosion of Mg and its alloys on the cathodic reaction rates in polarization tests as a result of Negative Difference Effect (NDE) was suggested by Ha *et al.* [73].

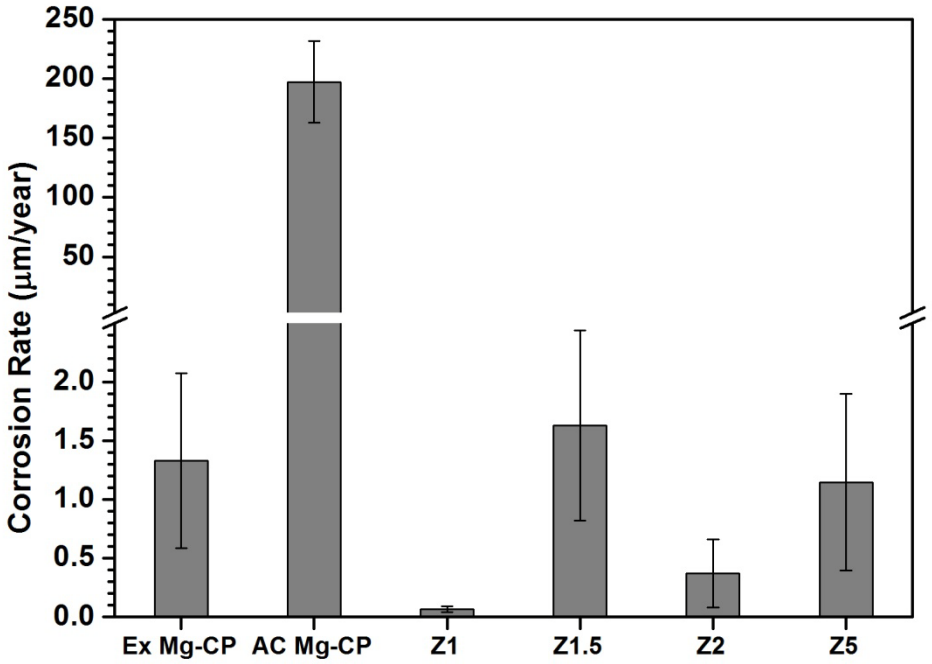

Figure 4.16 Corrosion rates of the samples from Tafel polarization. All corrosion rates were averaged for three specimens of the same sample. The error bar represents standard deviation.

The considerable improvement in the corrosion rate of Ex Mg-CP over AC Mg-CP can be explained by the ~86% reduction in grain size as explained before in section 4.4.2. From Table 4.3, it can be seen that the Z1 alloy has the most positive E_{corr} and least i_{corr} value, which directly translates into the lowest corrosion rate among all the samples. The decreased corrosion rate of all as-cast alloys in comparison to AC Mg-CP proves the ability of Zn as a

corrosion inhibitor, as seen previously in the immersion corrosion results. The Z1.5 alloy has a higher corrosion rate than Z1 and a slightly higher corrosion rate (0.30µm/year) than the Ex Mg-CP. This can be explained by the more negative corrosion potential (E_{corr}) of Z1.5 as seen in Figure 4.15 in comparison to all other samples except AC Mg-CP. The serrations observed in the Tafel plots in Figure 4.15(a) in the Z1, Z2 and Z5 alloys indicate that there could be constant formation and dissolution of passive film on the sample surface thus providing some level of protection from corrosion. The lack of these serrations in the plot for Z1.5 alloy could mean that there was no passive layer formed on the alloy surface thus resulting in direct exposure to SBF resulting in its higher corrosion rate.

The Z2 alloy shows higher E_{corr} and i_{corr} values in comparison to Z1 alloy (Figure 4.15(a)). This can be explained by the tendency of Z2 alloy to form larger quantity of $Zn(OH)_2$ than the Z1 alloy due to the presence of more Zn^{2+} ions in Z2 [73]. The $Zn(OH)_2$ decomposes into ZnO, which enhances the protectiveness of the passive film. However, the protective nature of ZnO is found to be masked by its higher conductivity in comparison to $Zn(OH)_2$, resulting in more hydrogen gas evolution thus elevating the E_{corr} [73]. The higher conductivity of ZnO combined with the constant breakdown of the passive film, as seen from the serrations in Figure 4.15(a), contribute to the higher corrosion current density resulting in a higher corrosion rate of the Z2 alloy in comparison to Z1 alloy. The higher average corrosion rate of Z5 alloy (Figure 4.16) in comparison to Z1 and Z2 can be attributed to the fragmented networks of $MgZn_2$ as seen in Figure 4.5(e). However, in Figure 4.15(a), the Z5 alloy exhibits passivation behaviour which reduces its i_{corr} value (Table 4.4). The passivation starts at the constant passivation current (i_{pass}) for a certain range forming a layer composed of magnesium and zinc hydroxides, which eventually breaks down at -0.803V (E_b) leading to corrosion of the material.

Table 4.4 Passivation parameters for Z5 alloy

Material	**E_{corr} (V)**	**i_{pass} (µA/cm^2) Passivation Current**	**E_b (V) Breakdown Voltage**	**Passive Range (V)**	**i_{corr} (µA/cm^2)**
Z5	-0.959	0.054	-0.803	0.093	0.004

The analysis of the OCP and Tafel plots revealed that there was no particular trend followed by the alloys (with increasing Zn content) as seen previously in the immersion corrosion results. This was probably due to the localized corrosion occurring after passive film breakdown, as suggested by Ha *et al.* [73]. Variation in corrosion parameters between different repeats was also noted and probably arose due to the inhomogeneous nature of the as-cast samples.

4.5.2. Electrochemical Impedance Spectroscopy Tests

Electrochemical Impedance Spectroscopy (EIS) was used to model the electrode-electrolyte interface. All impedance experiments were conducted at the stabilized OCP for the respective samples. Curve fitting of the impedance data and analysis of the EIS plots (Figure 4.17, Figure 4.18) generated the appropriate electrical circuit shown in Figure 4.19.

The Nyquist plots for all the samples in Figure 4.17 consist of an arc with one end extending away from the incomplete semicircle, with the exception of AC Mg-CP. The single incomplete semicircles in the Nyquist plots reveal that they consist of a single time constant (i.e., one RC component) [74]. The loop at the low frequency end of the plot in Figure 4.17(b) could be attributed to inductive behaviour of the system [75]. The diameters of the semicircles (when drawn) correspond to the polarization or charge transfer resistance of the electrochemical system [74]. This resistance is inversely related to the corrosion current density (i_{corr}) by the Stern-Geary equation [53]:

$$i_{corr} = \frac{\beta_a \beta_c}{2.303(\beta_a + \beta_c)} . \frac{1}{R_p} \quad (4.1)$$

where, the *'i_{corr}'* was the corrosion current density in A/cm^2, *'β_a'* and *'β_c'* were the anodic and cathodic Tafel slopes in V/decade, respectively and *'R_p'* was the polarization/charge transfer resistance in Ω.cm^2. Thus, visually it was seen from Figure 4.17, that the Z1 alloy would have the highest diameter i.e., the highest resistance to corrosion. According to Equation 4.1, the Z1 alloy would have the least i_{corr}, thus resulting in the lowest corrosion rates as previously seen in Table 4.3 and Figure 4.16. In contrast to the Z1 alloy, the AC Mg-CP had the smallest diameter and hence the least resistance to corrosion, thus exhibiting the highest corrosion rate in the Tafel plots.

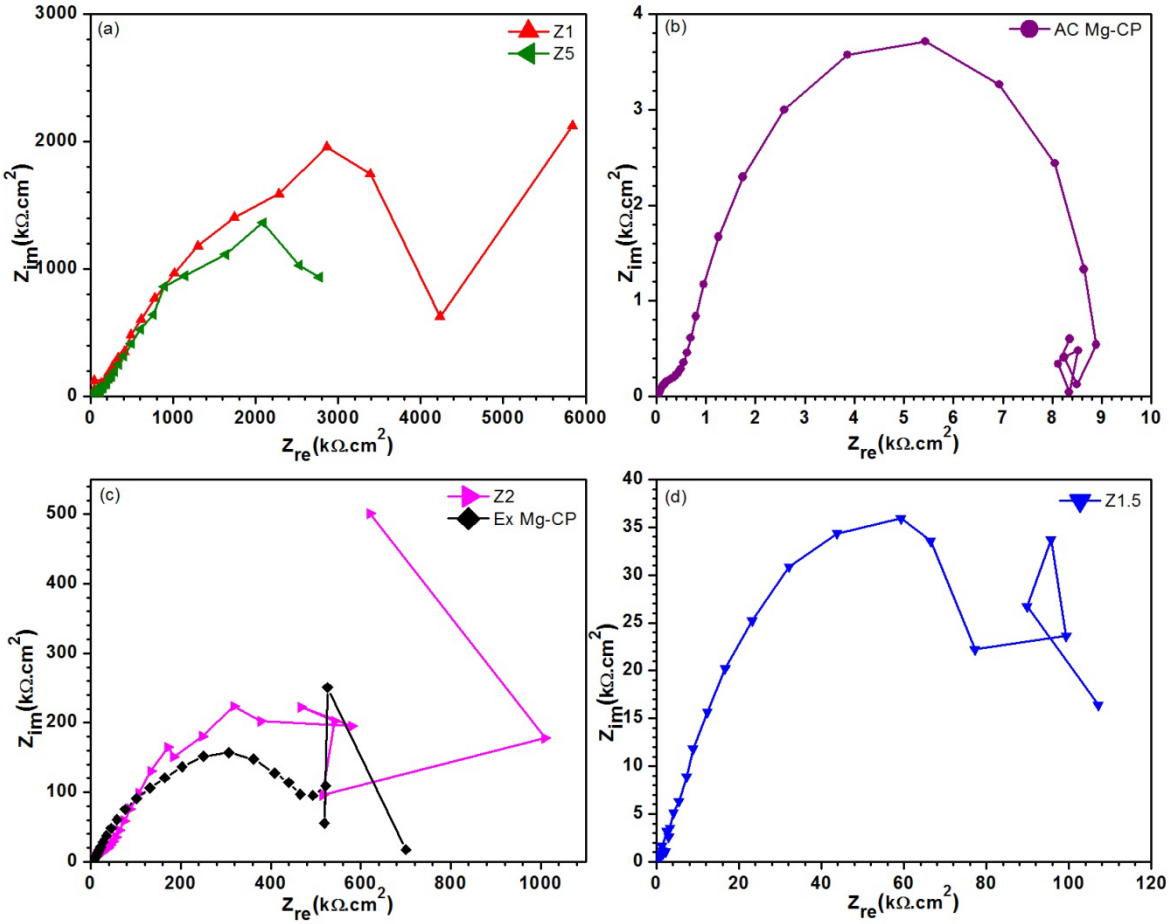

Figure 4.17 Nyquist plots for (a) Z1 and Z5; (b) AC Mg-CP; (c) Z2 and Ex Mg-CP; (d) Z1.5 samples

The use of Bode plot indicates the effect of a capacitor as it is directly related to the frequency at which the AC signal is applied [75]. The Bode magnitude and phase plots are shown in Figure 4.18. The Mg-CP samples (extruded and as-cast) exhibit constant impedance in the low frequency region in the Bode magnitude plot (Figure 4.18(a)) indicating the presence of some resistance, as the interfacial capacitor behaves as an open circuit [27]. These constant impedance values indicate to the presence of some protective layer, possibly $Mg(OH)_2$ [22]. The negative slope of the Bode magnitude plots seen in all the samples corresponds to the capacitive behavior of the electrical double layer present between the metal and the electrolyte [27, 22, 75]. It was observed that the Mg-Zn alloys did not exhibit a substantial region with constant impedance indicating that a passive layer was not formed immediately probably due to the passive nature of the alloys relative to the pure Mg samples.

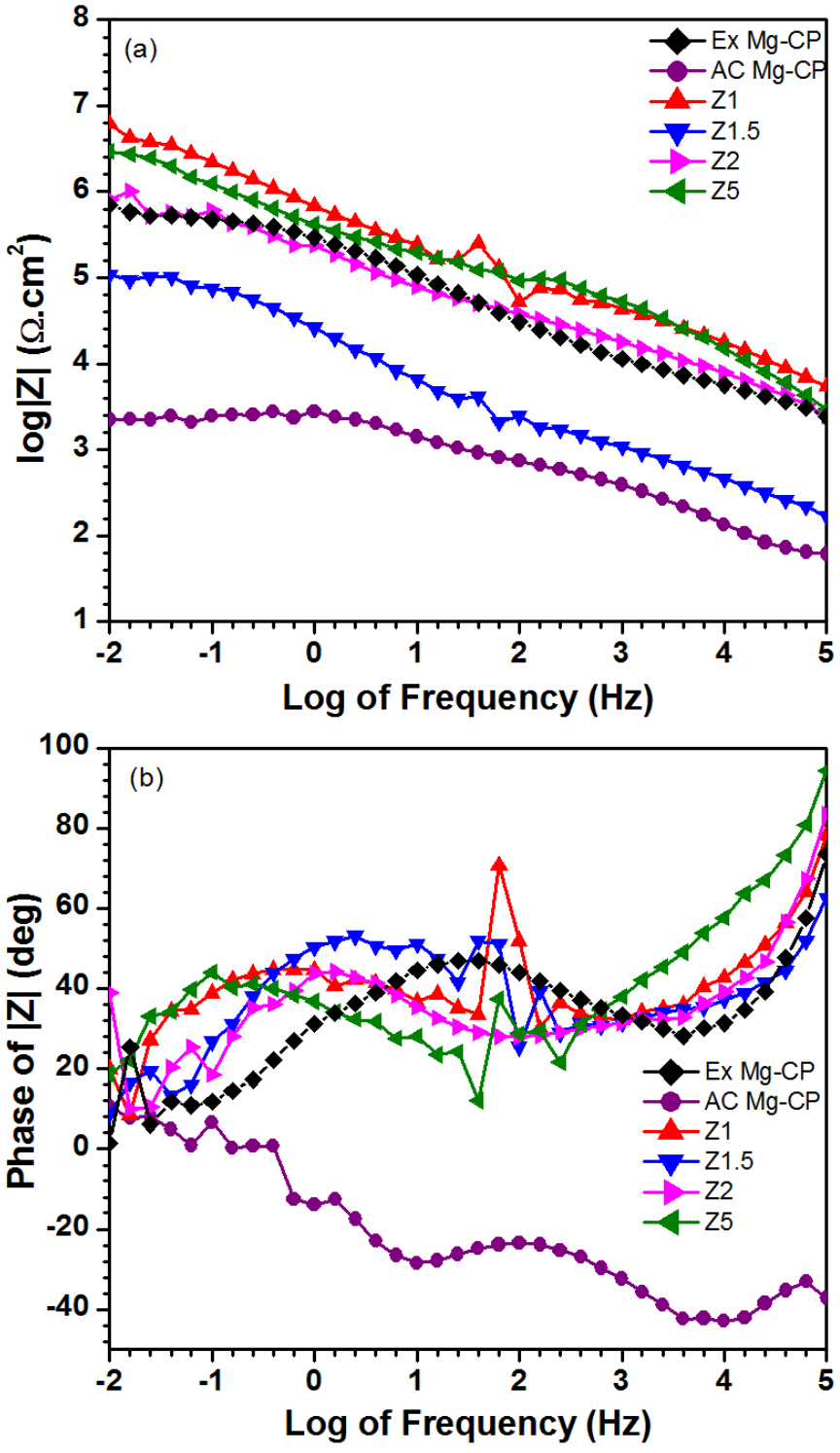

Figure 4.18 Bode (a) magnitude and; (b) phase plots for all samples

In the Bode phase plot (Figure 4.18(b)), the capacitive effect is seen in the form of the broad peaks for all the samples [27]. These peaks are seen in the 0.01Hz-100Hz frequency range for all the Mg-Zn alloys confirming the results of the Bode magnitude plots that the alloys

primarily exhibit capacitive behavior before passive film formation. The capacitive peaks for Ex Mg-CP and AC Mg-CP lie in the 0.1Hz-10,000Hz and 10Hz-10,000Hz frequency ranges, respectively. The absence of a constant phase angle indicates to the absence of stable passivation of the metal samples [22]. In the high frequency region, the capacitance of the electrical double layer behaves as a short circuit, therefore the phase angles should approach zero. However, the phase angles seem to be increasing with log(frequency), pointing to the presence of another electrical component.

The electrical circuit shown in Figure 4.19(a) was obtained after curve fitting the Nyquist parameters. The RC(RW) model fits well with the experimental data with acceptable individual error and low Chi-squared value (in the order of 10^{-2}). In Figure 4.19(a), R_s is the solution resistance between the working and reference electrodes, R_{ct} is the resistance to Charge Transfer / Polarization, C_{dl} is the capacitance of the electrical double layer at the electrode/solution interface and W is the Warburg Impedance accounting for diffusion of ions from the bulk electrolyte to the electrode interface or vice versa [75]. The values for these electrical parameters for the different samples are given in Table 4.5 with the error percentage in parenthesis. The extremely low R_s for AC Mg-CP might have occured due to some experimental artefact. However, this deviation was seen in all three repeats of the EIS experiments (The remaining repeats can be found in Appendix A). The high W of AC Mg-CP might be due to a greater diffusion range for the ions in the low frequency range as a result of the high C_{dl} [74]. A physical model representing the electrode/electrolyte is presented in Figure 4.19(b).

From the EIS analysis, the corrosion resistance in decreasing order for the alloys was as follows:

$$Z1 > Z2 > Z5 > Z1.5$$

This trend follows the same pattern as exhibited by the average polarization corrosion rates, depicted in Figure 4.16. However, the effect of Zn seems to be vague as Z1.5 has the least corrosion resistance.

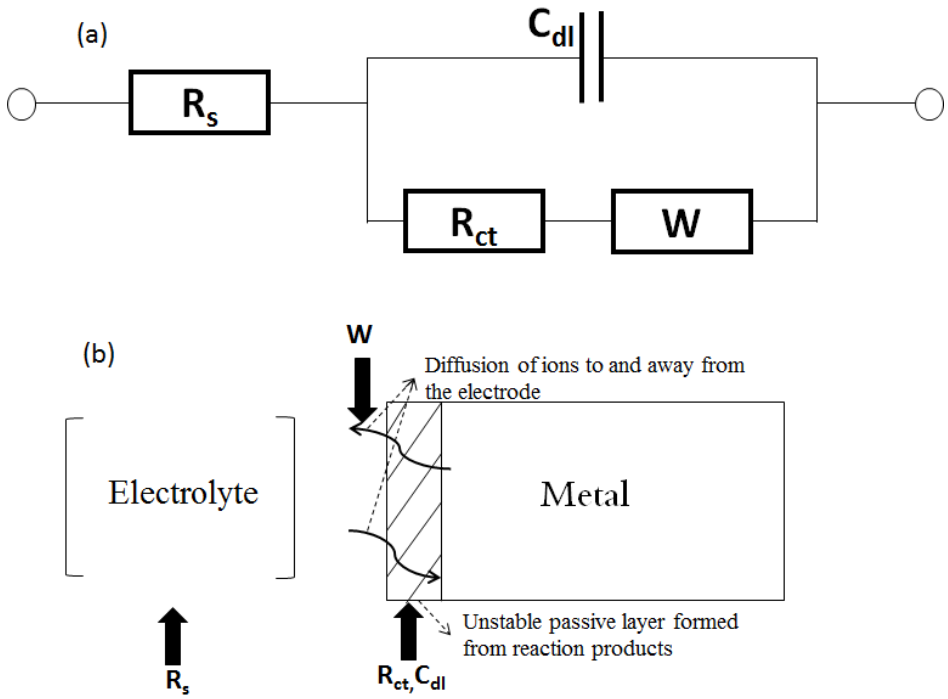

Figure 4.19 (a) Equivalent electrochemical circuit for the corrosion model; (b) physical model of the electrode/electrolyte interface

Table 4.5 Values of the electrical parameters of the curve fitted EIS data

Material	**R_s (10^6 Ω.cm^2)**	**C_{dl} (10^{-10} µF)**	**R_{ct} (10^4 Ω.cm^2)**	**W (10^{-7})**	**Chi-squared**
Ex Mg-CP	0.7921 (7.196)	5.86 (12.57)	0.3543 (11.78)	11.56 (4.224)	2.094 x 10^{-2}
AC Mg-CP	19.72 x 10^{-6} (32.42)	3.541x10^{23} (7.946x10^{16})	0.2567 (5.064)	328.8 (6.289)	3.280 x 10^{-2}
Z1	10.31 (27.88)	3.234 (14.00)	1.649 (16.54)	4.494 (6.411)	5.867 x 10^{-2}
Z1.5	.2189 (19.48)	79.85 (17.82)	0.0282 (17.17)	148.6 (5.472)	4.605 x 10^{-2}
Z2	1.144 (13.62)	7.342 (11.17)	0.9329 (11.43)	14.22 (6.737)	4.479 x 10^{-2}
Z5	6.476 (30.59)	6.952 (8.408)	5.388 (10.47)	8.259 (7.935)	5.140 x 10^{-2}

The values in the parenthesis represent the percentage error.

4.5.4. Post-polarization Microstructure

In Figure 4.20, the corrosion surface after polarization is seen using the SE mode in the SEM. The extensive and deep pitting seen after the immersion testing (Figure 4.9) is absent after polarization testing with the corroded region exhibiting a cracked appearance with white corrosion products deposited in some regions. Also, the shallow corrosion was observed to be spread out more uniformly on the polarized surface in comparison to the immersion samples (Figure 4.8). This could have occurred due to galvanic cell formation between the corroded (with more positive E_{corr}) and non-corroded (with more negative E_{corr}) regions of the sample [76]. This phenomenon drives the corrosion of the non-corroded regions while retarding the corrosion of the corroded region, thus resulting in shallow and uniform corrosion on the polarized surface [76]. The insets in Figure 4.20 show these microcracks on the surface clearly. These microcracks resemble the cracked microstructure observed in Z2 and Z5 alloys in Figure 4.9(d) and (e), as indicated by the arrows. This suggests that the microcracks appear during the initial stages of the corrosion process and later lead to pitting and/or localized corrosion, as explained in section 4.4.1. A similar appearance of microcracks was witnessed after the immersion of magnesium alloys in Hank's solution for 24 hours [51] consolidating the fact that the observed microcracks appeared in the early stage of the corrosion process.

On performing X-EDS on the polarized samples, the presence of Ca and/or P was detected, as shown in Figure 4.21. This confirms that calcium phosphates were one of the corrosion products, further reinforcing the FTIR and XRD results presented previously in Figure 4.12 and Figure 4.13, respectively. In all the X-EDS spectra, the presence of Ca and P seem to be analogous to each other except for the Z2 alloy (Figure 4.21(d)). This could have happened as quantity of P might have been below the detection limit of the X-EDS detector. The uniform distribution of Ca and P throughout the samples indicates the formation of a Ca-P coating, which might be beneficial in reducing the corrosion rate of the samples [72]. Additionally presence of salt in the form of crystals was also seen in some portions of the X-EDS spectrum, as seen in the Z1 and Z1.5 alloys in Figure 4.21, where the chlorine and sodium content are overlapping one another. In the Z5 alloy (Figure 4.21(e)), the X-EDS map for Zn resembles the network-like appearance seen previously in Figure 4.11(e).

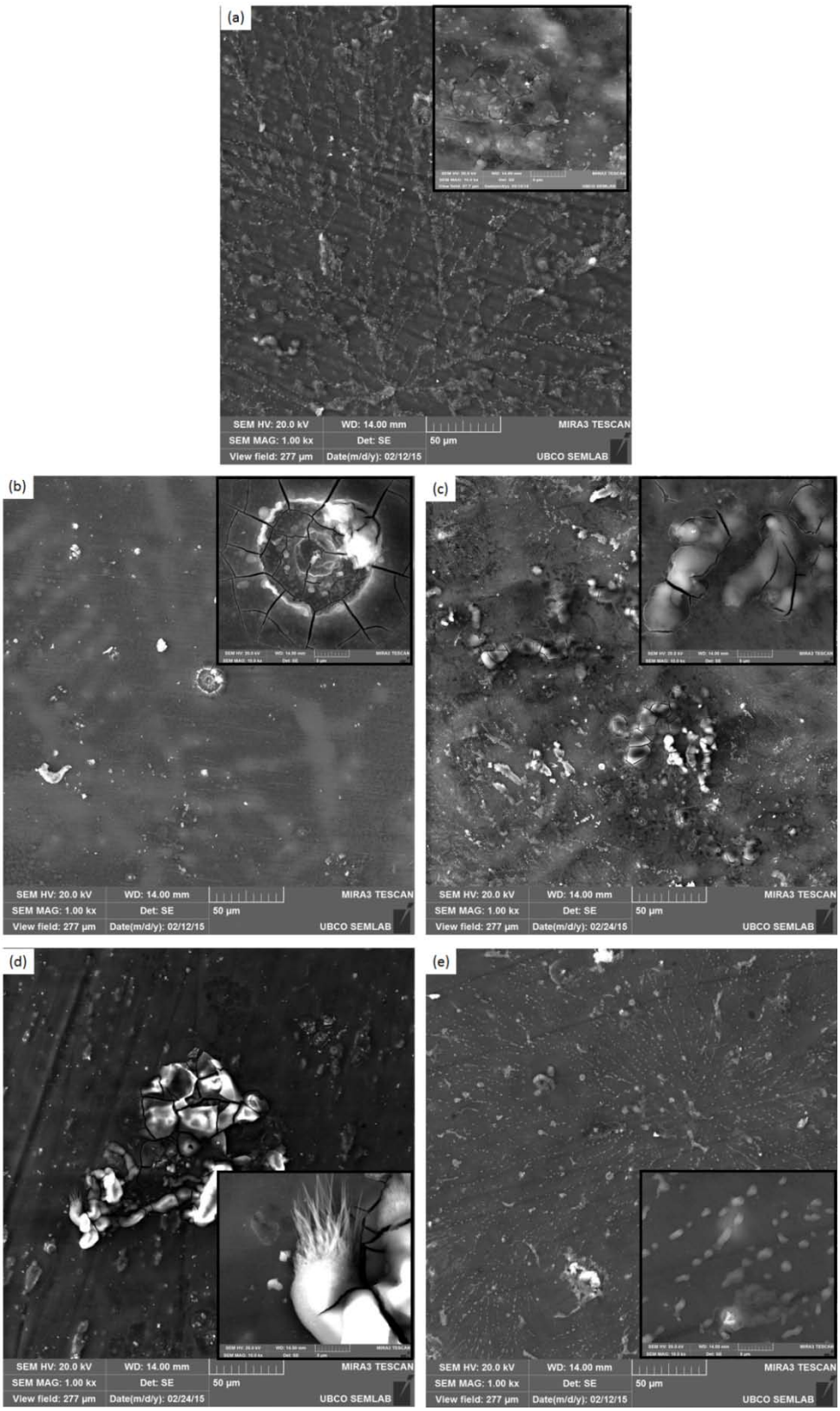

Figure 4.20 SEM images of corroded surfaces of (a) Ex Mg-CP; (b) Z1; (c) Z1.5; (d) Z2; (e) Z5 samples after dynamic polarization tests. Insets show close-up images at 10000X magnification

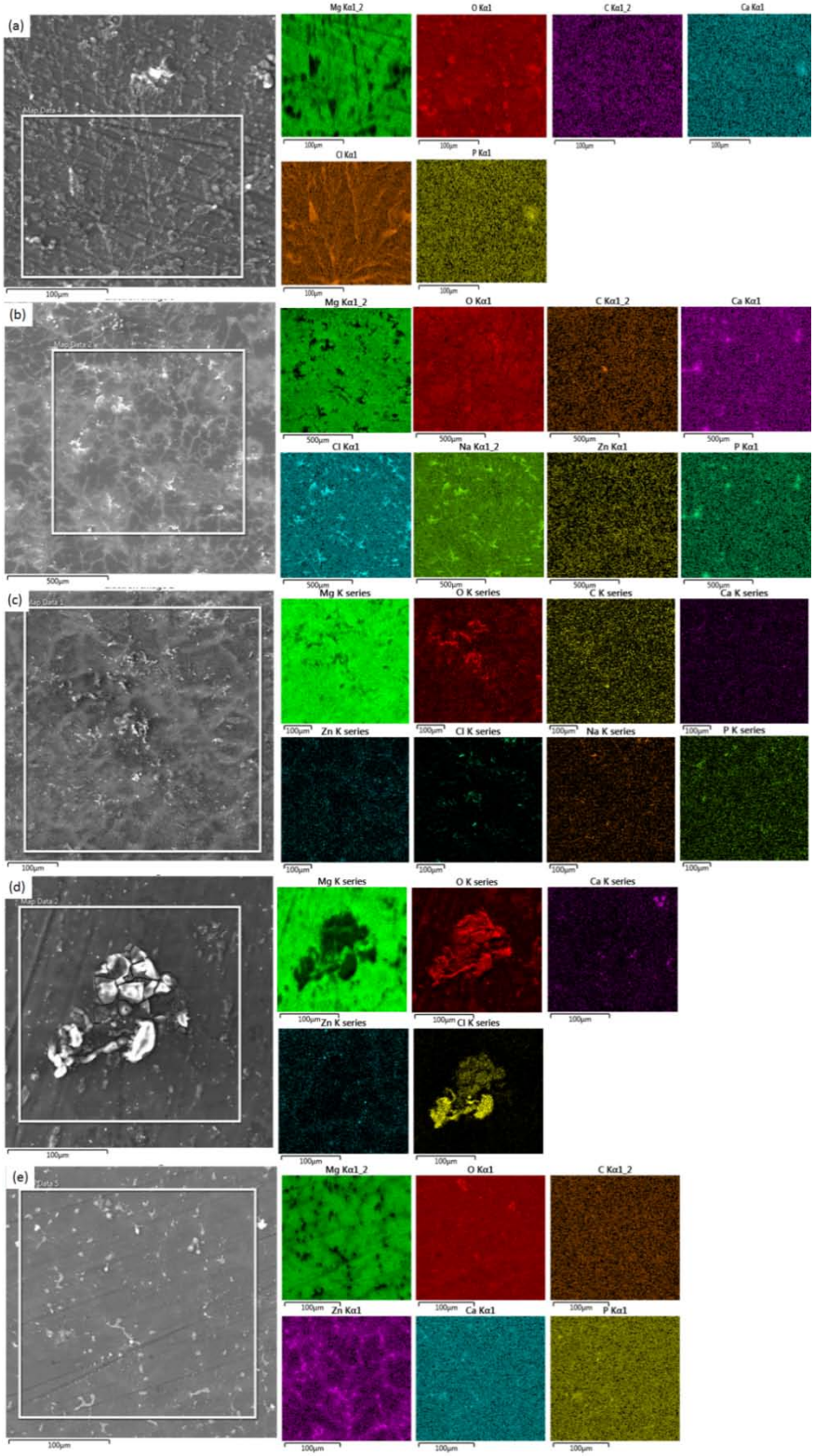

Figure 4.21 SEM images of corroded (a) Ex Mg-CP; (b) Z1; (c) Z1.5; (d) Z2; (e) Z5 alloys after dynamic polarization tests showing the area mapped X-EDS spectra

4.6. Variation Among the *in vitro* Techniques

The variation in the corrosion rates between the immersion and electrochemical tests is quite significant. The extensive pitting corrosion observed in Figure 4.9 in comparison to Figure 4.20 could have occurred due to several factors. Firstly, as the samples for immersion and polarization were taken from different sections of the as-cast ingots, the inhomogeneity in as-cast specimens arising from microstructural changes and non-uniform Zn distribution, could have led to variation in corrosion results between the two testing methods. Secondly, the polarization experiments were carried out at room temperature while the immersion experiments were conducted at the human body temperature which might have affected the polarization results as noted previously by Kirkland *et al.* [55]. The significant difference between the ratio of corrosion rates between the Ex-Mg CP and AC Mg-CP within the two techniques (see Figure 4.10 and Figure 4.16) was a result of localized corrosion in the AC Mg-CP which would have resulted in particle undermining. The electrochemical technique does not account for this scenario and therefore resulted in an exaggerated corrosion [65].

Variation in gravimetric and polarization corrosion rates for AZ91D was reported previously [77] and it was postulated that the polarization results represent the beginning of the corrosion process whereas the immersion testing by weight loss or hydrogen evolution method yields the average corrosion rate over a period of time. This result was experimentally validated by polarizing ZE41 samples after 0 hours and 48 hours immersion time [78]. It was found from the respective Tafel plots that samples immersed for 48 hours attained steady state corrosion whereas, the 0 hour immersion samples yielded low corrosion rates with less H_2 evolution indicating the onset of corrosion [78]. A similar sort of early onset corrosion combined with the aforementioned reasons, seems to have resulted in the extremely low corrosion rates in the polarization studies conducted in this research.

Further, some studies have suggested that potentiodynamic polarization is not a suitable method for obtaining the actual corrosion rates of fast corroding magnesium alloys as the test accelerates corrosion reactions to occur within a short time frame [79, 80]. Thus, it was concluded that the electrochemical polarization technique was representative of the onset of corrosion while the immersion technique was representative of the average corrosion rates of the magnesium alloys.

Chapter 5 : CONCLUSIONS AND FUTURE WORK

5.1. Conclusions

Pure Mg and Mg-Zn alloys were successfully fabricated by permanent mold casting. All samples were characterized using Optical Microscopy, SEM – X-EDS and XRD prior to mechanical testing (Vickers Hardness) and *in vitro* corrosion (static immersion, electrochemical polarization and EIS) testing followed by post-corrosion analysis. The conclusions drawn from the experiments and characterization techniques are as follows:

(a) The as-cast alloys exhibited inhomogeneity due to oxide inclusions and turbulent liquid flow during pouring, with one sample (Z2) exhibiting centreline porosity. Grain size analysis revealed the uniform microstructure of Ex Mg-CP with the lowest grain size and the directionally solidified columnar and equiaxed grains of the AC Mg-CP with the highest grain size. Grain size of the Mg-Zn alloys decreased with increasing Zn additions. The Vickers hardness results were inversely related to the grain sizes of all samples and increased with subsequent Zn additions.

(b) Microstructural analysis of the alloys confirmed the non-homogenous distribution of alloying elements with Zn detected in the interdendritic regions. The second phases which appeared along the dendrite boundaries in the Z1.5 alloy formed network like connections in the Z2 alloy. Fragmentation of these second phase networks was observed in the Z5 alloy and the second phase was identified to be $MgZn_2$ with the aid of XRD.

(c) The immersion corrosion tests revealed that among the as-cast samples, the Z2 alloy possessed highest corrosion resistance when immersed for 10 days in SBF at 37°C and a pH of 7.4. The ranking of the samples in the order of highest to least corrosion resistance was:

Z2 > Ex Mg-CP > Z1.5 > Z1 > Z5 > AC Mg-CP

The Ex Mg-CP was highly corrosion resistant due to the least grain size. The corrosion rate of AC Mg-CP improved by more than 50% with 1 wt.% Zn addition. Among the alloys, corrosion resistance was dependent on the $MgZn_2$ phase distribution. The networks of $MgZn_2$ formed in Z2 alloy acted as physical barrier to

the corrosion of the α(Mg) matrix, while the fragmentation of the networks in the Z5 alloy resulted in microgalvanic corrosion due to increase in the number of micro-cathodic ($MgZn_2$) and micro-anodic (α(Mg)) sites.

(d) Analysis of the corrosion surface morphology revealed that the Mg-Zn alloys had undergone non-uniform corrosion with preferential corrosion occurring in some regions. It was determined with the aid of FTIR and XRD that the corrosion products were composed of magnesium carbonates, magnesium hydroxides and calcium phosphates which were weakly adhered to the sample and were disintegrated by the penetration of the strong SBF electrolyte.

(e) The polarization testing revealed that the Z1 alloy exhibited the least corrosion rate in aerated SBF at room temperature. The corrosion rate in increasing order for all the samples was:

Z1 > Z2 > Z5 > Ex Mg-CP > Z1.5 > AC Mg-CP

Analysis of the polarization plots revealed the formation and dissolution of a passivation film (possibly $Mg(OH)_2$). EIS analysis of the electrode-electrolyte interface was correlated by a (RC(RW)) electrical equivalent circuit where, diffusion of reactants and products across the electrical double layer seemed to play a significant role. Though introduction of Zn improved the corrosion resistance of Mg, effect of varying Zn content among the alloys seemed to be inconclusive.

(f) Microstructure of the polarized surfaces presented with microcracks, characteristic of the onset of corrosion. The corrosion products on the polarized surface of the samples studied with X-EDS revealed uniform and analogous distribution of calcium and phosphorous, indicating to the formation of calcium phosphates which further retarded the corrosion rates in comparison to the immersion results.

(g) Significant variation in the immersion and polarization corrosion rates can be explained by the inhomogeneity within the as-cast ingots of each sample and variation in the testing environment (temperature and free-aeration in polarization experiments). Furthermore, the polarization results are representative of the initial stages of corrosion whereas, the immersion results are representative of steady state corrosion thus yielding the average corrosion of the samples.

5.2. Limitations of Work

(a) The chemical inhomogeneity in the as-cast samples contributed to the lack of reproducibility. Enhancing homogeneity might yield more consistent data.

(b) The static condition of the SBF and absence of external loading during immersion and polarization testing do not closely simulate the *in vivo* human body environment and therefore may yield lower corrosion rates.

(c) The temperature in which the electrochemical testing was carried out was not controlled to represent the physiological human body temperature which might have affected the corrosion rates. Additionally pH monitoring was not done, which could reveal interesting information about the passive film formation.

5.3. Scope for Future Work

(a) The effect of the $MgZn_2$ second phase on corrosion control may be further analyzed by plotting the Temperature-Time curves during casting to identify when the phase transformation is occurring.

(b) As the grain size seems to significantly affect the corrosion rate, grain refinement through extrusion and addition of biocompatible grain refiners may be done.

(c) Further mechanical tests, such as Tensile, Compressive and Fatigue testing should be carried out to determine critical mechanical parameters keeping in mind the required strengths for use of Mg alloys in orthopaedic applications.

(d) *In vitro* corrosion testing in dynamic environment by circulating the SBF and simultaneous cyclic loading can be performed to simulate the *in vivo* environment as closely as possible.

(e) As corrosion is a surface property, the surface roughness of the samples might play a significant role in determining the corrosion rates. Thus, studies related to variation in surface roughness through surface modification techniques may be conducted.

(f) Toxicity measurement of Mg-Zn alloys by using cytotoxicity tests with appropriate cell cultures to determine the biocompatibility of the alloys need to be carried out. Further, the alloys can then be used to study the amount of cell adhesion using Micro-computed Tomography followed by *in vivo* corrosion testing to explore the biomedical potential of these alloys.

Bibliography

[1] F. Witte, "The history of biodegradable magnesium implants: a review," *Acta Biomaterialia,* vol. 6, no. 5, pp. 1680-1692, 2010.

[2] S. V. Bhat, Biomaterials, New Delhi, India: Alpha Science International Ltd, 2002.

[3] J. Billette and T. Janz, "Statistics Canada," Government of Canada, 28 06 2011. [Online]. Available: http://www.statcan.gc.ca/pub/82-624-x/2011001/article/11506-eng.htm.

[4] C. K. Seal, K. Vince and M. A. Hodgson, "Biodegradable surgical implants based on magnesium alloys - A review of current research," in *IOP Conference series: Materials Science and Engineering*, 2009.

[5] D. R. Sumner and J. O. Galante, "Determinants of stress shielding: design versus materials versus interface," *Clinical orthopaedics and related research,* vol. 274, pp. 202-212, 1992.

[6] M. Salashoor and Y. Guo, "Biodegradable orthopedic magnesium-calcium (MgCa) alloys, processing, and corrosion performance," *Materials,* vol. 5, no. 1, pp. 135-155, 2012.

[7] K. A. Athanasiou, G. G. Niederauer and C. Agrawal, "Sterilization, toxicity, biocompatibility and clinical applications of polylactic acid/polyglycolic acid copolymers," *Biomaterials,* vol. 17, no. 2, pp. 93-102, 1996.

[8] M. N. Rahaman, D. E. Day, B. Sonna Bal, Q. Fu, S. B. Jung, L. F. Bonewald and A. P. Tomsia, "Bioactive glass in tissue engineering," *Acta Biomaterialia,* vol. 7, no. 6, pp. 2355-2373, 2011.

[9] X. N. Gu and Y. F. Zheng, "A review on magnesium alloys as biodegradable materials Frontiers of Materials Science in China," *Frontiers of Materials Science in China,* vol. 4, no. 2, pp. 111-115, 2010.

[10] M. P. Staigner, A. M. Pietal, J. Huadmai and G. Dias, "Magnesium and its alloys as orthopedic biomaterials: a review," *Biomaterials,* vol. 27, no. 9, pp. 1728-1734, 2006.

[11] F. Witte, V. Kaese, H. Haferkamp, E. Switzer, A. Meyer-Lindenberg, C. J. Wirth and H. Windhagen, "In vivo corrosion of four magnesium alloys and the associated bone response," *Biomaterials,* vol. 26, no. 17, pp. 3557-3563, 2005.

[12] F. Witte, N. Hort, C. Vogt, S. Cohen, K. U. Kainer, R. Willumeit and F. Feyerabend, "Degradable biomaterials based on magnesium corrosion," *Current opinion in solid state and materials science,* vol. 12, no. 5, pp. 63-72, 2008.

[13] J. Vormann, "Magnesium: nutrition and metabolism," *Molecular aspects of medicine,* vol. 24, no. 1, pp. 27-37, 2003.

[14] L. Xu, G. Yu, E. Zhang, F. Pan and K. Yang, "In vivo corrosion behavior of Mg-Mn-Zn alloy for bone implant application," *Journal of Biomedical Materials Research Part A,* vol. 83, no. 3, pp. 703-711, 2007.

[15] C. Castellani, R. A. Lindtner, P. Hausbrandt, E. Tschegg, S. E. Stanzl-Tschegg, G. Zanoni and A. M. Weinberg, "Bone–implant interface strength and osseointegration: biodegradable magnesium alloy versus standard titanium control," *Acta Biomaterialia,* vol. 7, no. 1, pp. 432-440, 2011.

[16] Y. Chen, Z. Xu, C. Smith and J. Sankar, "Recent advances on the development of magnesium alloys for biodegradable implants," *Acta Biomaterialia,* vol. 10, no. 11, pp. 4561-4573, 2014.

[17] D. F. Williams, "On the mechanisms of biocompatability," *Biomaterials,* vol. 29, no. 30, pp. 2941-2953, 2008.

[18] B. D. Ratner, "The biocompatibility manifesto: biocompatibility for the twenty-first century," *Journal of cardiovascular translational research,* vol. 4, no. 5, pp. 523-527, 2011.

[19] B. Heness and B. Ben-Nissan. [Online]. Available: http://www.azom.com/article.aspx?ArticleID=2630#_Bioinert_Biomaterials. [Accessed 16 February 2013].

[20] J. Park and R. S. Lakes, Biomaterials: An Introduction, Springer Science & Business Media, 2007.

[21] K. Wang, "The use of titanium for medical applications in the USA," *Material Science and Engineering: A,* vol. 213, no. 1, pp. 134-137, 1996.

[22] R. Ummethala, F. Despang, M. Gelinsky and B. Basu, "In vitro corrosion and mineralization of novel Ti–Si–C alloy," *Electrochimica Acta,* vol. 56, no. 11, pp. 3809-3820, 2011.

[23] K. A. Athanasiou, G. G. Niederauer and C. M. Agrawal, "Sterilization, toxicity, biocompatibility and clinical applications of polylactic acid/ polyglycolic acid copolymers," *Biomoterials,* vol. 17, pp. 93-102, 1996.

[24] X. Gu, Y. Zheng, S. Zhong, T. Xi, J. Wang and W. Wang, "Corrosion of, and cellular responses to Mg–Zn–Ca bulk metallic glasses," *Biomaterials,* vol. 31, no. 6, pp. 1093-1103, 2010.

[25] H. S. Brar, M. O. Platt, M. Sarntinoranont, P. I. Martin and M. V. Manuel, "Magnesium as a biodegradable and bioabsorbable material for medical implants," *Jom,* vol. 61, no. 9, pp. 31-34, 2009.

[26] K. F. Farraro, K. E. Kim, S. L. Woo, J. R. Flowers and M. B. McCullough, "Revolutionizing orthopaedic biomaterials: The potential of biodegradable and bioresorbable magnesium-based materials for functional tissue engineering," *Journal of biomechanics,* vol. 47, no. 9, pp. 1979-1986, 2014.

[27] M. Mandal, A. P. Moon, G. Deo, C. L. Mendis and K. Mondal, "Corrosion behavior of Mg–2.4 Zn alloy micro-alloyed with Ag and Ca," *Corrosion Science,* vol. 78, pp. 172-182, 2014.

[28] T. B. Abbott, "Why choose magnesium?," *Materials Science Foum,* vol. 618, pp. 3-6, 2009.

[29] J. W. Seo and T. J. Park, "Magnesium metabolism," *Electrolyte & Blood Pressure,* vol. 6, no. 2, pp. 86-95, 2008.

[30] G. L. Song and A. Atrens, "Corrosion mechanisms of magnesium alloys," *Advanced engineering materials,* no. 1, pp. 11-33, 1999.

[31] Z. Li, X. Gu, S. Lou and Y. Zheng, "The development of binary Mg–Ca alloys for use as biodegradable materials within bone," *Biomaterials,* vol. 29, no. 10, pp. 1329-1344, 2008.

[32] G. Song, "Control of biodegradation of biocompatable magnesium alloys," *Corrosion Science,* vol. 49, no. 4, pp. 1696-1701, 2007.

[33] S. Zhang, X. Zhang, C. Zhao, Y. Song, C. Xie and Y. Bian, "Research on an Mg–Zn alloy as a degradable biomaterial," *Acto Biomaterialia,* vol. 6, no. 2, pp. 626-640, 2010.

[34] E. Zhang, L. Xu, G. Yu, F. Pan and K. Yang, "In vivo evaluation of biodegradable magnesium alloy bone implant in the first 6 months implantation," *Journal of*

Biomedical Materials Research Part A, vol. 90, no. 3, pp. 882-893, 2009.

[35] L. Choudhary and R. S. Raman, "Magnesium alloys as body implants: fracture mechanism under dynamic and static loadings in a physiological environment," *Acta biomaterialia,* vol. 8, no. 2, pp. 916-923, 2012.

[36] E. Zhang, D. Yin, L. Xu, L. Yang and K. Yang, "Microstructure, mechanical and corrosion properties and biocompatibility of Mg–Zn–Mn alloys for biomedical application," *Materials Science and Engineering: C,* vol. 29, no. 3, pp. 987-993, 2009.

[37] Y. Sun, B. Zhang, Y. Wang, L. Geng and X. Jiao, "Preparation and characterization of a new biomedical Mg–Zn–Ca alloy," *Materials & Design,* vol. 34, pp. 58-64, 2012.

[38] L. Geng, B. P. Zhang, A. B. Li and D. C. C, "Microstructure and mechanical properties of Mg–4.0 Zn–0.5 Ca alloy," *Materials Letters,* vol. 63, no. 5, pp. 557-559, 2009.

[39] D. T. Chou, D. Hong, P. Saha, J. Ferrero, B. Lee, Z. Tan, Z. Dong and P. N. Kumta, "In vitro and in vivo corrosion, cytocompatibility and mechanical properties of biodegradable Mg–Y–Ca–Zr alloys as implant materials," *Acta biomaterialia,* vol. 9, no. 10, pp. 8518-8533, 2013.

[40] J. B. Clark, L. Zabdyr and Z. Moser, "Mg (Magnesium) Binary Alloy Phase Diagrams, 1988," in *Alloy Phase Diagrams*, vol. 3, ASM Handbook Online, , http://products.asminternational.org/hbk/index.jsp, ASM International, 1992, pp. 2250-2285. [Accessed 20 August 2015].

[41] M. Mezbahul-Islam, A. O. Mostafa and M. Medraj, "Essential magnesium alloys binary phase diagrams and their thermochemical data," *Journal of Materials,* 2014.

[42] J. B. Clark, L. Zabdyr and Z. Moser, "Mg (Magnesium) Binary Alloy Phase Diagrams, 1988," ASM Handbook Online, ASM International, 1992. [Online]. Available: http://www.himikatus.ru/art/phase-diagr1/Mg-Zn.php. [Accessed 16 August 2015].

[43] L. Y. Wei, G. L. Dunlop and H. Westengen, "The intergranular microstructure of cast Mg-Zn and Mg-Zn-rare earth alloys," *Metallurgical and Materials Transactions A,* vol. 26, no. 8, pp. 1947-1955, 1995.

[44] M. Paliwal and I. H. Jung, "Microstructural evolution in Mg–Zn alloys during solidification: An experimental and simulation study," *Journal of Crystal Growth,* vol. 394, pp. 28-38, 2014.

[45] B. S. Murty, "Advanced Metallurgical Thermodynamics," National Programme on

Technology Enhanced Learning, Ministry of Human Resource Development, Government of India, [Online]. Available: http://nptel.ac.in/courses/113106031/. [Accessed 31 March 2015].

[46] Y. Song, E. H. Han, D. Shan, C. D. Yim and B. S. You, "The effect of Zn concentration on the corrosion behavior of Mg–xZn alloys," *Corrosion Science,* vol. 65, pp. 322-330, 2012.

[47] M. Bamberger and V. S. J. B. Levi, "Precipitation hardening in Mg-Ca-Zn alloys," *Metallurgical and Materials Transactions A,* vol. 37, no. 2, pp. 481-487, 2006.

[48] W. D. Callister, Materials Science and Engineering: An Introduction, 7th ed., New York: John Wiley & Sons Inc., 1940.

[49] E. Zhang and L. Yang, "Microstructure, mechanical properties and bio-corrosion properties of Mg–Zn–Mn–Ca alloy for biomedical application," *Materials Science and Engineering: A,* vol. 497, no. 1, pp. 111-118, 2008.

[50] B. P. Zhang, L. Geng and Y. Wang, "Research on Mg-Zn-Ca alloy as degradable biomaterial," *INTECH Open Access Publisher,* 2011.

[51] H. Du, Z. Wei, X. Liu and E. Zhang, "Effects of Zn on the microstructure, mechanical property and bio-corrosion property of Mg–3Ca alloys for biomedical application," *Materials Chemistry and Physics,* vol. 125, no. 3, pp. 568-575, 2011.

[52] ASTMG31-2012a, "Standard Guide for Laboratory Immersion Corrosion Testing of Metals," ASTM International, West Conshohocken, PA, 2012.

[53] ASTMG102-89, "Standard Practice for Calculation of Corrosion Rates and Related Information from Electrochemical Measurements," ASTM International, West Conshohocken, PA, 2010.

[54] Y. Xin, T. Hu and P. K. Chu, "In vitro studies of biomedical magnesium alloys in a simulated physiological environment: a review," *Acta biomaterialia,* vol. 4, p. 7, 2011.

[55] N. T. Kirkland, J. Lespagnol and N. Birbilis, "A survey of bio-corrosion rates of magnesium alloys," *Corrosion Science,* vol. 52, no. 2, pp. 287-291, 2010.

[56] J. Walker, S. Shadanbaz, N. T. Kirkland, E. Stace, T. Woodfield, M. P. Staiger and G. J. Dias, "Magnesium alloys: predicting in vivo corrosion with in vitro immersion testing," *Journal of Biomedical Materials Research Part B: Applied Biomaterials,* vol. 100, no. 4, pp. 1134-1141, 2012.

[57] C. A. Dinarello and R. Porat, "Fever and Hyperthermia," in *Harrison's Principles of Internal Medicine,* 18th ed., New York, NY: McGraw-Hill, 2012.

[58] "Materials Evaluation and Enginering Inc.," [Online]. Available: http://mee-inc.com/esca.html. [Accessed 6 February 2015].

[59] D. S. Yin, E. L. Zhang and S. Y. Zeng, "Effect of Zn on mechanical property and corrosion property of extruded Mg-Zn-Mn alloy," *Transactions of Nonferrous Metals Society of China,* vol. 18, no. 4, pp. 763-768, 2008.

[60] B. Zhang, Y. Hou, X. Wang, Y. Wang and L. Geng, "Mechanical properties, degradation performance and cytotoxicity of Mg–Zn–Ca biomedical alloys with different compositions," *Materials Science and Engineering: C,* vol. 31, no. 8, pp. 1667-1673, 2011.

[61] H. K. D. H. Bhadeshia, "Dendritic Solidification," University of Cambridge, [Online]. Available: http://www.msm.cam.ac.uk/phase-trans/dendrites.html. [Accessed 20 05 2015].

[62] J. E. Catalano and L. J. Kecskes, *A Generic Metallographic Preparation Method for Magnesium Alloys,* ARMY RESEARCH LAB ABERDEEN PROVING GROUND MD WEAPONS AND MATERIALS RESEARCH DIRECTORATE, 2013.

[63] G. Vander Voort, *Metallography of Magnesium and its Alloys,* Buehler Tech-Notes.

[64] S. Cai, T. Lei, N. Li and F. Feng, " Effects of Zn on microstructure, mechanical properties and corrosion behavior of Mg–Zn alloys," *Materials Science and Engineering: C,* vol. 32, no. 8, pp. 2570-2577, 2012.

[65] G. Song and A. Atrens, "Understanding magnesium corrosion," *Advanced Engineering Materials,* vol. 5, no. 12, pp. 837-858, 2003.

[66] M. Alvarez-Lopez, M. D. Pereda, J. A. Del Valle, M. Fernandez-Lorenzo, M. C. Garcia-Alonso, O. A. Ruano and M. L. Escudero, "Corrosion behaviour of AZ31 magnesium alloy with different grain sizes in simulated biological fluids," *Acta Biomaterialia,* vol. 6, no. 5, pp. 1763-1771, 2010.

[67] Z. Grubač, M. Metikoš-Huković and R. Babić, "Electrocrystallization, growth and characterization of calcium phosphate ceramics on magnesium alloys," *Electrochimica Acta,* vol. 109, pp. 694-700, 2013.

[68] Y. Zhu, G. Wu, Y. H. Zhang and Q. Zhao, "Growth and characterization of Mg (OH) 2

film on magnesium alloy AZ31," *Applied Surface Science,* vol. 257, no. 14, pp. 6129-6137, 2011.

[69] J. E. Gray-Munro and M. Strong, "The mechanism of deposition of calcium phosphate coatings from solution onto magnesium alloy AZ31," *Journal of Biomedical Materials Research Part A,* vol. 90, no. 2, pp. 339-350, 2009.

[70] Y. Pekounov and O. E. Petrov, "Bone resembling apatite by amorphous-to-crystalline transition driven self-organisation," *Journal of Materials Science: Materials in Medicine,* vol. 19, no. 2, pp. 753-759, 2008.

[71] C. A. O. Ramirez, A. M. Costa, J. Bettini, A. J. Ramirez, M. H. Prado da Silva and A. M. Rossi, "Structural properties of nanostructured carbonate apatites," *Key Engineering Materials,* vol. 396, pp. 611-614, 2009.

[72] K. F. Farraro, K. E. Kim, S. L. Woo, J. R. Flowers and M. B. McCullough, "Revolutionizing orthopaedic biomaterials: The potential of biodegradable and bioresorbable magnesium-based materials for functional tissue engineering," *Journal of biomechanics,* vol. 47, no. 9, pp. 1979-1986, 2014.

[73] H. Y. Ha, J. Y. Kang, J. Yang, C. D. Yim and B. S. You, "Limitations in the use of the potentiodynamic polarisation curves to investigate the effect of Zn on the corrosion behaviour of as-extruded Mg–Zn binary alloy," *Corrosion Science,* vol. 75, pp. 426-433, 2013.

[74] Gamry Instruments, "Basics of electrochemical impedance spectroscopy," [Online]. Available: https://www.gamry.com/application-notes/EIS/basics-of-electrochemical-impedance-spectroscopy/. [Accessed 16 July 2015].

[75] Princeton Applied Research, "Basics of Electrochemical Impedance Spectroscopy," [Online]. Available: http://www.princetonappliedresearch.com/Literature/index.aspx. [Accessed 16 July 2015].

[76] G. Song, "Recent progress in corrosion and protection of magnesium alloys," *Advanced Engineering Materials,* vol. 7, no. 7, pp. 563-586, 2005.

[77] W. Zhou, T. Shen and N. N. Aung, " Effect of heat treatment on corrosion behaviour of magnesium alloy AZ91D in simulated body fluid," *Corrosion Science,* vol. 52, no. 3, pp. 1035-1041, 2010.

[78] M. C. Zhao, M. Liu, G. L. Song and A. Atrens, "Influence of pH and chloride ion concentration on the corrosion of Mg alloy ZE41," *Corrosion Science,* vol. 50, no. 11,

pp. 3168-3178, 2008.

[79] N. T. Kirkland, N. Birbilis and M. P. Staiger, "Assessing the corrosion of biodegradable magnesium implants: a critical review of current methodologies and their limitations," *Acta biomaterialia*, vol. 8, no. 3, pp. 925-936, 2012.

[80] A. H. M. Sanchez, B. J. Luthringer, F. Feyerabend and R. Willumeit, "Mg and Mg alloys: How comparable are in vitro and in vivo corrosion rates? A review," *Acta biomaterialia*, vol. 13, pp. 16-31, 2015.

Appendix A: Corrosion Measurement Data for the Repeats of Polarization Test

The OCP values from Figure A1.1 and Figure A2.1 and E_{corr} and i_{corr} values from Figure A1.2 and Figure A2.2 were used in the calculation of average E_{corr}, i_{corr} and corrosion rates presented previously in Table 4.3 and Figure 4.16. In some cases, the Bode plot is useful in case of data scatter in the Nyquist plots which prevent adequate fitting of the semicircle [75], as seen in the case of Figure A1.3(d) and Figure A2.3(b). There are some severe deviations even in the Bode phase plots for both repeats. This could happen due to any change in the cell from its steady state condition, such as, oxide layer growth, reaction product build up, and temperature fluctuations which may lead to inaccurate EIS results [74]. Some of the values of the electrical parameters given Table A1.1 and Table A2.1 (given in italics) were erroneous and hence were not used for analyzing the electrical equivalent circuit (Figure 4.19(a)).

A1: 2nd Repeat of the Electrochemical Test

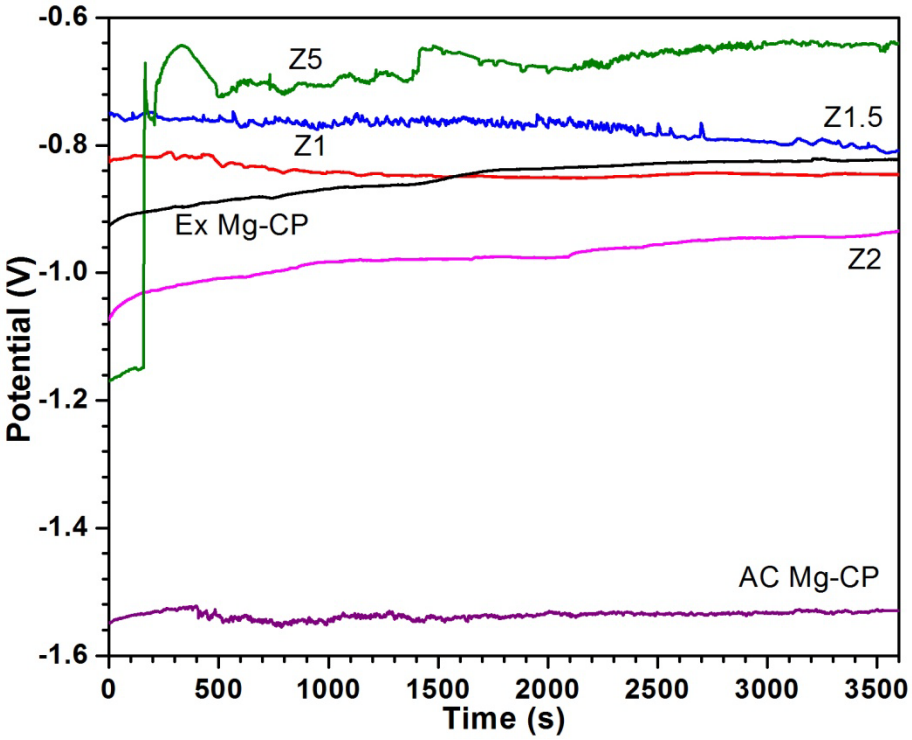

Figure A1.1 OCP vs. time plots for all samples (Repeat 2)

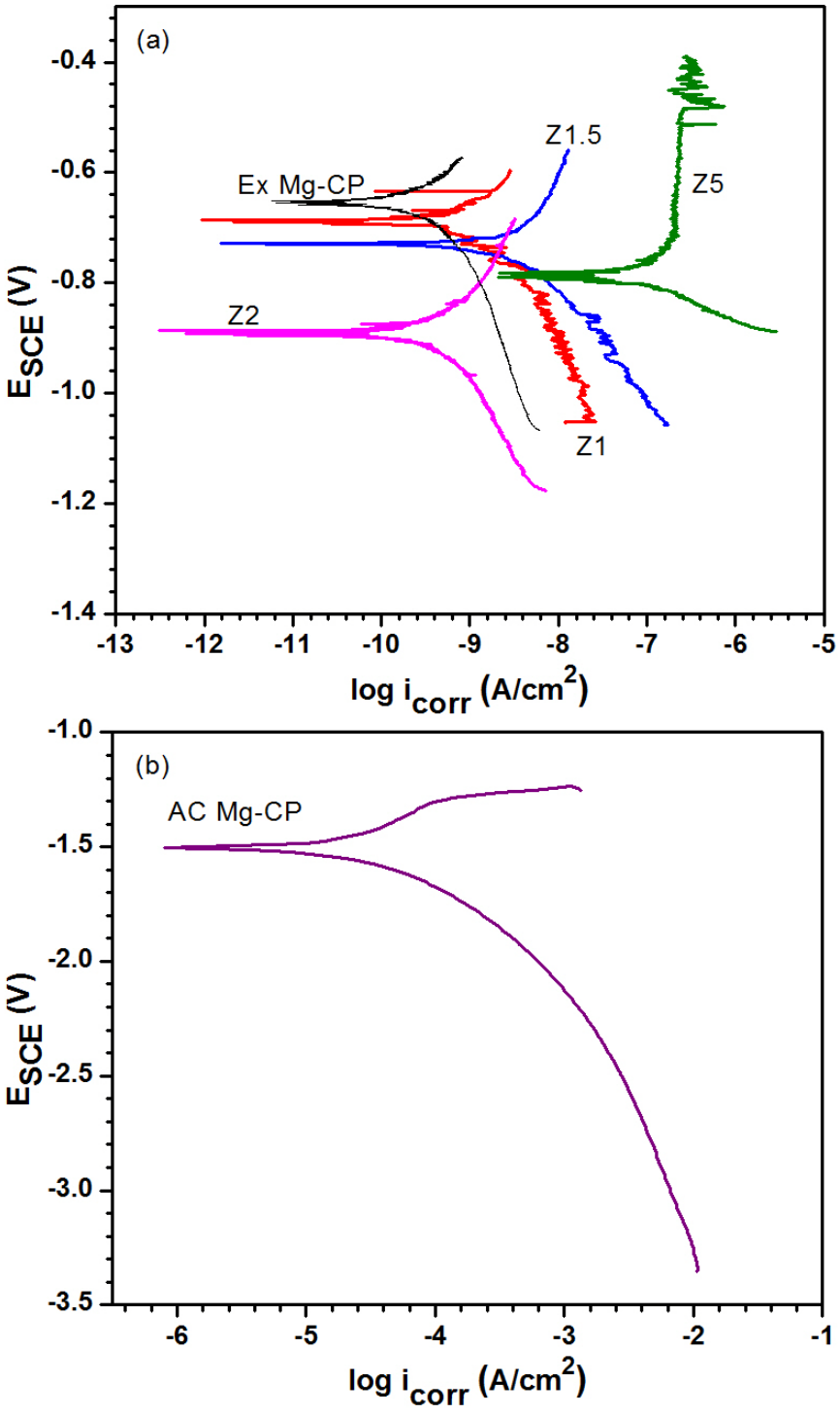

Figure A1.2 Tafel plots for (a) Ex Mg-CP and as-cast alloys; (b) AC Mg-CP (Repeat 2)

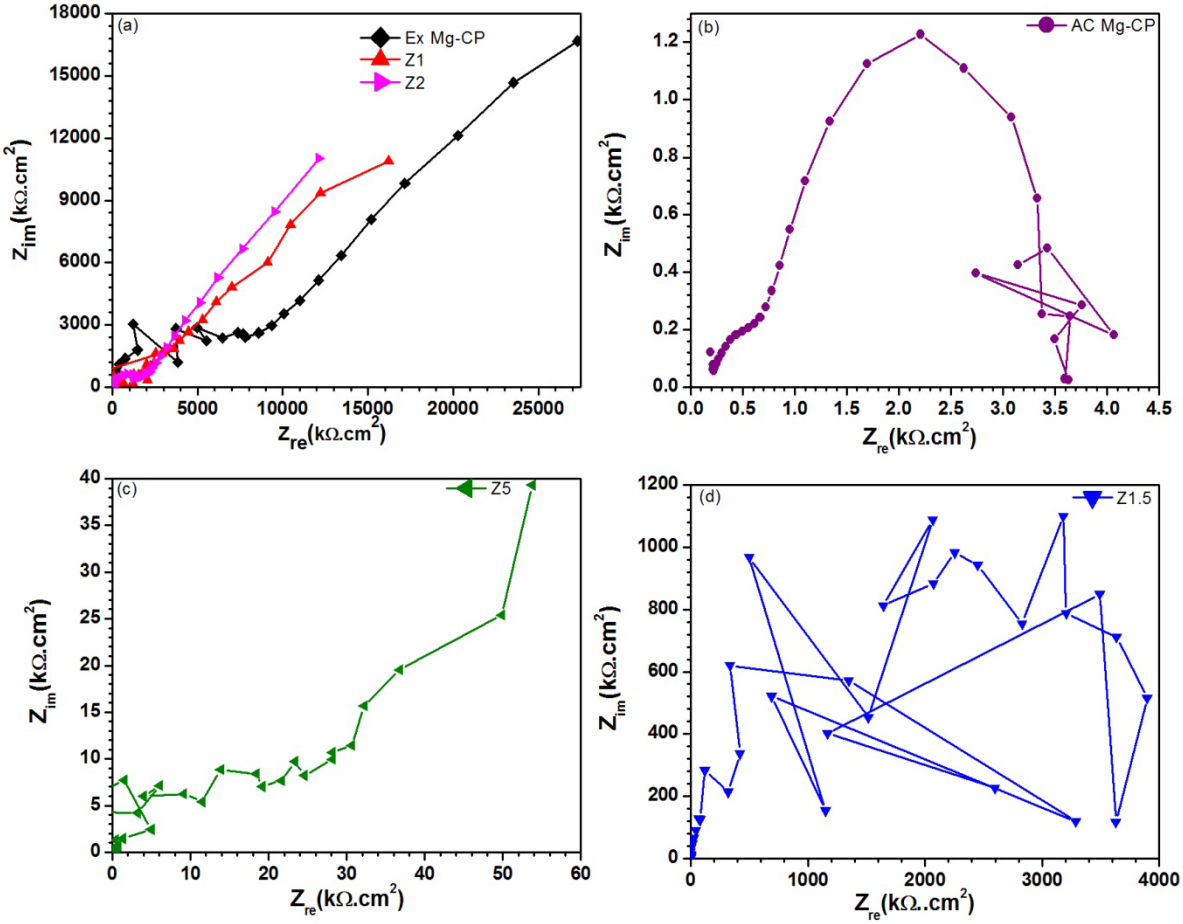

Figure A1.3 Nyquist plots for (a) Z1, Z2 and Ex Mg-CP; (b) AC Mg-CP; (c) Z5 and; (d) Z1.5 samples (Repeat 2)

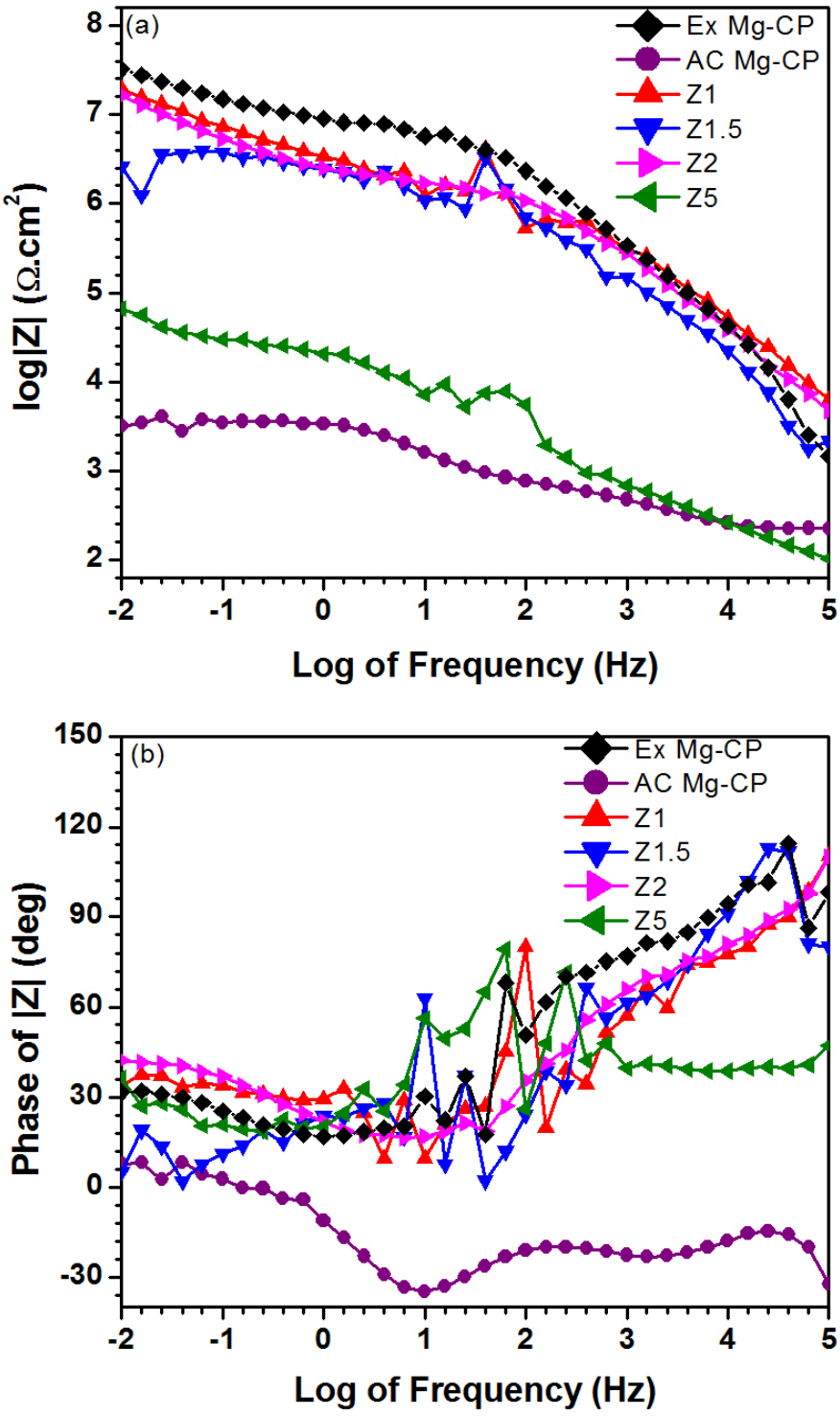

Figure A1.4 Bode (a) magnitude and; (b) phase plots for all samples (Repeat 2)

Table A1.1 Values of the electrical parameters of the curve-fitted EIS data (Repeat 2)

Material (Run2)	R_s (10^6 Ω.cm^2)	C_{dl} (10^{-10} µF)	R_{ct} (10^4 Ω.cm^2)	W (10^{-7})	Chi-squared
Ex Mg-CP	90.1 (62.15)	4.543 (5.99)	580 (10.94)	0.9171 (22.68)	5.899 x 10^{-2}
AC Mg-CP	2.086 x 10^{-4} (8.57)	1.329x10^{24} (5.013x10^{17})	0.3836 (6.872)	485.2 (9.12)	3.916 x 10^{-2}
Z1	*435.6* *(1140)*	*2.905* *(13.68)*	*229.7* *(17.61)*	*2.223* *(36.48)*	*2.542 x 10^{-1}*
Z1.5	*4.072* *(42)*	*8.065* *(14.28)*	*591.1* *(75.76)*	*0.9295* *(254.5)*	*3.231 x 10^{-1}*
Z2	1028 (1138)	4.243 (5.46)	120.3 (7.408)	2.639 (11.03)	3.876 x 10^{-2}
Z5	*-4.433 x 10^8* *(5.562 x 10^{10})*	*13.09* *(2.895 x 10^5)*	*-1595* *(1.732 x 10^7)*	*117* *(13.32)*	*4.182 x 10^{-1}*

A2: 3rd Repeat of the Electrochemical Test

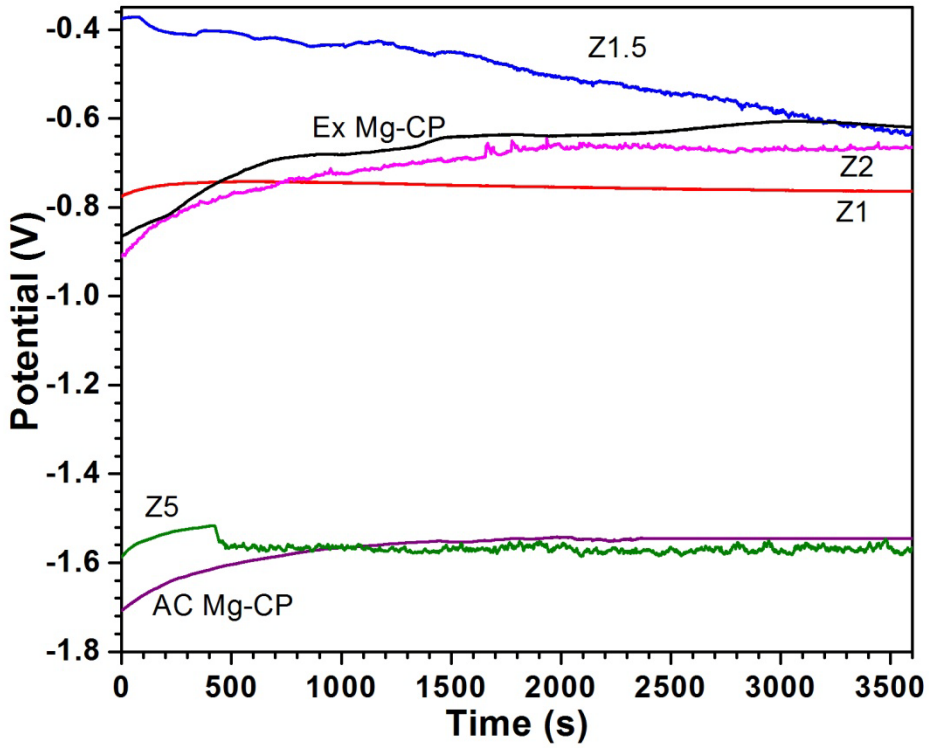

Figure A2.1 OCP vs. time plots for all samples (Repeat 3)

The Tafel plot for Z5 (Figure A2.2 (b)) is erroneous and was not used in the E_{corr}, i_{corr} and corrosion rate calculations.

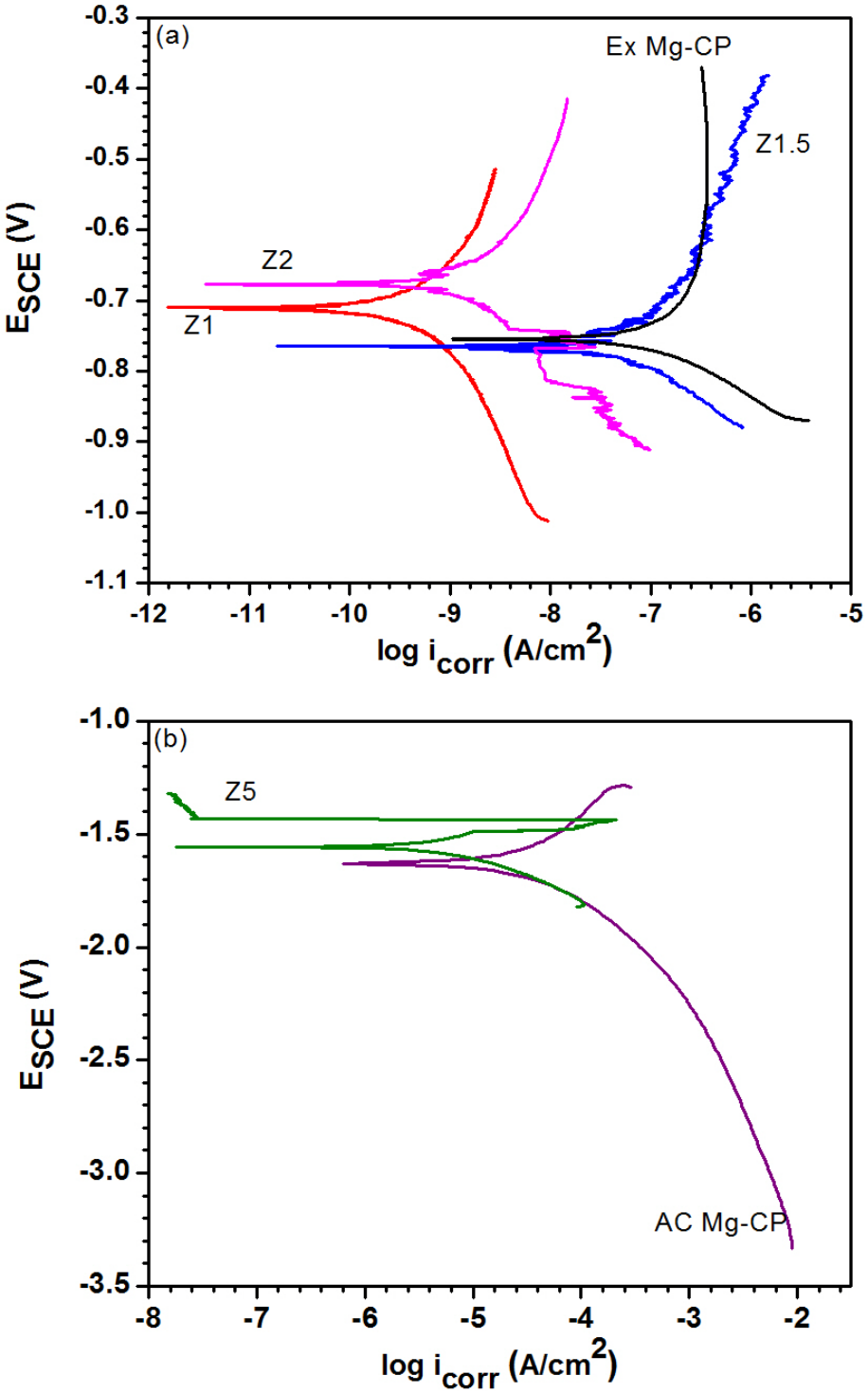

Figure A2.2 Tafel plots for (a) Ex Mg-CP, Z1, Z1.5 and Z2; (b) Z5 and AC Mg-CP (Repeat 3)

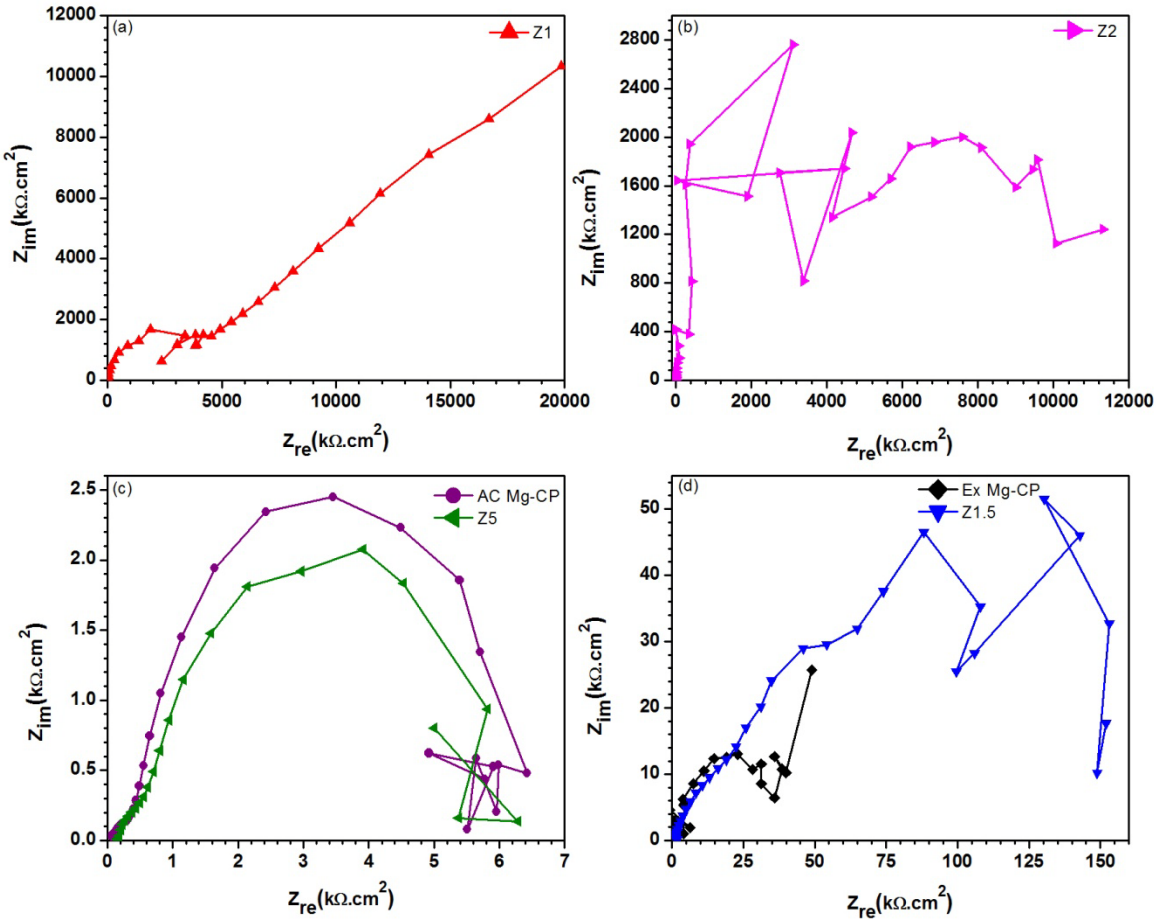

Figure A2.3 Nyquist plots for (a) Z1; (b) Z2; (c) AC Mg-CP and Z5; (d) Ex Mg-CP and Z1.5 samples (Repeat 3)

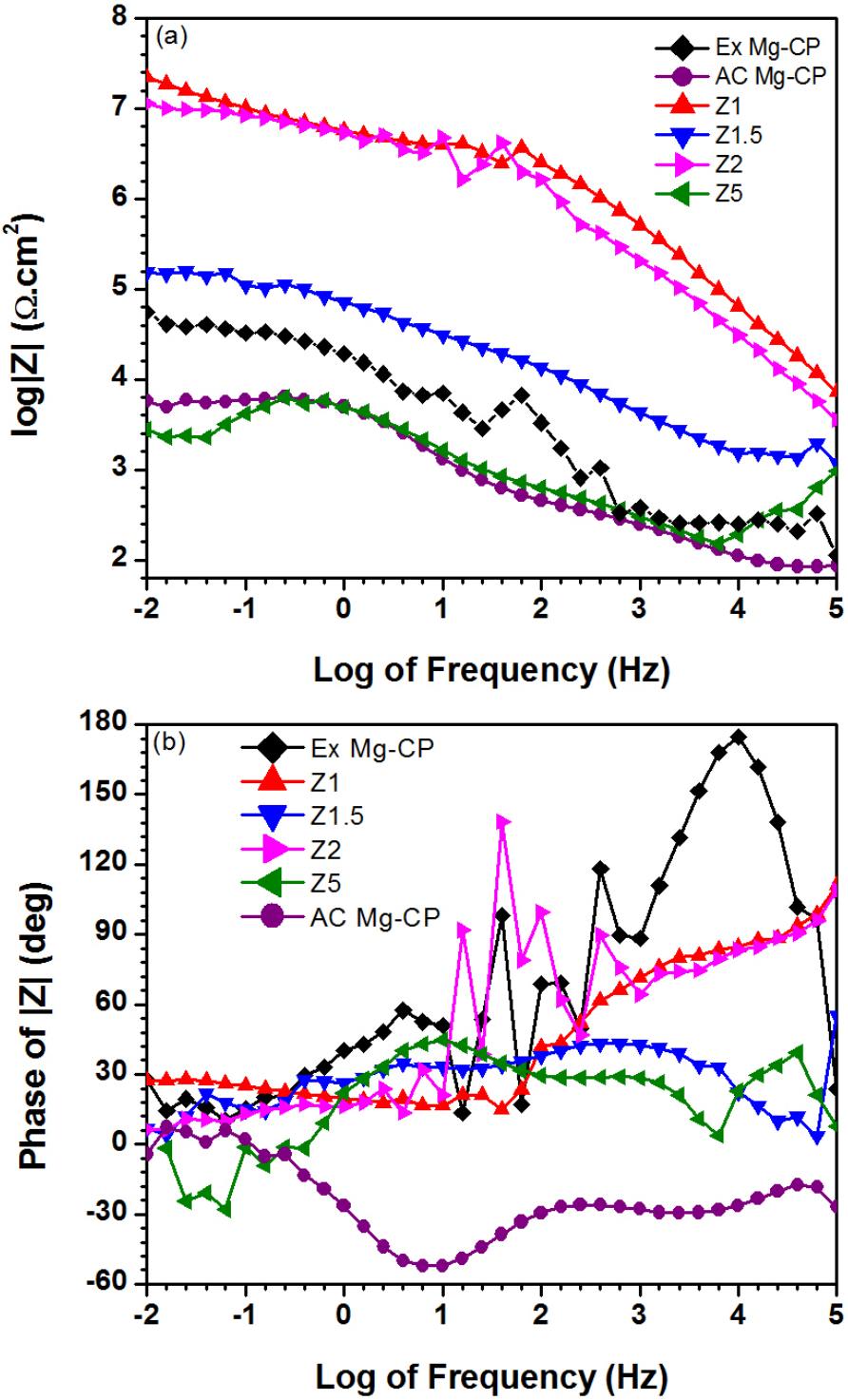

Figure A2.4 Bode (a) magnitude and; (b) phase plots for all samples (Repeat 3)

Table A2.1 Values of the electrical parameters of the curve-fitted EIS data (Repeat 3)

Material (Run3)	**R_s (10^6 Ω.cm^2)**	**C_{dl} (10^{-10} µF)**	**R_{ct} (10^4 Ω.cm^2)**	**W (10^{-7})**	**Chi-squared**
Ex Mg-CP	*-1.068 x 10^{14}* *(8.452 x10^{-13})*	*3.313 x 10^{-9}* *(30.24)*	*-1.32 x 10^{11}* *(1.045 x10^9)*	*2.084 x 10^{13}* *(5.002 x 10^{22})*	*1.161*
AC Mg-CP	63.37 x 10^{-6} (15.18)	2.587x10^{22} (2.635e16)	0.8362 (11.73)	656.7 (8.235)	7.379 x 10^{-2}
Z1	42.98 (27.11)	2.524 (4.537)	328.1 (7.163)	1.124 (13.7)	2.857 x 10^{-2}
Z1.5	0.1736 (9.094)	2.504 (83.26)	0.1132 (14.22)	33.67 (6.402)	4.516 x 10^{-2}
Z2	*-9.132 x 10^{13}* *(1.935 x 10^{13})*	*4.167* *(27.68)*	*-10.55* *(296.9)*	*0.1539* *(21.42)*	*6.175 x 10^{-1}*
Z5	*0.007956* *(25.71)*	*1 x 10^{-14}* *(1.484x10^{17})*	*0.0509.6* *(20.24)*	*609* *(29.11)*	*3.516 x 10^{-1}*